

https://dspace.org/

Low-loaded Platinum electrocatalysts on non-carbon supports for the development of direct ethanol fuel cells

Modise, Refiloe Petronella

2020

https://hdl.handle.net/10539/30177

Downloaded from a DSpace repository. https://dspace.org/

Low-loaded Platinum Electrocatalysts on Non-carbon Supports for the Development of Direct Ethanol Fuel Cells



By

Refiloe Petronella Modise

A dissertation submitted to the Faculty of Science, University of the Witwatersrand, Johannesburg, in fulfilment of the requirements for the degree of Master of Science.

March 2020

Declaration

I declare that this dissertation is my own, unaided work. It is being submitted for the Degree of Master of Science at the University of the Witwatersrand, Johannesburg. It has not been submitted before for any degree or examination at any other University.



(Signature of candidate)

Signed on the 27th day of March 2020 at Johannesburg.

Abstract

Platinum-based electrocatalysts (Pt/TiO_2, Pt/TiO_2Mn, Pt/TiO_2Ce, $Pt/TiO_2Mn_{0.5}Ce_{0.5}$ and $Pt/TiO_2Ce/C$) were prepared using the alcohol reduction method. The electrocatalysts were characterized using X-ray diffraction (XRD), Raman spectroscopy, ultraviolet-visible spectroscopy (UV-vis.), Scanning electron microscopy (SEM), transmission electron microscopy (TEM) and X-ray photoelectron spectroscopy (XPS) to investigate their physical properties. This was followed by the electrochemical behaviour evaluation in ferri-ferrocyanide ($Fe(CN)_6^{3-}/Fe(CN)_6^{4-}$) using cyclic and linear sweep voltammetry, chronoamperometry (CA) electrochemical impedance spectroscopy (EIS) and Bode impedance. A fast electron (e^-) transfer and enhanced Faradaic current was exhibited by $Pt/TiO_2Ce/C$ relative to the other electrocatalysts, aided by the electronic conductivity of carbon. This was illustrated by the smaller peak potential separation, large active area and high electrode surface coverage compared to the other electrocatalysts. The electrocatalysts illustrated a mixed adsorption-diffusion controlled (more of diffusion) mass transport mechanism as demonstrated by the effect of scan rate on the peak current. Thereafter, the electrochemical behaviour of the electrocatalysts towards ethanol oxidation reaction (EOR) was evaluated in acidic and alkaline electrolyte separately using cyclic voltammetry (CV), linear sweep voltammetry (LSV), CA and EIS techniques. The results illustrated the dependence of EOR on the co-catalysts manganese (Mn) and/or manganese oxide (MnO_X) as well as cerium (Ce) and/or ceria (CeO_x) in titanium dioxide (TiO_2). Especially, the catalysts supported on TiO_2/Ce and/or CeO_x which exhibited lower onset potential (E_{onset}), fast electron transport (smaller ΔE_p), enhanced Faradaic current response, high exchange current densities and lower charge transfer resistance (R_{ct}). The activity towards the EOR was observed to

increase in the following order: Pt/TiO_2 < Pt/TiO_2Mn < $Pt/TiO_2Mn_{0.5}Ce$ ≤ Pt/TiO_2Ce < $Pt/TiO_2Ce/C$.

Moreover, the electrocatalysts, Pt/TiO_2, Pt/TiO_2Mn, Pt/TiO_2Ce, $Pt/TiO_2Mn_{0.5}Ce_{0.5}$ and $Pt/TiO_2Ce/C$ were investigated for their electrochemical behaviour towards oxygen reduction reaction (ORR). Again, Pt/TiO_2Ce exhibited enhanced activities showing more positive E_{onset} and half-wave potential ($E_{1/2}$) accompanied by high diffusion-limited current density (j_d). However, it was interesting to note that the Pt/TiO_2Mn was more efficient towards ORR, indicated by the number of electrons (n) determined from the Koutecky-Levich (K-L) plots and equation. According to the K-L plots, the ORR for the Pt/TiO_2, Pt/TiO_2Mn, $Pt/TiO_2Mn_{0.5}Ce_{0.5}$, $Pt/TiO_2Ce/C$ proceed via the 4 e^- and Pt/TiO_2Ce demonstrated a 2 e^- processes. The catalytic activity towards ORR increased in the following order: Pt/TiO_2Mn < Pt/TiO_2 < $Pt/TiO_2Mn_{0.5}Ce_{0.5}$ < Pt/TiO_2Ce < $Pt/TiO_2Ce/C$.

Acknowledgements

My heartfelt gratitude to my supervisors, Prof. Kenneth I. Ozoemena and Dr. Jessie I. Pillay, for their guidance throughout the past two years. I appreciate the comments, advice and lessons learnt throughout the duration of the course.

I am also thankful to Prof. Neil Coville for granting access to the laboratory C117 during my studies, Dr. Caren Billing who granted access to use the VMP-300 Potentiostat for some of my experimental work. I appreciate the assistance and guidance from the Materials Electrochemistry and Energy Technologies (MEET) team, especially, Mr. Adewale Ipadeola for his comments and advices throughout. It has been both a pleasant and productive experience to work with all the MEET members. I acknowledge Dr. Rudolf Erasmus for his assistance with Raman Analysis as well as the Microscopy and Microanalysis Unit (MMU) staff at Wits for XRD, SEM and TEM training and granting me access to use the microscopes for the full length of my MSc research.

I extend my gratitude to the Materials and Characterization Laboratory team at National Metrology Institute of South Africa (NMISA); Dr. Clive Oliphant, Mrs. Loukie Adlem and Ms. Fortunate Modiba for their assistance with SEM as well as Mr. Werner Jordan who assisted with the XPS analysis. In addition, would like to thank both NMISA and PFK electronics for funding this project and my academic fees.

Finally, I would like to acknowledge my parents and siblings. Especially, mom and dad who sacrificed a lot in their lives, to help me reach this far. I wish you both, good health, love, peace and wisdom, for as long as you live. To my friends who constantly motivated me throughout the past two years, your support has been truly helpful. Then last but the most important, God who has carried me by His grace.

Table of Contents

Abstract ii

Acknowledgements iv

Table of Contents v

List of Figures ix

List of Tables xii

List of Abbreviations and Symbols xiv

RESEARCH OUTPUTS xx

Chapter 1 1

Introduction 1

1.1 Introduction 1

1.2 Motivation of the Study 2

1.3 Aim and Objectives 5

1.3.1 Aim 5

1.3.2 Objectives 5

1.4 Scope of Research Project 6

Chapter 2 8

Literature Review 8

2.1 Fuel Cells 8

2.1.1 Proton Exchange Membrane Fuel Cell (PEMFC) 9

2.1.2 Direct Alcohol Fuel Cells (DAFCs) 11

2.2 Electrocatalyst for DAFCs 14

2.2.1. Platinum (Pt) and Pt-based catalysts 15

(i) Pt alloy and core-shells 15

(ii) Effect of Particle Size.....16

2.2.2. Catalyst Supports for DEFCs 16

(i) Alternative Carbon Supports 17

(ii) Non-carbon Supports.....18

Titanium dioxide (TiO_2).....19

Ceria oxide (CeO_X) and Manganese oxides (MnO_X).....21

2.3 Material Characterization.....22

2.3.1 Powder X-Ray Diffraction (PXRD) 22

2.3.2 Raman Spectroscopy 24

2.3.3 Ultra-violet Visible Spectroscopy (UV-vis.) 24

2.3.4 Scanning Electron Microscopy (SEM).....25

2.3.5 Energy Dispersive Spectroscopy (EDS).....25

2.3.6 Transmission Electron Microscopy (TEM).....26

2.3.7 X-Ray Photoelectron Spectroscopy (XPS).....26

2.4 Electrochemical Characterization Techniques 27

2.4.1 Cyclic Voltammetry (CV) 27

2.4.2 Cyclic Voltammetry (CV) and Ethanol Oxidation Reaction.....29

2.4.3 Linear Sweep Voltammetry (LSV).....30

2.4.4 Chronoamperometry (CA).....31

2.4.5 Electrochemical Impedance Spectroscopy 32

2.4.6 Rotating Disc Electrode (RDE) and Oxygen Reduction Reaction 33

Chapter 3 36

Materials and Methods 36

3.1 Chemicals 36

3.2. Synthetic Methods 36

3.2.1 Synthesis of Support Material 36

3.2.2 Synthesis of Electrocatalyst Materials 37

3.3 Physical Characterization 38

3.3.1 Powder X-Ray Diffraction (PXRD) 38

3.3.2 Raman Spectroscopy 38

3.3.3 Ultra-violet Visible Spectroscopy (UV-vis.) 39

3.3.4 Scanning Electron Microscopy (SEM) 39

3.3.5 Energy Dispersive Spectroscopy (EDS) 39

3.3.6 Transmission Electron Microscopy (TEM) 39

3.3.7 X-Ray Photoelectron Spectroscopy (XPS) 40

3.4 Electrochemical Characterization 40

3.4.1 Cells, Electrodes and Sample Preparations 40

3.4.2 Cyclic Voltammetry (CV) 42

3.4.3 Cyclic Voltammetry (CV) and Ethanol Oxidation Reaction 42

3.4.4 Linear Sweep Voltammetry (LSV) 42

3.4.5 Chronoamperometry (CA) 42
3.4.6 Electrochemical Impedance Spectroscopy 43
3.4.7 Rotating Disc Electrode (RDE) and Oxygen Reduction Reaction 43
3.4.8 EtOH Gas Sensing 43
Chapter 4 45
Physical and Electrochemical Characterization of the Supports and Electrocatalysts 45
4.1. Results and Discussion 45
4.1.1. Physical Characterization 45
4.1.2 Electrochemical characterization 58
4.2. Conclusion 64
Chapter 5 66
Electrochemical Behaviour of the Electrocatalysts towards EOR 66
5.1. Results and Discussion 66
5.1.1. Electro-oxidation of ethanol in acidic and alkaline electrolyte 66
5.2. Conclusion 80
Chapter 6 81
Electrochemical Behaviour of the Electrocatalysts towards ORR 81
6.1. Results and Discussion 81
6.1.1. Oxygen reduction reaction in acidic and alkaline electrolyte 81
6.2 Conclusion 90
Chapter 7 91

Sensing Performance of Pt/TiO_2Ce/C.....91

7.1 Introduction.....91

7.2. Results and Discussion.....93

7.3. Conclusion.....94

Chapter 8.....95

Summary and Recommendations.....95

References.....99

List of Figures

Figure 1.1: Schematic representation of carbon corrosion under fuel cell operating conditions. 3

Figure 2.1: Schematic diagram of a Proton Exchange Membrane Fuel Cell [44]. 11

Figure 2.2: Schematic diagram of DAFC [46].....12

Figure 2.3: Carbon support materials [76]. 17

Figure 2.4: Cyclic voltammogram of carbon supported Pt catalyst in 0.5 M H_2SO_4. 28

Figure 2.5: Cyclic voltammogram of Pt/C catalyst in 0.5 M H_2SO_4 + 0.5 M EtOH. 30

Figure 2.6: Linear sweep voltammogram of Pt/C in 0.5 M H_2SO_4 + 0.5 M EtOH. 31

Figure 2.7: Current time curve for carbon supported Pt catalyst in 0.5 M H_2SO_4 + 0.5 M EtOH, polarized at an oxidation potential of 0.75 V for 900 s. 32

Figure 2.8: The EIS Nyquist plot for GCE in 0.1 M KCl containing 3.0 mM $[Fe(CN)_6]^{3-/4-}$ polarized at open circuit potential (OCV) 0.30 V vs. Ag|AgCl, 3.0 M KCl, from 0.1 Hz to 100 kHz. 33

Figure 2.9: The corresponding equivalent electrochemical circuit of a GCE.....33

Figure 2.10: Linear Sweep Voltammograms of Pt/C in O_2 saturated 0.50 M H_2SO_4. 34

Figure 3.1: A three-electrode cell used for $K_3[Fe(CN)_6]$/ $K_4[Fe(CN)_6]$ and EOR experiments. 40

Figure 3.2: A three-electrode cell used for ORR rotating disc electrode experiment.....41

Figure 3.3: A picture of the experimental gas sensing set up. 44

Figure 4.1: (A) PXRD patterns of the supports (a) TiO_2 anatase, (b) TiO_2, (c) TiO_2Mn, (d) TiO_2Ce, (e) $TiO_2Mn_{0.5}Ce_{0.5}$ and (f) TiO_2Ce/C and (B) the enlarged view of the (1 0 1) peak. 45

Figure 4.2: PXRD patterns of the electrocatalysts. 47

Figure 4.3: The Raman spectra of (a) the prepared supports and (b) an enlarged view of the Eg peak of the supports. 48

Figure 4.4: (a) UV-visible spectra and (b) Tauc plot for TiO_2 anatase, TiO_2, TiO_2Mn, TiO_2Ce and TiO_2 $Mn_{0.5}Ce_{0.5}$.....49

Figure 4.5: XPS spectra of (a) Ti2p and (b) O1s for TiO_2 anatase and the electrocatalysts....51

Figure 4.6: XPS spectra of (a) Mn2p and (b) Ce3d of the electrocatalysts. 54

Figure 4.7: XPS spectra of Pt4f for the electrocatalysts. 55

Figure 4.8: (a–d) SEM images Pt/TiO_2, Pt/TiO_2Mn, Pt/TiO_2Ce and Pt/TiO_2 $Mn_{0.5}Ce_{0.5}$, respectively. 56

Figure 4.9: EDX spectra (a-d) of Pt/TiO_2, Pt/TiO_2Mn, Pt/TiO_2Ce and Pt/TiO_2 $Mn_{0.5}Ce_{0.5}$, respectively. 57

Figure 4.10: The TEM images of the electrocatalysts (a) Pt/TiO_2, (b) Pt/TiO_2Mn, (c) Pt/TiO_2Ce and (d) $Pt/TiO_2Mn_{0.5}Ce_{0.5}$, (e) $Pt/TiO_2Ce/C$. 57

Figure 4.11: Cyclic Voltammograms of the bare GCE and modified GCE in 0.1 M KCl containing 3.0 mM $K_3[Fe(CN)_6]/K_4[Fe(CN)_6]$ at 10 mVs^{-1}. 58

Figure 4.12: The (a) log i_p vs. log ν and (b) i_p vs. $\sqrt{\nu}$ plots for bare GCE and Pt/TiO_2, Pt/TiO_2Mn, Pt/TiO_2Ce, $Pt/TiO_2Mn_{0.5}Ce_{0.5}$ and $Pt/TiO_2Ce/C$.....60

Figure 4.13: The (a) Nyquist plots, (b,c) EEC and Bode plots, (d) log Z vs. log frequency and (e) phase Z vs. log frequency for the GCE and modified GCE in 0.10 M KCl containing 3.0 mM $K_3[Fe(CN)_6]/K_4[Fe(CN)_6]$.....63

Figure 5.1: Cyclic voltammograms of the electrocatalysts in N_2 purged (a) 0.5 M H_2SO_4 and (b) 0.5 M KOH collected at a scan rate of 25 mVs^{-1}.....67

Figure 5.2: Cyclic voltammograms of the electrocatalysts in N_2 purged (a) 0.5 M H_2SO_4 + 0.5 M EtOH and (b) 0.5 M KOH + 0.5 M EtOH collected at a scan rate of 50 mVs^{-1}.....68

Figure 5.3: Current-time curves recorded at 0.70 and – 0.30 V in (a) 0.5 M H_2SO_4 and (b) 0.5 M KOH. 71

Figure 5.4: The i_p vs. $\sqrt{v}$ plots for the electrocatalysts in (a) 0.5 M H_2SO_4 and (b) 0.5 M KOH. 72

Figure 5.5: The (a,b) linear sweep voltammograms and (c,d) Tafel plots of the electrocatalysts in 0.5 M H_2SO_4 and 0.5 M KOH. 73

Figure 5.6: (a,b) The fitted Nyquist plots of the electrocatalysts in both electrolytes, Equivalent electrochemical circuits of (c) Pt/TiO_2, Pt/TiO_2Mn and $Pt/TiO_2Mn_{0.5}Ce_{0.5,}$ (d) Pt/TiO_2Ce and (e) $Pt/TiO_2Ce/C$ in acidic and alkaline electrolyte.....75

Figure 5.7: The Bode impedance plots (a, b) phase angle vs. log frequency and (c, d) log Z vs. log frequency. 77

Figure 5.8: Variations of the ECSA of the electrocatalysts with the cycle number during the ADT. 79

Figure 6.1: CVs of the electrocatalysts in (a) 0.5 M H_2SO_4 and (b) 0.1 M KOH collected at 25 mVs^{-1}.....81

Figure 6.2: LSVs of the electrocatalysts in O_2 saturated (a) 0.5 M H_2SO_4 and (b) 0.1 M KOH collected at 1600 rpm, 10 mVs^{-1}.....82

Figure 6.3: K-L plots of the electrocatalysts in 0.5 M H_2SO_4 for (a) Pt/TiO_2, (b) Pt/TiO_2Mn, (c) Pt/TiO_2Ce, (d) $Pt/TiO_2Mn_{0.5}Ce_{0.5}$ and $Pt/TiO_2Ce/C$. 87

Figure 6.4: K-L plots of the electrocatalysts in 0.1 M KOH for (a) Pt/TiO_2, (b) Pt/TiO_2Mn, (c) Pt/TiO_2Ce, (d) $Pt/TiO_2Mn_{0.5}Ce_{0.5}$ and $Pt/TiO_2Ce/C$. 88

Figure 6.5: Tafel slopes of the electrocatalysts in (a) 0.5 M H_2SO_4 and (b) 0.1 M KOH.....89

Figure 7.1: The current-time curve polarized at -0.40 V for 15 seconds and (insert) concentration against current plots. 93

List of Schemes

Scheme 3.1: Synthesis of the support materials.....37

.....38

Scheme 3.2: Synthesis of the electrocatalysts.....38

List of Tables

Table 2.1: The types of fuel cells.....9

Table 4.1: Average crystallite size and lattice parameter by XRD for the electrocatalysts….47

Table 4.2: Band gap and shifts.....50

Table 4.3: The binding energies and elemental at. % of the TiO_2 anatase and electrocatalysts from XPS analysis.....53

Table 4.4: Summary of data obtained from CV of the bare GCE and electrocatalysts in 0.1 M KCl containing 3.0 mM $K_3[Fe(CN)_6]$/ $K_4[Fe(CN)_6]$. 62

Table 4.5: EIS data and Bode impedance data for the bare GCE and modified GCE. The values in the parenthesis are the deviations from the real fit. 64

Table 5.1: Electrochemical properties of the catalysts studied in both acidic and alkaline media. 70

Table 5.2: Exchange current densities of the electrocatalysts in both acidic and alkaline media. 74

Table 5.3: Resistance parameters of the electrocatalysts for EOR studied in both acidic and alkaline media. 76

Table 5.4: Pseudocapacitance parameters of the electrocatalysts for EOR studied in both acidic and alkaline media. 78

Table 6.1: Electrocatalytic activitiesof the electrocatalysts for the ORR studied using RDE and collected at 1600 rpm, 10mVs^{-1} in O_2 saturated 0.5 M H_2SO_4 and 0.1 M KOH electrolyte. ..84

Table 6.2: The estimated number of electrons transferred (*n*) for the electrocatalysts.....85

Table 6.3: The kinetic rate constants (*k*) estimated for the electrocatalysts. 86

List of Abbreviations and Symbols

ΔEp: Peak potential seperation

AC: Alternating current

ADAFC: Alkaline Direct Alcohol Fuel Cell

Ag: Silver

AgCl: Silver chloride

b: Tafel slope

BAC: Blood alcohol content

BrAC: Breath alcohol content

C: Carbon

C_2H_5OH: Ethanol

CA: Chronoamperometry

C–C: Carbon bonded to carbon

CCD: Charged coupled device

C_{dl}: Double layer capacitance

$Ce(NO_3)_3 \cdot 6H_2O$: cerium nitrate hexahydrate

Ce: Cerium

$Ce_2Ti_2O_7$: Cerium titanate

CeO_2: Ceria

CH_3COH: Acetaldehyde

CH_3COOH: Acetic acid

CN: Coordination number

CNFs: Carbon nanofibres

CNTs: Carbon nanotubes

CO: Carbon monoxide

$E°$: Standard electrode potential

Fe: Iron

g: gram

GC: Gas Chromatography

GCE: Glassy Carbon Electrode

GDL: Gas Diffusion Layer

Gly: Glycerol

GO: Graphene Oxide

h: hour

H^+: Proton

H_2: Hydrogen

H_2O: Water

H_2O_2: Hydrogen peroxide

H_2SO_4: sulfuric acid

Hz: Hertz

i: Current

i_p: peak current

i_{fp}: Forward peak current

i_{rp}: Reverse peak current

ICDD: Inorganic crystal structure database

IPA: Isopropanol

IR: Infrared

j: Current density

j_d: Diffusion-limited current density

j_o: Exchange current density

k: Rate constant

K_2PtCl_4: Tetrachloroplatinate

$K_3Fe(CN)_6$): Potassium hexacyanoferrate

KCl: Potassium chloride

kHz: kiloHertz

K-L: Koutecky Levich

KOH: Potassium hydroxide

kV: kiloVolt

LiF: Lithium flouride

LoD: Limit of detection

LSV: Linear sweep voltammetry

M: Transition metal

mA: milliampere

MC: Metal carbides

MCFCs: Molten carbonate fuel cells

MCN: Metal carbonitride

MEA: Membrane Electrode Assembly

MeOH: Methanol

mg: milligram

min: minute

MITNAD: Microwave induced top down nanostructuring and decoration

mL: millilitre

mmol: millimole

$Mn(NO_3)_2 \cdot 4H_2O$: Manganese nitrate tetrahydrate

Mn: Manganese

MN: Metal nitride

MnO_X: Manganese oxide

Mo: Molybdenum

MoO_X: Molybdenum oxide

MOR: Methanol oxidation reaction

MO_X: Metal Oxides

mV dec^{-1}: millvolt per decade

η: Overpotential

NHE*:* Normal hydrogen electrode

N_2: Nitrogen

Ni: Nickel

NMISA: National Metrology Institute of South Africa

O: Oxygen

O_2: Oxygen

OCV: Open circuit voltage

OH: Hydroxyl

OH_{ads}: Adsorbed hydroxyls

OLC: Onion like carbon

ORR: Oxygen reduction reaction

PAFCs: Phosphoric Acid Fuel Cells

Pd: Palladium

PEM: Proton Exchange Membrane

PEMFC: Proton Exchange Membrane Fuel Cell

Pt: Platinum

PVP: Polyvinylpyrolidone

PXRD: Powder X-ray diffraction

R^2: Linear regression

R_{ct}: Charge transfer resistance

RDE: Ring disk electrode

RHE: Reversible hydrogen electrode

rpm: rotation per minute

R_s: Solution resistance

Ru: Ruthenium

s: Second

SA: South Africa

SEM: Scanning electron microscopy

Si: Silicon

SMSI: Strong metal-support interaction

Sn: Tin

SnO_2: Tin oxide

SO_4^{2-}: sulfate

SRGO: Sulfonated reduced graphene oxide

TCN: Titanium carbonitride

TEM: Transmission electron microscopy

Ti: Titanium

TiC: Titanium carbide

TiN: Titanium nitride

TiO_2: Titanium dioxide

TNTs: Titania nanotubes

UV – vis: Ultra-violet visible

V/s: Volts per second

VOCs: Volatile organic compounds

vol.%: Volume percent

W: Tungsten

W: Watts

WC: Tungsten carbide

WO_X: Tungsten oxide

wt.%: weight percentage

XPS: X-ray photoelectron spectroscopy

W: Warburg impedance

v: Scan rate

Ω: Ohm

RESEARCH OUTPUTS

MANUSCRIPTS BEING PREPARED FOR PUBLICATIONS

1) **Refiloe P. Modise**, Jessie I. Pillay and Kenneth I. Ozoemena, "*Low-loaded Pt nanocatalysts on CeO_X doped TiO_2 Support for Enhanced Ethanol Oxidation Reaction: Synergistic Effects of Ceria-doping and H_2-treatment of TiO_2"* (in preparation)

2) **Refiloe P. Modise**, Jessie I. Pillay and Kenneth I. Ozoemena, "*The Design and Synthesis of Pt nanostructured Catalysts Supported on CeO_X doped TiO_2 Composite for Oxygen Reduction Reaction in Acid and Alkaline Media"* (in preparation)

Conference Presentation

A part of the work reported in this dissertation has been reported at:

1) **Refiloe P. Modise**, Jessie I. Pillay and Kenneth I. Ozoemena "*Platinum nanoparticles supported on titanium dioxide nanoparticles for electro-oxidation reaction in acidic electrolyte"*,70th International Society of Electrochemistry (ISE), 4-9th August 2019, Durban, South Africa **(POSTER Presentation)**
2) **Refiloe P. Modise**, Jessie I. Pillay and Kenneth I. Ozoemena "*Platinum nanoparticles supported on titanium dioxide nanoparticles for electro-oxidation reaction in acidic electrolyte"*, 9th South African Nanotechnology Initiative – Nanoscience Young Researchers'Symposium, 12th November 2019, University of Pretoria, Pretoria, South Africa **(POSTER Presentation, which received the Prize as 3rd best Masters poster presentation).**

Chapter 1
Introduction

1.1 Introduction

The increasing global population gradually leads to an escalation in energy demand. Fossil fuels are the primary sources of energy. However, dependence on fossil fuels as energy source is non-desirable since they are non-renewable and unsustainable. In addition, the excessive usage of fossil fuels will gradually deplete the reserves. Another disadvantage with the utilization of fossil fuels is environmental pollution during the combustion process. The burning of fossil fuels is a threat to humans, animals and the environment. This is attributed to the emission of greenhouse gases that result in climate changes on planet Earth and respiratory related illnesses with human beings [1–2]. Consequently, there is an increasing interest in other energy sources that are renewable, sustainable and clean. For instance, energy can be generated from the sun, wind etc., however these are seasonal. Other sustainable and clean energy production methods are via the use of energy storage and/or conversion devices. Energy storage devices such as, supercapacitors and batteries, stores chemical energy and delivers electrical energy when required, whereas energy conversion devices, like fuel cells convert chemical energy from fuels into electrical energy [3–6]. Fuel cells, unlike fossil fuels are energy conversion devices that generate low pollutant emissions and have high efficiency. In a fuel cell, a fuel such as hydrogen (H_2) is oxidized and oxygen (O_2) is reduced. As a result, electricity is produced via the flow of electrons (e^-) in the cell, as well as, water (H_2O) which is the by-product, unlike the greenhouse gases produced in the combustion of fossil fuels [7]. Also, when compared to batteries and supercapacitors, fuel cells exhibit longer operating time, high energy density output and a continuous supply in energy, so long as fuel and oxygen is fed into

the device [6,8]. Thus, fuel cells are efficient and environmentally benign. Today, several types of fuel cells exist due to their efficiency and sustainability.

The commercialization of proton exchange membrane fuel cells (PEMFCs) are limited by the high cost of production, storage and transportation of H_2. Therefore, researchers have directed their interest to the use of alcohols such as, methanol (MeOH) and ethanol (EtOH) that have low-molecular weight as fuel. The liquid fuels are cheaper to produce, easy to store and transport using the current existing petroleum infrastructures [9]. The devices are commonly known as, direct alcohol fuel cells (DAFCs), where direct methanol fuel cell (DMFC) and direct ethanol fuel cell (DEFC) make use of MeOH and EtOH, respectively.

1.2 Motivation of the Study

The low temperature DEFCs are widely investigated due to their attractive properties such as their use of a renewable and sustainable fuel such as EtOH which can be produced from abundant natural resources like sugar cane, woodchips, corn etc., in large quantities [10]. Also, EtOH unlike MeOH is non-toxic and possesses high energy density (8.01 vs. 6.09 kWh/kg for MeOH) [9,11,12]. However, the full commercialization of DEFCs is limited by: (i) high Pt content (20 – 60 wt. %) in the electrocatalyst, as the cost of Pt and its scarcity resulted in a high cost of the device [13,14] , (ii) the poor stability of carbon black in the operating conditions (oxidant rich, high pH and humidity) with a high tendency to corrode, since carbon undergoes oxidation under these conditions and loses interaction with Pt catalyst, thereby leading to its dissolution and agglomeration as depicted in Figure 1.1. This decreases the electrochemical surface area (ECSA) and subsequently reduces the efficiency of the electrocatalyst [9,13,15]. Lastly, (iii) the slow ethanol oxidation reaction (EOR) and oxygen reduction reaction (ORR) kinetics due to poisoning of Pt by reaction intermediates (acetaldehyde, carbonyls or hydroxyls), blocking the active sites that hinder the oxidation of fresh alcohol or oxygen molecules [13,16,17].

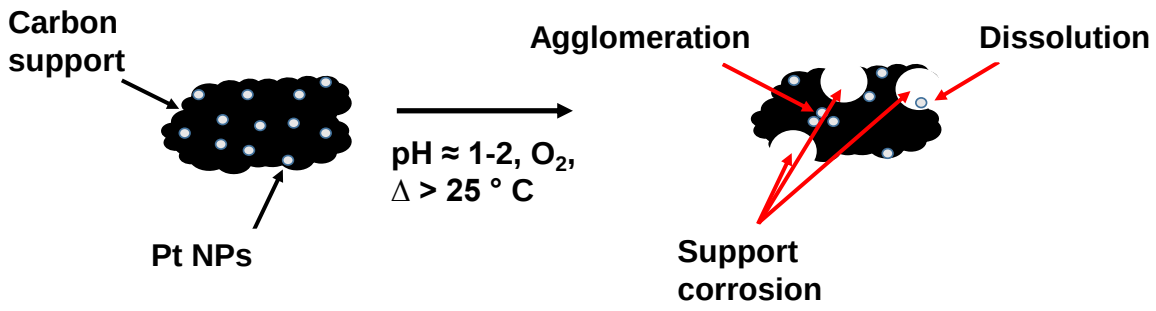


Figure 1.1: Schematic representation of carbon corrosion under fuel cell operating conditions.

Recent studies on power generating fuel cells that are applicable in stationary (generators) [18,19,20,21], mobile (transportation vehicles) [19,20,21,22,23] and portable devices (battery chargers) [4,10,18,19,24] have demonstrated strategies to improve the electrocatalytic activity and stability of the electrocatalysts. For instance, the use of durable support materials (carbon and non-carbon), reduced or non-Pt based catalysts to lower the cost and enhance the performance of the fuel cells.

To overcome the high cost of the electrocatalysts and sluggish kinetics, Pt-M (M = transition metals) alloys or core shells are usually employed to reduce the content of Pt. The introduction of M such as Molybdenum (Mo) [25,26], Ruthenium (Ru) [4,6,27], Tungsten (W) [13,28, 29], Tin (Sn) [2,10,15] etc. have demonstrated improved catalytic activities by producing hydroxyl (OH) species from H_2O at low potentials. The production of adsorbed (OH_{ads}) facilitates the oxidative removal of the carbonaceous species, unblocking the active sites known as the bifunctional mechanism. In addition, the alloys (Pt-M) result in electronic effect between the metals, by altering the electronic structure of Pt that yields weaker adsorption of oxygenated species [5,30–33]. In this study, with the aim to reduce the Pt content whilst enhancing the electrocatalytic activity, synergistic effect of manganese (Mn) and ceria (Ce) as co-catalysts towards EOR and ORR were explored with reduced Pt loading (13 wt. %).

To address the durability of the electrocatalyst; literature reports the use of more stable materials such as graphene, carbon nanotubes (CNTs), carbon nanofibres (CNFs) with high surface area and good electronic conductivity [34–36]. However, the carbonaceous materials still undergo carbon corrosion to some degree. Therefore, corrosion resistant material such as metal oxide (MO_X) and/or the composites of MO_X with carbon are often used as support materials for the catalysts. In addition, MO_X are believed to stabilize the catalyst nanoparticles on the account of the strong interaction between the MO_X and catalyst nanoparticles [37–40]. In this work, titanium dioxide (TiO_2) and doped TiO_2 (TiO_2Mn, TiO_2Ce and $TiO_2Mn_{0.5}Ce_{0.5}$) were studied as Pt catalyst support toward EOR and ORR. It is well known that South Africa holds a greater percentage of titanium (Ti) and Mn deposits compared to other countries which further informed our decision to use these abundant and low-cost materials in our study, as well as mineral beneficiation for our country's economy [41,42].

Another common strategy to improve the catalytic activity of the electrocatalysts is the use of alkaline electrolyte. Alkaline electrolyte is a milder condition relative to acidic electrolyte. It eliminates the corrosion of support materials and minimizes the dissolution of non-noble transition metals. Also, the abundance of OH species enhance the EOR and ORR by the bifunctional mechanism shown in Equation 1.1 – 1.4 [9,43].

$$Pt + CH_3CH_2OH + 3OH^- \rightarrow Pt[CH_3CO]_{ads} + 3H_2O + 3e^- \quad 1.1$$

$$MO_X + OH^- \rightarrow MO_X[OH]_{ads} + e^- \quad 1.2$$

$$Pt[CH_3CO]_{ads} + MO_X[OH]_{ads} \rightarrow CH_3COOH + Pt + MO_X \quad 1.3$$

$$CH_3COOH + OH^- \rightarrow CH_3COO^- + H_2O \quad 1.4$$

Therefore, a comparison study between sulphuric acid (H_2SO_4) and potassium hydroxide (KOH) as electrolytes was conducted for the non-carbon supported electrocatalysts to determine their activities toward the EOR and ORR.

1.3 Aim and Objectives

1.3.1 Aim

The aim of the study was to investigate the electrochemical behaviour of low-loaded platinum electrocatalysts on non-carbon support materials towards EOR and ORR.

1.3.2 Objectives

The objectives of the study were to:

i. Prepare the non-carbon supports (TiO_2, TiO_2Mn, TiO_2Ce and TiO_2MnCe) and the corresponding electrocatalysts (Pt/TiO_2, Pt/TiO_2Mn, Pt/TiO_2Ce and Pt/TiO_2MnCe)
ii. Physical characterization of the electrocatalysts using X-ray diffraction, X-ray photoelectron spectroscopy, ultraviolet visible spectroscopy, transmission electron microscopy, scanning electron microscopy and energy dispersive spectroscopy
iii. Electrochemical characterization of the electrocatalysts using cyclic voltammetry, linear sweep voltammetry, chronoamperometry and electrochemical impedance spectroscopy.
iv. Explore the sensing performance of the electrocatalyst that displays an enhanced behaviour towards EOR for the development of a fuel cell breath alcohol sensor (FCBrAS).

1.4 Scope of Research Project

Chapter 2: Literature Review

This Chapter will focus on the introduction to fuel cells, operating conditions of fuel cells and the developments (catalysts and supports) made so far will be briefly mentioned to gain an understanding of how to improve or enhance the performance and life time of the cell. The type of materials used for supports and catalysts will also be discussed. Furthermore, the basic principles and equations (where applicable) of the physical and electrochemical characterizations will be introduced.

Chapter 3: Materials and Methods

This Chapter will provide the list of materials, sample preparation methods and experimental conditions that were used. The operating conditions of the instrument used will also be provided.

Chapter 4: Results and discussions on the physical and electrochemical characterization of the synthesized supports and electrocatalysts.

The chapter presents the results and discussions on the physical characterization of the prepared supports and electrocatalysts. Furthermore, the electrochemical behaviour of the electrocatalysts in ferri-ferrocyanide ($Fe(CN)_6^{3-}/Fe(CN)_6^{4-}$) were discussed.

Chapter 5: Results and discussions on the electrochemical behaviours of the electrocatalysts towards EOR in acid and alkaline electrolytes.

In this Chapter, the results on the electrochemical behaviour of the electrocatalysts towards EOR in acid and alkaline electrolytes are discussed.

Chapter 6: Results and discussions on the electrochemical behaviours of the electrocatalysts towards ORR in acid and alkaline electrolytes.

In this Chapter, the results on the electrochemical behaviour of the electrocatalysts towards ORR are discussed.

Chapter 7: Results and discussions on the sensing performance of $Pt/TiO_2Ce/C$ towards EtOH gas.

In this Chapter the results on the sensing performance of $Pt/TiO_2Ce/C$ towards EtOH gas are discussed.

Chapter 8: Conclusion and Recommendations

The conclusion and recommendations on the performance of the synthesized electrocatalysts towards EOR, ORR and the development of fuel cell breath alcohol sensors (FCBrAS) are provided.

Chapter 2
Literature Review

2.1 Fuel Cells

Fuel cell technology was first discovered in the year 1839 by Sir William Grove. He demonstrated the use of H_2 and O_2 to produce electrical energy. In his experiment, Sir W. Grove immersed Pt electrodes in dilute acidic electrolyte (H_2SO_4) and connected to an ammeter. The H_2 and O_2 underwent electrocatalysis at the surface of the electrodes producing H_2O and current flow. Today, fuel cells employ the same principle whereby either H_2 or alcohol and O_2 are catalysed on high surface area, porous Pt electrodes, releasing electron flow through the external circuit, subsequently, generating electrical energy. Theoretically, fuel cells produce H_2O and CO_2 when the fuel of choice is H_2 and MeOH, respectively. Thus, the use of fuel cells are promising sources for green electrical energy. The different types of fuel cells are generally characterized by their operating temperature and the electrolyte in use as described in Table 2.1 [6]. The attractive properties of fuel cell technology, such as: the high energy efficiency, zero or low pollutant emissions and reliability are the driving force to the continuous and growing interest in fuel cells as energy conversion devices [3,12,44,45].

Table 2.1: The types of fuel cells [6].

Fuel Cell	Operating temperature (°C)	Electrolyte	Efficiency (%)	Applications
Proton exchange membrane fuel cell (PEMFC)	60 – 80	Perflorosulfonic acid	35 – 60	Portable, transportation and storage
Direct alcohol fuel cell (DAFC)	60 – 90	Perflorosulfonic acid	50 – 60	
Alkaline direct alcohol fuel cell (ADAFC)	90 – 100	60 % potassium hydroxide	60 – 70	Military, space
Solid oxide fuel cell (SOFC)	700 – 1000	Yttria-stabilized zirconia	60 – 85	Large distributed generation
Molten-carbonate fuel cell (MCFC)	600 – 700	Lithium and/or sodium carbonates	50 – 85	Large distributed generation
Phosphoric-acid fuel cell (PAFC)	150 – 200	Phosphoric acid	40 – 85	Distributed generation

2.1.1 Proton Exchange Membrane Fuel Cell (PEMFC)

The PEMFC comprises of a proton conducting, polymer membrane shown in Figure 2.1. H_2 is oxidized at the anode compartment, releasing protons (H^+) which are conducted through the polymeric membrane and e^- that flow through the external circuit into the cathode compartment. The O_2 is reduced by e^- and H^+ producing H_2O in the cathode compartment. The described anodic, cathodic and overall reaction processes are shown in Equation 2.1 – 2.3 [4,44,46].

$$H_2 \rightarrow 2H^+ + 2e^-, E^o = 0.00\ V\ vs.\ NHE \quad (2.1)$$

$$O_2 + 4H^+ + 4e^- \rightarrow 2H_2O, E^o = 1.23\ \text{V vs. NHE} \quad (2.2)$$

$$\text{Net reaction: } H_2 + \frac{1}{2}O_2 \rightarrow H_2O, E^o = 1.23\ \text{V vs. NHE} \quad (2.3)$$

Nafion® is a perflurosulfonic acid polymer membrane that conducts H^+ and is commonly used as an electrolyte in PEMFCs. Ideally, the membrane should be H^+ conducting and resistant to e^- flow. The electrode material consists of carbon powder (Cabot ®) supported Pt nanoparticles that are bound together by Nafion® solution. The nano-sized Pt are distributed over the large surface area carbon to expose a wide range of active sites for contact with the analyte or reactants. In addition, the carbon-supported Pt nanoparticles are often mixed with a Teflon binder and coated on gas diffusion layers (GDLs) [7]. The GDL is a carbon paper or cloth that provides mechanical structure to the electrode and will facilitate the diffusion of gas reactants (H_2 and/or O_2) to the catalyst. The GDL will also facilitate the diffusion of gaseous products (CO_2) from the catalyst. Furthermore, GDLs are carbon based materials which implies that they are electronic conductors that enable the flow of e^- from the catalyst surface to the external circuit *vis. versa*. It is also essential to achieve direct contact between the reactant-electrode-electrolyte also known as the three-phase contact to ensure the performance of the cell. To achieve this, the electrolyte is sandwiched between the two electrodes namely; anode and cathode by hot pressing (140 °C for 3 min) the three material to form a membrane electrode assembly (MEA) [7]. Although the PEMFCs are highly efficient and environmentally friendly since they eliminate the emission of CO_2, the lack of H_2 storage, transportation infrastructure, high cost of production of the fuel and high Pt content limit their commercialization. For this reason, there has been growing attention to the development of DAFCs whereby low molecular-weight alcohols such as MeOH and EtOH are used as fuel. In the next section, a brief overview of DAFCs is given [9].

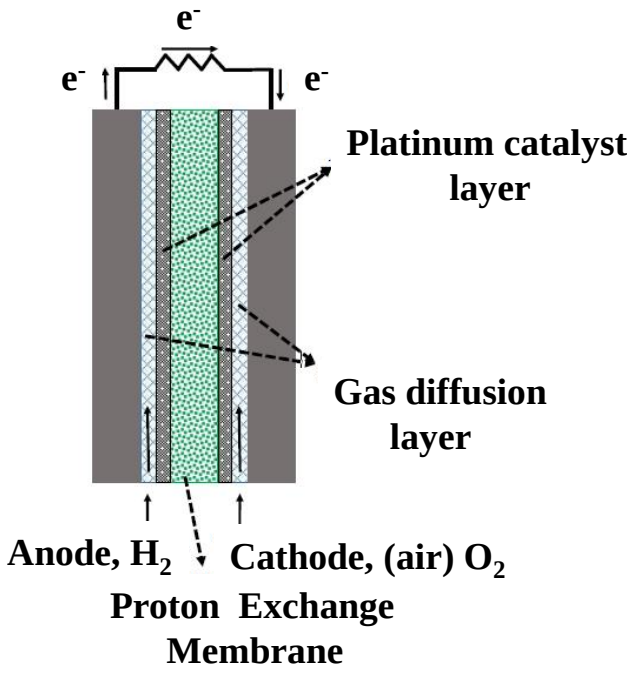


Figure 2.1: Schematic diagram of a Proton Exchange Membrane Fuel Cell [44].

2.1.2 Direct Alcohol Fuel Cells (DAFCs)

The DAFCs systems eliminates the problems of high cost production and the limited infrastructures of the H_2 storage and transportation. This is attributed to the use of alcohols unlike H_2 in DAFCs. Alcohols are easy to store and transport using the existing petroleum infrastructures [2,36]. In addition, the production of alcohols are convenient, especially EtOH which is considered renewable and sustainable since it can be produced from biomass [2,10]. The operation and applications of DAFC and PEMFC are similar. In a DAFC, alcohol such as EtOH is oxidized on the catalyst, producing H^+ and e^-. The H^+ permeate through the H^+ conducting membrane whilst e^- flow by way of the external circuit into the cathode compartment where O_2 reacts with the e^- and H^+ producing H_2O [7,12]. The schematic representation of a DAFC is shown in Figure 2.2.

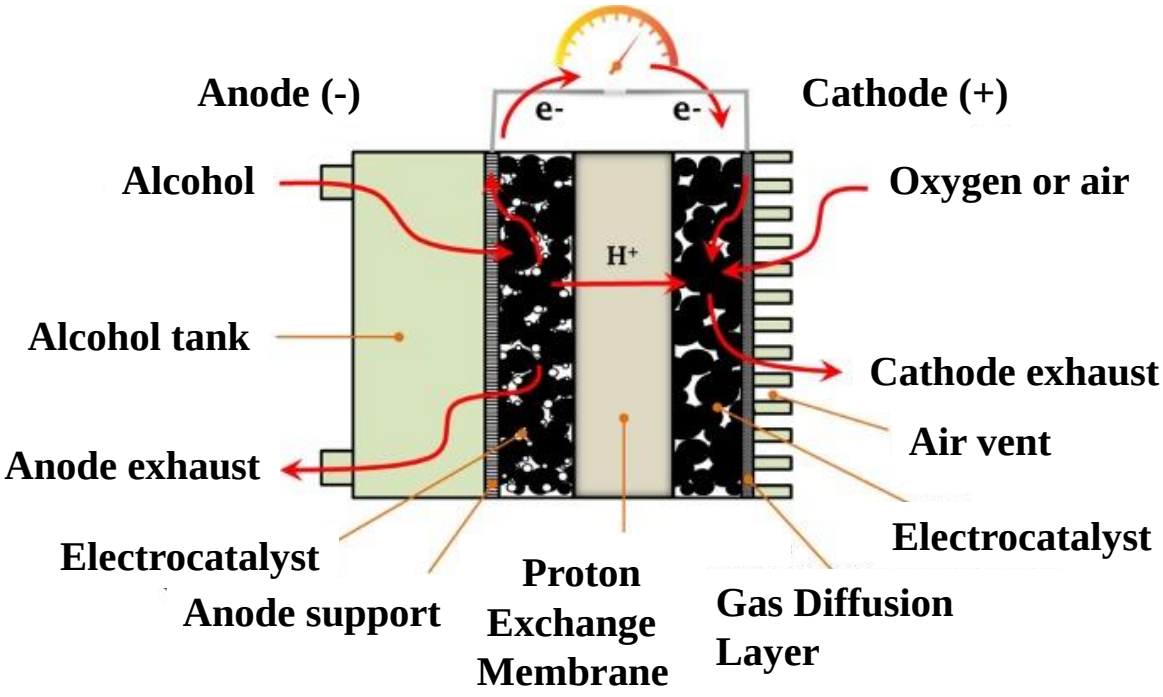


Figure 2.2: Schematic diagram of DAFC [46].

Literature reports on the use of DAFCs revealed that alcohols such as MeOH [4,33,35,36], EtOH [4,10,11,36], glycerol (Gly) [4,47,48, 49] and ethylene glycol (EG) [4, 47,48, 50] as fuels. However, DEFCs are extensively studied due to their attractive properties such as low-toxicity relative to MeOH, high energy density of 8.01 vs. 5.0, 5.2 and 6.09 kWh/kg for Gly, EG and MeOH, respectively and sustainability since it can be produced from abundant natural resources. These fuel cells consists of a proton conducting membrane as mentioned above and can also operate in alkaline electrolyte [9,11,12].

ADAFC is another type of fuel cell that employs the same set-up as a DAFC with slight modifications. Instead of H^+ conducting membrane, ADAFC consists of hydroxyl (OH^-) conducting membrane. The alcohol of interest is first oxidized in the anode compartment producing H^+ and e^-. Then e^- flow through the external circuit into the cathode compartment, reducing O_2 into OH^- which permeate across the membrane into the anode compartment. Finally, the OH^- react with H^+ to produce water [7]. The drawbacks in the use of ADAFCs is

carbonate formation in the presence of CO_2 from intermediate products and their surroundings as well as poor conductivity and stability of the membrane [7,11].

The DEFC anodic reaction is one of the main challenges with fuel cells since EtOH, unlike H_2 and MeOH is complex, requiring high overpotentials to induce oxidation. It requires the breakage of the carbon to carbon (C–C) bond to completely oxidize EtOH to CO_2. Instead, oxidation of EtOH undergoes partial oxidation to yield acetaldehyde (CH_3COH) which may further be oxidized to acetic acid (CH_3COOH), the major product. The two reactions require high overpotential and the presence of reaction intermediates and/or by-products tend to block the active sites by adsorbing to the Pt surface, further degrading the performance. The electron process for the complete oxidation to CO_2 is $12e^-$ whereas the partial oxidation undergoes $2e^-$ and $4e^-$ for CH_3COH and CH_3COOH, respectively as shown in Equation 2.4 – 2.6, respectively [51].

Complete Oxidation of EtOH:

$$C_2H_5OH + 3H_2O \rightarrow 2CO_2 + 12H^+ + 12e^-, E^\circ = 0.084 \text{ V vs. NHE} \quad 2.4$$

Partial Oxidation of EtOH:

$$C_2H_5OH \rightarrow CH_3COH + 2H^+ + 2e^- \quad 2.5$$

$$C_2H_5OH + H_2O \rightarrow CH_3COOH + 4H^+ + 4e^- \quad 2.6$$

Also, the cathodic reaction remains a challenge in fuel cells attributed to the slow kinetics of the ORR that result to high overpotentials [14,52]. In addition, the operating conditions such as: high potentials (0.6 – 1.2 V vs. RHE), acidic environment, high humidity and temperature of the cathode lead to the deterioration of the electrocatalyst components such as the carbon support. As a result, the efficiency of the fuel cell is reduced [53,54]. The ORR mechanism can undergo the direct reduction of O_2 to H_2O or a partial reduction of O_2 to hydrogen peroxide (H_2O_2) which may be further reduced to H_2O. The e^- process for complete reduction of O_2 to

H_2O is $4e^-$ whereas the partial reduction is $2e^-$ each for the reduction of O_2 to H_2O_2 and H_2O_2 to H_2O, respectively [11].

The ORR mechanisms in acidic electrolyte are shown in Equation 2.7 – 2.9.

Complete Oxygen Reduction:

$$O_2 + 4H^+ + 4e^- \rightarrow 2H_2O, E° = 1.230 \text{ V} \quad 2.7$$

Partial Oxygen Reduction:

$$O_2 + 2H^+ + 2e^- \rightarrow H_2O_2, E° = 0.695 \text{ V} \quad 2.8$$

$$H_2O_2 + 2H^+ + 2e^- \rightarrow 2H_2O, E° = 1.230 \text{ V} \quad 2.9$$

The slow kinetics of the EOR and ORR, high Pt content and poor durability of the electrocatalysts limit the commercialization of DEFCs. Thus, it is significant to develop more efficient electrocatalysts for the reactions [5,55,56].

The following section focuses on the electrocatalysts that have been explored for DAFCs.

2.2 Electrocatalyst for DAFCs

Electrocatalysts catalyze chemical reactions whereby a chemical energy conversion to electrical energy takes place over the electrocatalyst surface. Catalysts lower the activation energy that is needed for a reaction to take place, increasing the rate of the reaction at low temperatures without it being consumed [7]. In addition, electrocatalysts play a role in transportation of the electrons across the cell. Electrocatalysts in fuel cell technology are characterized as heterogeneous catalysts since they exist in a different phase compared to the reactants.

2.2.1. Platinum (Pt) and Pt-based catalysts

Currently, the widely adopted electrocatalysts for both the anode and cathode compartment are Pt or Pt-based catalysts supported on carbon black. Pt-based electrocatalysts are the most effective for EOR and ORR making them the catalyst of choice. However, due to the scarcity, high cost and the sluggish kinetics, the search for more active, stable and low-cost materials has extensively increased [2,57,58].

(i) Pt alloy and core-shells

Alloying or syntheses of core-shell Pt with other transition metals (M) (Pt-M or M@Pt) such as ruthenium (Ru), tin (Sn), molybdenum (Mo), nickel (Ni), copper (Cu), Co, Mn, are the most common strategies used to reduce the Pt content. Pt alloys and core-shells have illustrated enhanced catalytic activities in both acidic and alkaline electrolyte [16,55,59–62]. The alloy or core-shell formation of Pt with other transition metals induces the bifunctional mechanism. The bifunctional mechanism is a phenomenon where the added M acts as a co-catalyst in the electrochemical reaction whereby the M activates H_2O to produce OH^- at low overpotential. Subsequently, the OH_{ads} species facilitates the oxidation of catalyst poisoning species (CO, CH_3COH and CH_3COOH), unblocking the active sites for more reactions to take place [61,63]. This is good since the noble Pt loading can be reduced whilst the catalytic efficiency of the electrocatalyst is retained and/or improved. Furthermore, Pt alloys and/or core-shells modify the electronic structure of Pt, known as the electronic effect and as a result, the oxygenated species adsorb weakly to the Pt surface, further revealing the active sites for catalytic reactions to occur.

Several research interests also present the use of alkaline electrolyte as means to eliminate or reduce the use of Pt [10,11,51,64]. Alkaline electrolyte is milder, which grant the use of low-cost materials such as palladium (Pd), Pd-based, Ni and Co [12,51,65,66] electrocatalysts for EOR, especially for ORR, where several studies have presented the use of non-precious

electrocatalysts such as: metal oxides, carbides [67–69], metal nitrogen carbon [70,71] and nitrogen doped carbon materials [10,60,61,72,73].

(ii) Effect of Particle Size

Nano-sized particles are more active than bulk or large single crystals. This is attributed to the low co-ordination number (CN) of nano-sized particles that allows the freedom of movement by surface atoms. As a result, surface reconstruction occurs and the analyte adsorption is facile for electrochemical reactions to occur [11,44]. Furthermore, nano-sized Pt-based nanoparticles are usually distributed on high surface area support material like carbon, increasing the active surface area for the occurrence of enhanced electrochemical reactions, by this, the Pt loading can be reduced. The nanoparticle size of the catalysts is controlled by the preparation method that is used such as the alcohol, sodium borohydride reduction method or the addition of capping agents such as polyvinylpyrolidone (PVP) [11,74].

2.2.2. Catalyst Supports for DEFCs

The activity of a catalyst is not dependant on the catalyst alone. Catalyst supports play a vital role on the efficiency and durability of the electrocatalysts. Also, the efficient utilization of Pt nanoparticles relies on the strong interaction between the catalyst and the support [74]. A suitable support should preferably have the following features: (i) high surface area to allow dispersion of metal nanoparticles (large ECSA), (ii) porous channels for mass transfer, (iii) electron conductivity for electronic transfer, and (iv) durable support. However, carbon supported Pt catalysts are prone to degradation due to the severe corrosion under the fuel cell operating conditions (acidic environment, oxygen enriched cathode compartment, high overpotential, humidity and temperature). Furthermore, upon oxidation of carbon, the ECSA and stability decreases as well as an increase in micro-pore volume and hydrophobicity [40,49].

The process of the oxidation of carbon is presented in Equation 2.10 [40]:

$$C + 2H_2O \rightarrow CO_2 + 4H^+ + 4e^-, E° = 0.207 \text{ V vs. NHE} \quad 2.10$$

To overcome these challenges, the development of more stable support material to substitute and/or add to carbonaceous material has been demonstrated in several studies.

(i) Alternative Carbon Supports

Carbon materials that are less prone to corrosion in the operating conditions of fuel cells such as, graphene nanosheets or nanoflakes, carbon nanotubes (CNTs), carbon nanofibres (CNFs), onion like carbon (OLC) and carbon spheres (CS) (shown in Figure 2.3) were developed using various methods of syntheses and used as alternative support materials.

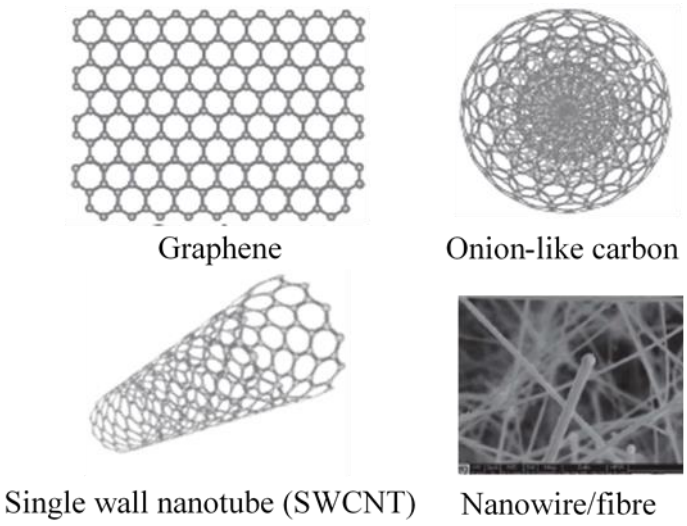


Figure 2.3: Carbon support materials [76].

The presence of carbon graphitization in these materials enhances their stability towards corrosion. Graphitic materials are sp^2 carbon atoms bonded to three adjacent carbons, forming planar hexagonal rings commonly known as graphene sheets. This is attributed to the long range ordering that is found in the graphitic materials compared to short range ordering in amorphous carbon. In addition to this, graphitized carbon consists of ordered carbon lattice, small amount of surface defects, and low adsorption of O_2 [39,77]. The graphitized carbon

supports offer other advantages such as strong anchorage of metal nanoparticles. However, these materials do not entirely eliminate carbon oxidation. Usually, corrosion occurs at the sites were free electrons are present, such as surface defects, edges and corners of basal planes. Also, pre-treatment of the graphitic carbon supports is often required to provide anchoring sites for metal nanoparticles. This lead to unfavourable long synthesis procedures and structural disorder [11,53].

Consequently, non-carbon supports known as MO_X, MC and MN are commonly used to address concerns with corrosion of carbon materials. The MO_X, MN and MC exhibit attractive properties such as resistance to corrosion, strong metal to support interaction (SMSI) and acceptable electronic conductivity [78,79]. These properties make it worthwhile to investigate non-carbon support material as catalyst support for the EOR and ORR.

(ii) Non-carbon Supports

Extensive research that involves the use of MO_X, MC, MN and MCN has been pursued to address the durability of the electrocatalysts in the operating environment of fuel cells. In some cases mixtures of these semiconductors with carbon materials are employed. Examples of non-carbon supports that are commonly studied include the use of titanium nitride (TiN), titanium carbide (TiC), titanium carbonitride (TCN), tungsten carbide (WC), tungsten oxide (WO_X), molybdenum oxide (MoO_X), cerium oxide (CeO_2), tin oxide (SnO_2) and manganese oxide (MnO_X) [11,53].

The growing attention in the use of MOx, MC, MN and MCN is due to their attractive properties. The SMSI is due to the e^- donation from the support into the metal's d-band (electronic effect). This offers improved catalytic activity since the modified d-band of Pt allows weak adsorptions of intermediate species (Pt-CO), facilitating the facile desorption, creating more active sites for the electrochemical reactions to occur. The strong interaction also alleviates the dissolution and agglomeration of nanoparticles, further enhancing the durability

and catalytic activity of the electrocatalysts. Furthermore, the use of MO_X with oxygen vacancies (O_V) near the surface induces the formation of OH_{ads} near Pt surface which activates the bifunctional mechanism [80]. The commercialization of the MO_X, MC, MN and MCN are inhibited by low surface area and low conductivity compared to the commonly used carbonaceous material [81–83]. Thus, to improve the low surface area and conductivity of non-carbon supports, common strategies such as: (i) mixing MO_X, MC, MN and MCN with carbon materials, (ii) doping the semiconducting material with other transition metal, (iii) preparation of titania sub-oxides by heat treatment in the presence of H_2 and/or carbon has demonstrated improved surface area, conductivity, stability and catalytic behaviour [84,85], and (iv) the preparation of porous structures, large surface area material with the use of soft or hard templates have been investigated [40,53,80,86].

Titanium dioxide (TiO_2)

The most commonly studied MO_X is TiO_2 nanostructured materials as support for electrocatalyst used for fuel cells. This is due to the abundance, low-cost, non-toxicity and electrochemical stability of TiO_2. However, TiO_2 has large bandgaps of *ca*. 3.2 and 3.0 eV for anatase and rutile, respectively. Rutkowska and co-workers [87] compared the use of CNT, TiO_2, TiO_2/ CNTs as support materials for platinum ruthenium (PtRu) nanoparticles to study the electrochemical behaviour towards EOR in 0.5M H_2SO_4. The addition of TiO_2 alone demonstrated enhanced electrocatalytic activity towards the EOR due to the bifunctional mechanism and an enhanced charge and H^+ mobility. The presence of Ru activated the formation of Ru-OH_{ads}, further enhancing the performance of the electrocatalyst. Upon the addition of CNT to TiO_2, the electrocatalysts conductivity increased and more anchoring points were available for PtRu nanoparticles increasing the ECSA. Furthermore, the kinetic rate constants revealed that the TiO_2 supported PtRu alone enhanced catalytic behaviour irrespective of the presence of CNT. This indicates the efficiency of TiO_2 in the study towards

EOR. In a study conducted by Ito and co-workers [35], PtRu supported on C, CNFs, TiO_2, C-TiO_2 and CNF-TiO_2 were probed for their electrochemical activity towards methanol oxidation reaction (MOR). The PtRu/ TiO_2-CNFs demonstrated the highest catalytic activity followed by PtRu / TiO_2-C indicating the synergistic effect between TiO_2 and carbon materials towards MOR.

Hybrid materials that consists of Pt/C-titania nanotubes (TNTs) were investigated for MOR. The one-dimensional (1-D) self-ordered TNTs unlike TiO_2 nanotubes electrocatalyst presented enhanced catalytic activity, due to the improved conductivity of one-dimensional (1-D) self-ordered TNTs unlike the latter as well as the presence of carbon. In addition to this, electrocatalyst demonstrated enhanced stability, high distribution of Pt across the C-TNTs support and tolerance to catalyst poisoning [88].

To address the low conductivity of the semiconducting TiO_2, strategic methods such as, the formation of sub-stoichiometric TiO_2 also known as magneli phases have been investigated. Magneli phases with the general formula (Ti_xO_{2x-1}) where $3 < x < 10$ are corrosion resistant and present high electrical conductivity. Sub-stoichiometric TiO_2 are generally prepared by reducing TiO_2 with H_2 or carbon at high temperatures (> 1000 °C) as described by several studies [39,81,53,89]. However, recent studies by Esfahani and co-workers [80,89] demonstrated the formation of Ti_3O_5 at relatively lower temperature (850 °C) under the presence of H_2 and nitrogen (N_2) as the carrier gas. The facile transition of TiO_2 to Ti_3O_5 under lower temperature was attributed to the presence of H_2 and the dopant Mo. The reported reduced bandgap correlated to enhanced conductivity of the support. Subsequently, the Pt/Ti_3O_5Mo and Pt/Ti_3O_5MoSi electrocatalyts with (15 wt. % Pt) were investigated for ORR in acidic electrolyte solution. As expected, the electrocatalysts presented enhanced electrochemical activity and stability toward ORR unlike commercial Pt/C (E-TEK) with (20 wt. % Pt). There are limited studies on the electrochemical properties of sub-stoichiometric

TiO_2 towards the EOR in acidic electrolyte. Although, sub-stoichiometric TiO_2 show appreciable catalytic activities towards ORR, no study has reported the use of dopants such as, Mn and Ce in the production of magneli phases at relatively low temperatures [40,85,90].

Ceria oxide (CeO_X) and Manganese oxides (MnO_X)

Cerium oxide (CeO_2) are commonly explored as supports with or without carbonaceous materials. As in the case with TiO_2, CeO_2 nanoparticles are known to induce the electronic effect and bifunctional mechanism [83,91,92]. For example, Pt-CeO_2/C was investigated as a potential electrocatalysts towards MOR in acidic electrolyte and compared to Pt/C. As expected, the authors reported enhanced electrochemical behaviour and stability of the Pt-CeO_2/C, unlike Pt/C. The interaction of Pt-CeO_2 induced the tolerance of the electrocatalysts to poisonous CO species [56].

A comparison between Pt/CeO_2 and unsupported Pt towards ORR demonstrated higher catalytic activity and tolerance toward MeOH crossover with Pt/CeO_2 relative to the latter, indicative of the advantage of the electronic effect (between CeO_2 and Pt) which improves the selectivity and tolerance towards methanol crossover. Hybrid materials of CeO_2 with carbonaceous materials have been studied and show improved catalytic activity as it has been postulated. For instance, Kakaei and co-workers [92] fabricated sulfonated reduced graphene oxide (SRGO) supported Pt-CeO_2 nanoparticles to evaluate the electro-oxidation of EtOH. A lower activation energy toward EOR was demonstrated with the hybrid material Pt-CeO_2/SRGO compared to Pt/SRGO. This further supports the postulation that there exists synergistic effect between CeO_2 and Pt nanoparticles in EOR.

The efficiency of the electrocatalysts can also be improved using Mn or MnO_X as hybrid or non-hybrid support for Pt-based catalysts. The MnO_X are excellent proton conductors and share the same properties as those previously discussed. In a study conducted by Ganesan and co-workers [93], Pt/α-MnO_2-C compared to two commercial catalysts (Pt/C and PtRu/C) for MOR

in 1.0 M H_2SO_4 yielded the highest catalytic behavior and stability with Pt loading of (< 25 at. %). In the ORR, Pt/MnO_2 or Pt free catalysts compared to Pt/C electrochemical results revealed promising properties. The excellent catalytic activities of MnO_2 supported electrocatalysts were highlighted by a reduced production of H_2O_2 (less than 50 %) relative to Pt/C and high efficiency of the electrocatalysts by selectively following the $4e^-$ pathway in the reduction of O_2 attributed by the accelerated decomposition of H_2O_2 by MnO_2 [94,95]. Thus, owing to the attractive properties of the Mn, Ce and TiO_2, it is worth investigating the synergistic effect of Mn and Ce in TiO_2 as supports for Pt nanoparticles towards the EOR and ORR in acidic and alkaline electrolyte.

2.3 Material Characterization

Physical characterization techniques were used in this study to determine the physical-chemical properties of the materials. These were conducted to establish the morphologies, nanoparticle sizes, structures, optical properties of the materials, elemental and surface compositions. Herein, the experimental techniques used for physical evaluation are described briefly.

2.3.1 Powder X-Ray Diffraction (PXRD)

PXRD is used to identify the structural information of the analysed material. Physical properties such as, the crystal structure, degree of crystallinity, phases, average particle sizes and lattice parameters can be deduced from PXRD. A typical XRD measurement depends on the interaction of a single wavelength X-ray beam from a cathode ray tube with a crystal lattice in a sample being analysed. The incident X-ray beams interact with a regular arrangement of atoms and diffraction occurs. The diffracted radiation consists of wavelengths that are representative of the atoms that are present in the sample. This implies that the diffraction pattern is a representative of the atoms present in the sample [96,97]. The incident rays and sample interaction can either interfere constructively or destructively. The constructive

interference occurs under conditions satisfying the Bragg's law (Equation 2.11) [98], producing a sharp interference maxima with a symmetry that is similar to the distribution of atoms in the sample. As the sample rotates and a range of angles are scanned, the detector collects and processes the diffracted X-ray signal, and an out-put is displayed on a computer connected to the instrument.

$$n\lambda = 2d\,sin\,\theta \qquad 2.11$$

Where *n* is the diffraction order, λ is the wavelength of the X-ray source (0.154060), *d* is the distance between the lattice planes and θ is the diffracted angle.

As mentioned above, the average particle sizes can be determined from the PXRD pattern and the Debye-Scherrer equation (Equation 2.12) [83,99]:

$$D = \frac{\kappa\lambda}{\beta Cos\theta} \qquad 2.12$$

where κ (0.9 used in this work) is the dimensionless shape factor, λ is the wavelength of the X-ray source, *D* is the average particle size, β is the full width at half maximum (FWHM) and θ is the angle of the peak. The particle sizes are estimated by measuring the broadness of a peak of interest from the analysed sample. The peak width at half-maxima is inversely proportional to the particle size. Therefore, broader peaks indicate small sized particles and amorphous material, whilst narrow or sharp peaks indicate highly crystalline material.

The lattice parameter (a_o) was calculated using Equation 2.13 that is shown below [98]:

$$a_o = d\sqrt{(h^2 + k^2 + l^2)} \qquad 2.13$$

Where *h*, *k* and *l* are Miller indices of a crystal facet and *d* is the distance between the lattice planes.

2.3.2 Raman Spectroscopy

Raman Spectroscopy is used to identify the molecular structure of the analysed sample by determining their unique vibrational modes. During a measurement of the sample, a single wavelength light interacts with the electron cloud of the sample, resulting in the polarization of the molecule. This produces dipole moments and periodic oscillations having a unique frequency. The relaxation of high energy vibrations results to the emission of photons that can either possess more or less energy compared to the incident photon and this process is known as the inelastic scattering. When the emitted photon contains less energy, the process is known as the Stokes scattering. Alternatively, an emitted photon with more energy results to a process known as the Anti-Stokes scattering. The emitted photons of the single wavelength light contains characteristic frequencies that can provide structural information of the analysed sample [100]. Therefore, the measured frequencies from the scattered lights emitted, represent the species contained by the sample. In this work, the Raman analysis was used to determine the effect of the heat treatment on the support materials under reducing atmosphere.

2.3.3 Ultra-violet Visible Spectroscopy (UV-vis.)

UV-vis spectroscopy can be used to characterize substances for the identification of functional groups or analytes present in a sample. It is also used to determine the concentration of solutions, nanoparticles sizes and optical properties of semiconductors. In a UV-vis. measurement, a light source such as the deuterium and tungsten lamp provides an UV and visible radiation. Thereafter, a monochromator filters the light to monochromatic radiation. The radiation is passed through a narrow slit followed by a cuvette that contains the sample being analysed. The intensity of the radiations after absorption or reflectance by the solution are detected and measured. As a result, the output spectra of absorbance as a function of wavelength are displayed on the computer connected to the spectrometer [101]. UV-vis.

analysis was used to study the optical behaviour of the support materials and the spectra were converted to a Tauc plot from which the band gap values were acquired.

2.3.4 Scanning Electron Microscopy (SEM)

SEM is a non-destructive characterization technique that is used to determine the surface morphology and elemental composition of the analysed sample. The out-put is high-resolution images of the sample surface. In a SEM measurement, a focused beam of electrons are scanned over the sample. Upon the interaction of the electrons with the sample, a loss of energy occurs and is emitted in the form of secondary electrons, back-scattered electrons and X-rays, providing signals. The signals are detected and processed, producing images that represent the surface of the sample in sizes ranging from nanometer to micrometer scale [98]. The secondary electrons are used to analyse the surface topography since they are emitted from a few nanometers within the samples. This implies that, secondary electrons possess low energy unlike back-scattered electrons which are emitted from deep within the sample, and therefore contain high energy. The ability of back-scattered electrons to be emitted from deep within the sample, allows the analysis of the bulk properties and elemental composition of the sample [100,102].

2.3.5 Energy Dispersive Spectroscopy (EDS)

EDS is a technique that identifies and quantifies the elemental composition of the sample being analysed. The EDS detector is usually coupled to SEM or TEM and detects the X-rays that are produced from the interaction of an electron beam with a sample. The emitted X-rays possess specific amounts of energy and wavelength that are related to each specific element. Thus, the elemental composition of the sample may be determined from the obtained signals. After the capturing of SEM images, the EDS is performed to estimate the content of each element in the samples [102].

2.3.6 Transmission Electron Microscopy (TEM)

TEM provides information of nanomaterials at an atomic scale, aided by the enhanced image resolution when compared to the SEM. In a TEM imaging process, the sample is irradiated with a high voltage beam of electrons that are produced from the electron gun. First, the electrons are generated through the use of emission or thermionic processes. Then, the electron beam passes through condenser lenses and apertures and is focused onto a small area the sample. An interaction between the electron beam and the atoms present in the sample occurs, resulting in inelastic and elastic scattering from which parts of it are collected and focused by the objective lens. As a result a representative electron image of the analysed sample is projected on the fluorescent viewing screen. Also, the images can be recorded by the charge-coupled-device (CCD) camera and viewed on the computer screen [103].

2.3.7 X-Ray Photoelectron Spectroscopy (XPS)

XPS is used to identify the elemental surface composition, chemical and electronic states of the surface of a material within 2–10 nm depth. The XPS measurement consists of irradiating the material of interest with X-ray beam from the aluminium (Al) or Magnesium (Mg) radiation source. This results in the emission of photoelectrons from the core-levels into the vacuum of the instrument, where the kinetic energy is detected and measured by the electron energy analyser. As a result, the binding energy of the emitted electrons can be determined. Since each emitted electron has its' unique binding energy. This implies that the measured kinetic energies are representatives of a specific elements that are present in sample. All elements, (excluding hydrogen (H) and helium (He)) can be detected by the technique. Previous standard binding energies of most elements have been determined and can be used for qualitative analysis. Also, information about the chemical states of the elements can be determined. For example, the oxidation of an element is usually identified by a positive shift binding energy or loss in the kinetic energy of the core electrons [100].

2.4 Electrochemical Characterization Techniques

Electrochemical characterization techniques were used to characterize the electrochemical performance of the electrocatalysts. Herein, the experimental techniques used for electrochemical evaluation are described briefly.

2.4.1 Cyclic Voltammetry (CV)

Cyclic voltammetry is an essential technique that is used to study the electrochemical reduction and oxidation (redox) reactions that occurs on the electrode surface. Firstly, the potential is cycled from a low to high potential in the forward scan. Then, the potential is switched and swept from the high to low potential in the reverse scan, at a constant scan rate. The resultant faradaic response is measured against potential on the Potentiostat. The current-potential curve is referred to as the cyclic voltammogram. The rate at which faradaic process occurs on the surface of the electrode is governed by mass transfer. Mass transfer is described by the movement of reduction-oxidation species from an electrolyte solution to the electrode surface and vice versa under an applied potential. There are three types of mass transfers known as; migration, diffusion and convection processes [104]. Where:

- Diffusion is the movement of species from the bulk electrolyte solution, the high concentration region to the electrode surface with low concentration.
- Migration is the movement of charged species under an electrical field.
- Convection is the transport of species influenced by hydrodynamic forces such as: stirring.

Ideally, the study towards EOR undergoes the diffusion mechanism since there is no hydrodynamic force involved. Additionally, the migration mechanism is negligible since excess supporting electrolyte solution is used. The electrochemical behaviour of the electrocatalysts towards ORR undergoes the convection mechanism, which will further be

discussed in Section 2.4.6. Therefore, the current-potential signal obtained during CV experiments are as a result of the occurrence of faradaic processes on the electrode surface attributed to the mass transport of species from the electrolyte. In addition, CV can acquire other information like the diffusion coefficient (*D*) of the electroactive species, active area (*A*), rate constants (*k*), kinetic parameters and concentration of the redox species (*C*) [104].

A typical CV for Pt-based catalysts in 0.5 M H_2SO_4 is shown in Figure 2.4. The potential regions labelled are due to (i) hydrogen adsorption/desorption, (ii) double-layer, (iii) Pt-O oxidation (Pt-O) and/or Pt-OH formation and (iv) Pt-O reduction.

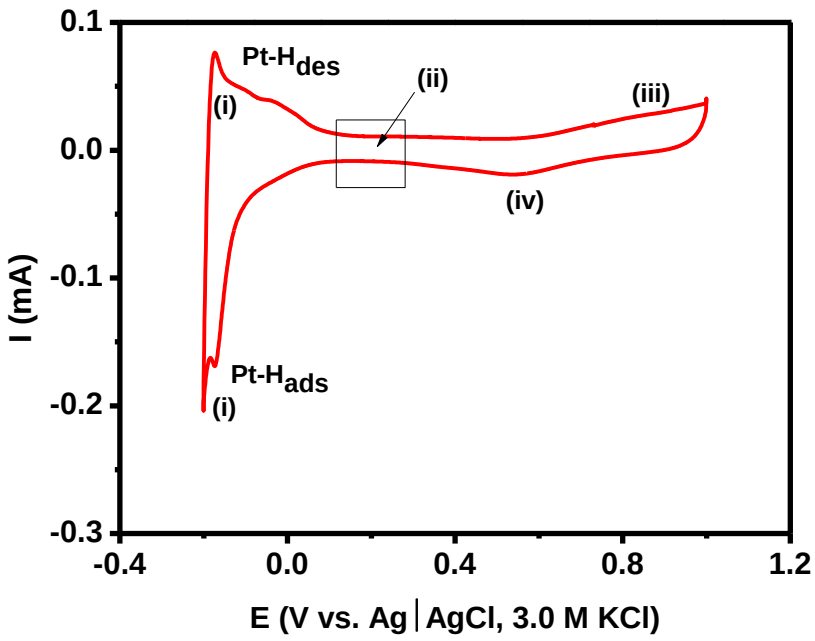


Figure 2.4: Cyclic voltammogram of carbon supported Pt catalyst in 0.5 M H_2SO_4.

The electrochemical active surface area (ECSA) of the Pt based electrocatalyst are determined from the hydrogen adsorption (H_{ads}) or desorption (H_{des}) peak since it is assumed that one metal atom adsorbs one hydrogen atom. By integrating this peak, the charge required to adsorb a monolayer of hydrogen or desorb hydrogen on the Pt surface can be calculated and substituted in Equation 2.14 to determine the ECSA of the electrocatalyst [105]:

$$ECSA\ (cm^{-2}g_{Pt}{}^{-1}) = \frac{Q_{H_{ads/H_{des}}}\ (\mu C\ cm^{-2})}{Q_H(\mu C\ cm^{-2}) \times m_{Pt}\ (g_{Pt}\ cm^{-2})} \quad 2.14$$

Where $Q_{Hads/Hdes}$ is the charge integrated from the H_{ads}/H_{des} peak, Q_H is the charge required to adsorb a monolayer of hydrogen on the platinum surface (210 C μC cm^{-2}) and m_{Pt} is the metal loading of Pt on the electrode [80].

2.4.2 Cyclic Voltammetry (CV) and Ethanol Oxidation Reaction

CV is also used to study the oxidation reaction of ethanol. Figure 2.5 displays a CV of Pt/C in 0.50 M H_2SO_4 containing 0.50 M EtOH. Firstly, the potential is swept from the lowest value in the anodic scan and current begins to increase (E_{onset}) with change in potential due to the oxidation of fresh ethanol molecules. Followed by a peak current (i_{fp}) at the forward peak potential (E_{fp}) of 0.76 V. The current begins to decrease at > 0.76 V, due to the depletion of the analyte at the surface of the electrode and the saturation of the electrocatalyst by the adsorbed reaction intermediate species. After the switching potential, the potential is swept in the cathodic direction and as seen from Figure 2.5, there is an increase in current. This peak is associated with the oxidation of the carbonaceous species adsorbed during the forward scan. Thus, a peak current (i_{rp}) at the reverse peak potential (E_{rp}) 0.48 V is observed. The activity of an electrocatalysts is measured by the parameters E_{onset}, i_{fp} and $i_{fp}/i_{rp,}$ whereby the lowest E_{onset} potential demonstrates a low overpotential that is required to oxidize ethanol. High i_{fp} indicates the fast kinetics of the electrocatalysts for the analyte and i_{fp}/i_{rp} ratio that establishes the ability of the electrocatalyst to tolerate towards the reaction intermediate carbonaceous species (the bigger the value, the more tolerant it is to carbonaceous species) [10,92,105].

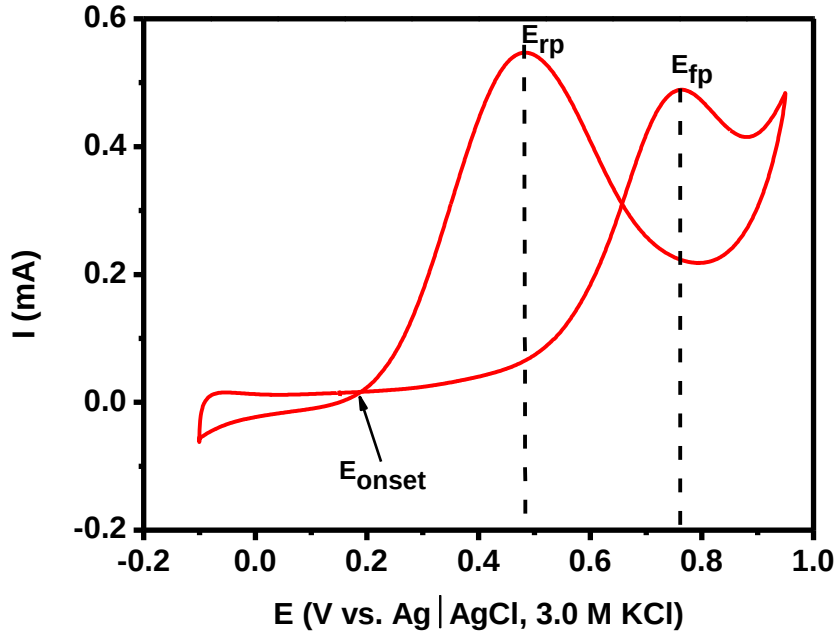


Figure 2.5: Cyclic voltammogram of Pt/C catalyst in 0.5 M H_2SO_4 + 0.5 M EtOH.

2.4.3 Linear Sweep Voltammetry (LSV)

In this experiment, the potential is swept linearly at a constant scan rate with time. As a result, the current produced against potential is measured by the Potentiostat (shown in Figure 2.6). In the presence of the analyte (EtOH in this study), the positive scan begins at the initial potential, E_i = 0.00 V, and the oxidation of EtOH is not observed. As the potential increases (E > 0.00 V), the oxidation of EtOH began and the current increased. Subsequently, the concentration of EtOH on the surface of the electrode reduced with an increase in potential. The maximum current was reached at peak potential, E_p = 0.68 V. At this point, the concentration of EtOH on the surface of the electrode has depleted and the current decreases with an increase in potential until the final potential, E_f = 0.85 V is reached.

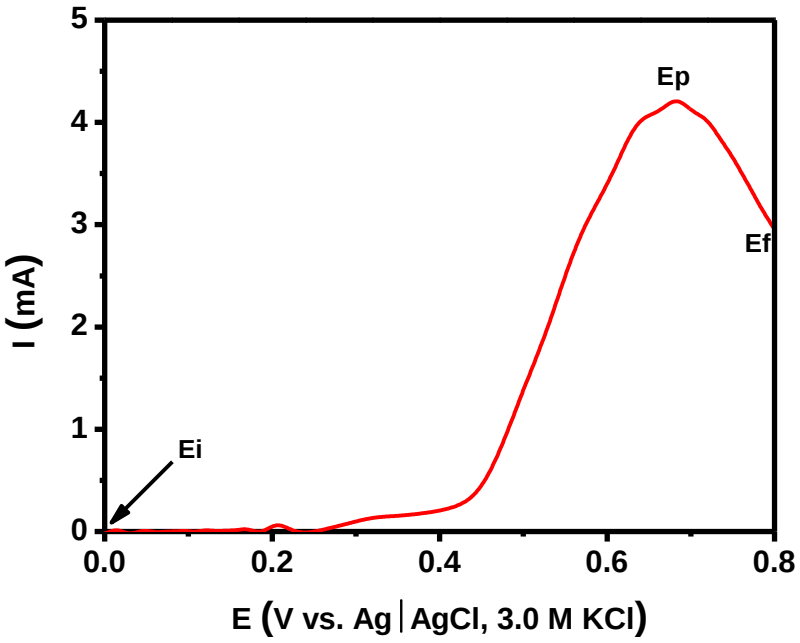


Figure 2.6: Linear sweep voltammogram of Pt/C in 0.5 M H_2SO_4 + 0.5 M EtOH.

2.4.4 Chronoamperometry (CA)

The chronoamperometry technique is used to study the electrochemical process that takes place at the surface of the electrode by polarizing the working electrode (WE) at a fixed oxidizing or reducing potential. Firstly, a fixed potential is applied and at that instant the oxidation or reduction of the electroactive species occurs, producing a maximum current. The electroactive species concentration gradually decreases at the surface of the electrode leading to a continuous flow of the species towards the electrode surface and the observed current is ascribed to the concentration of the species at the electrode surface [104]. With the increase in time, the current decays as a result of depletion of the reduction-oxidation species at the electrode surface as depicted in Figure 2.7.

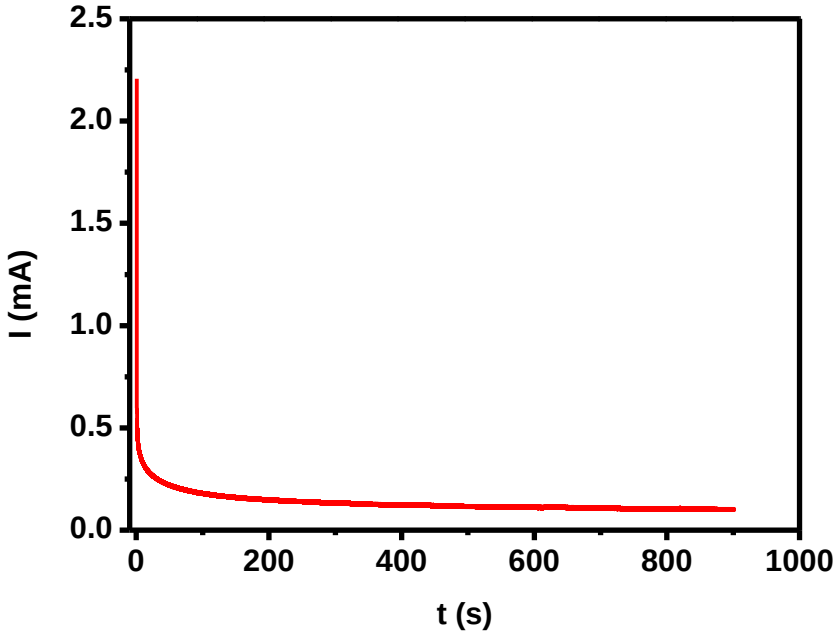


Figure 2.7: Current time curve for carbon supported Pt catalyst in 0.5 M H_2SO_4 + 0.5 M EtOH, polarized at an oxidation potential of 0.75 V for 900 s.

2.4.5 Electrochemical Impedance Spectroscopy

EIS is used to establish the electrode/electrolyte interface process as a function of the applied frequency. The information that is acquired from EIS includes: the solution resistance (R_s) charge transfer resistance (R_{ct}), double layer capacitance (C_{dl}), Warburg or diffusion resistance (W) and inductance (L) of the electrocatalyst. During the EIS measurement, a small-amplitude sinusoidal voltage perturbation of ca. 5-10 mV is applied at a particular frequency range and the impedance response is recorded by the Potentiostat. The collected EIS data can be presented in a form of a Nyquist plot shown in Figure 2.8. At the high frequency region, R_s is observed. At the low frequency regions, the R_{ct} and the linear portion known as W that is attributed to the diffusion of the redox species diffusing towards and away from the electrode surface. The mid-frequency regions present the C_{dl} or constant phase element (CPE) [104]. The experimental EIS spectra are usually fitted using equivalent electrochemical circuit (EEC) to evaluate the

electrolyte|electrode interface interactions. An example of the EEC is the Randle's electrochemical circuit shown in Figure 2.9 that was used to fit the Nyquist plot in Figure 2.8.

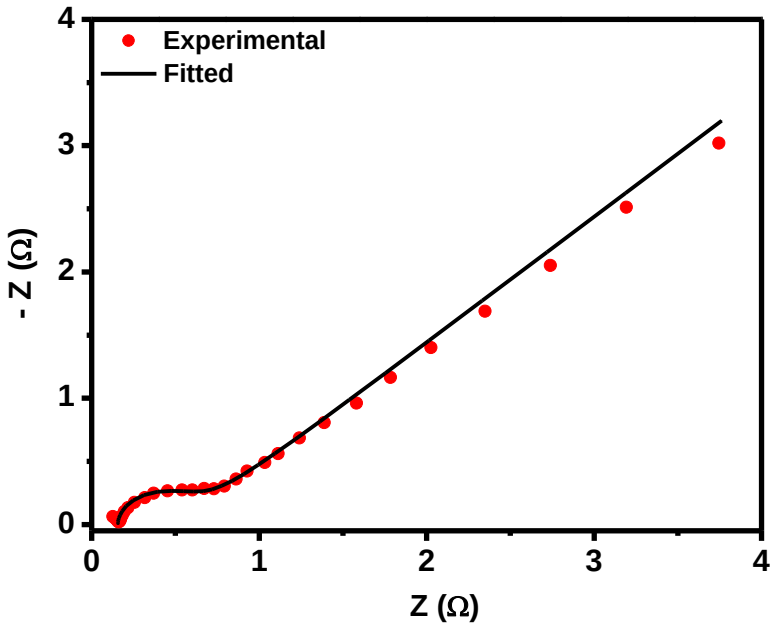


Figure 2.8: The EIS Nyquist plot for GCE in 0.1 M KCl containing 3.0 mM $[Fe(CN)_6]^{3-/4-}$ polarized at open circuit potential (OCV) 0.30 V vs. Ag|AgCl, 3.0 M KCl, from 0.1 Hz to 100 kHz.

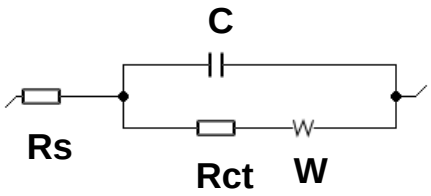


Figure 2.9: The corresponding equivalent electrochemical circuit of a GCE.

2.4.6 Rotating Disc Electrode (RDE) and Oxygen Reduction Reaction

Rotating disk electrode is an electrochemical technique that uses convection diffusion to transfer the reactant species in the electrolyte solution to the working electrode [106]. Potential is applied to the electrode at various rotation speeds (400 – 2500 rpm) and the resultant current

is measured by the Potentiostat. The WE is connected to a motor that rotates during a measurement at a certain frequency. During a measurement, the reactants are transported towards the working electrode and diffuses through diffusion layer. Thereafter, reduction of the reactant species occurred and the corresponding current is recorded. Then the products are swept away from the electrode into the electrolyte solution whilst fresh reactant molecules are transported continuously. The kinetics of the electrochemical process that occur on the surface of the electrode can be determined from the resultant LSVs (shown in Figure 2.10). The limiting current density (j_d) increases with an increase in rotation speed of the electrode [106,107]. The activity of the electrocatalyst is determined from the values of the E_{onset}, $E_{1/2}$ and j_d whereby, a more positive E_{onset} and $E_{1/2}$ demonstrated enhanced activities. Also, high value of j_d indicates faster kinetics on the surface of the electrode [38,108].

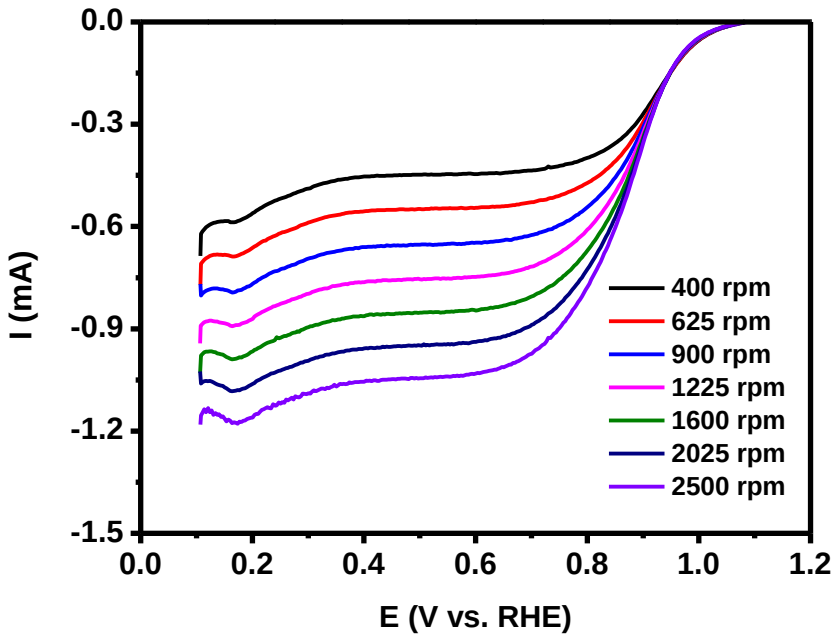


Figure 2.10: Linear Sweep Voltammograms of Pt/C in O_2 saturated 0.50 M H_2SO_4.

The Koutecky-Levich (K-L) equation shown in Equation 2.15, expresses the current density at a particular voltage and rotation speed.

$$\frac{1}{j} = \frac{1}{j_d} + \frac{1}{j_k} = \frac{1}{\beta\omega^{1/2}} + \frac{1}{j_k} \quad 2.15$$

Where $$\beta = 0.21\, nFC_o(D_o)^{2/3}\gamma^{-1/6} \quad 2.16$$

And j is the measured current density, j_d the diffusion-limiting current density, j_k the kinetic current density, n is the number of electrons, F is the Faraday constant, C_{O2} is the oxygen concentration, D is the diffusion coefficient, γ is the kinematic viscosity at room temperature (25 °) in acid and alkaline electrolyte respectively and ω is the rotation speed [107,109].

The plot of j^{-1} vs. $\omega^{-0.5}$ is referred to as the K-L plot that displays linear plots with a slope β and y-intercept j_k^{-1}. The electrocatalyst efficiency towards the ORR process can be determined from the KL plot by calculating the n values for the ORR whereby a four electron process indicates a more efficient electrocatalyst by reducing the reactants completely and the two electron process indicates an incomplete reduction of the reactants [38].

Chapter 3
Materials and Methods

3.1 Chemicals

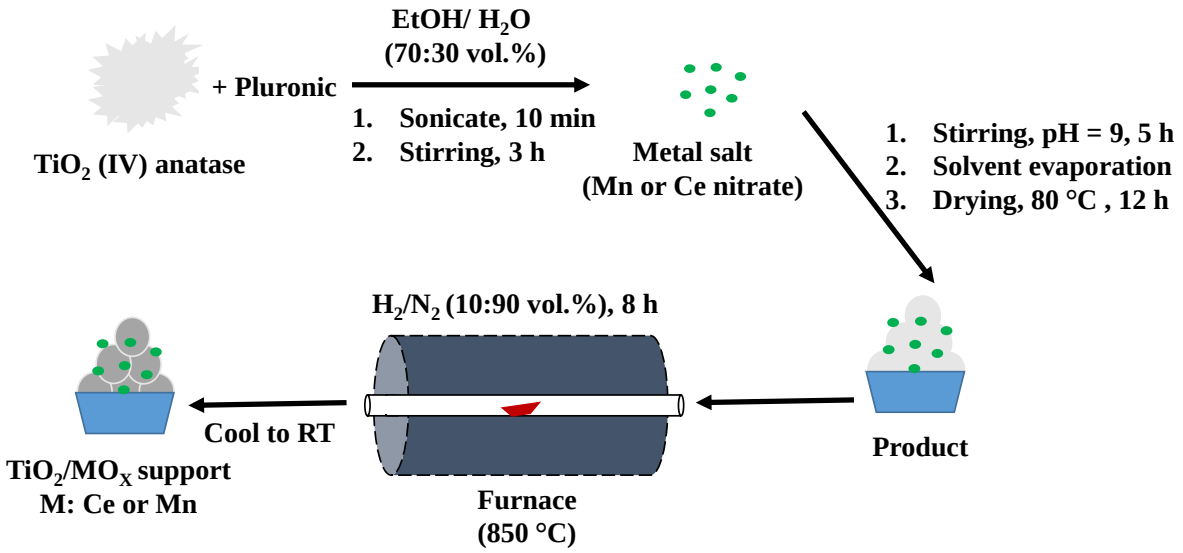
Titanium dioxide (TiO_2) (IV) anatase was purchased from PAL chemicals, Pluronic® F127, tetrachloroplatinate (K_2PtCl_4), manganese nitrate tetrahydrate ($Mn(NO_3)_2{\cdot}4H_2O$), cerium nitrate hexahydrate ($Ce(NO_3)_3{\cdot}6H_2O$) and Nafion® perfluorinated resin solution (5 wt.% mixture in lower aliphatic alcohols) were purchased from Sigma Aldrich. Ethanol (C_2H_5OH, 99 %) and isopropanol (IPA, 99 %) were purchased from MK chemicals. Ammonia solution (NH_4OH, 25%), sulfuric acid (H_2SO_4, 98 %), potassium hydroxide pellets (KOH) were purchased from ACE. Nitrogen (N_2) and H_2 gas were supplied in cylinders by Afrox (South Africa). The aqueous solutions were prepared with the use of ultra-pure water obtained from Millipore Milli-Q system (resistivity: 18.2 MΩ cm)

3.2. Methods

3.2.1 Synthesis of Support Material

The TiO_2 based supports were prepared using previously described method with slight modifications [80]. Three equivalents of TiO_2 (IV) anatase was dispersed in a mixture of ultra – pure water and ethanol (30:70 vol. %) followed by ultra-sonication for 10 mins. Then 2 wt. % of the Pluronic F127 surfactant was added to the stirring mixture and left for 3 hours at ambient temperature. For the preparation of different metals-doped TiO_2 support materials (TiO_2Mn, TiO_2Ce and $TiO_2Mn_{0.5}Ce_{0.5}$), one mole equivalent of $Mn(NO_3)_2{\cdot}4H_2O$, $Ce(NO_3)_3{\cdot}6H_2O$ and half mole equivalent of the $Mn(NO_3)_2{\cdot}4H_2O$ and $Ce(NO_3)_3{\cdot}6H_2O$ were added respectively to the TiO_2 (IV) anatase suspension, followed by pH adjustment to 9 with the use of NH_4OH. The resulting mixture was left to stir for 5 hours at ambient temperature.

Thereafter, the solvent was evaporated and further dying took place at 80 °C for 12 hours. The obtained powders were annealed at 850 °C, for 8 hours under H_2 and N_2 gases flow (10:90 vol. %). The support materials were treated with H_2 during preparation as an attempt to produce titanium sub-oxides which are known to have reduced band gap and acceptable electronic conductivity [43,77,81]. The prepared support materials were referred to as TiO_2, TiO_2Mn, TiO_2Ce and $TiO_2Mn_{0.5}Ce_{0.5}$ respectively. The syntheses procedure is summarized in Scheme 3.1.

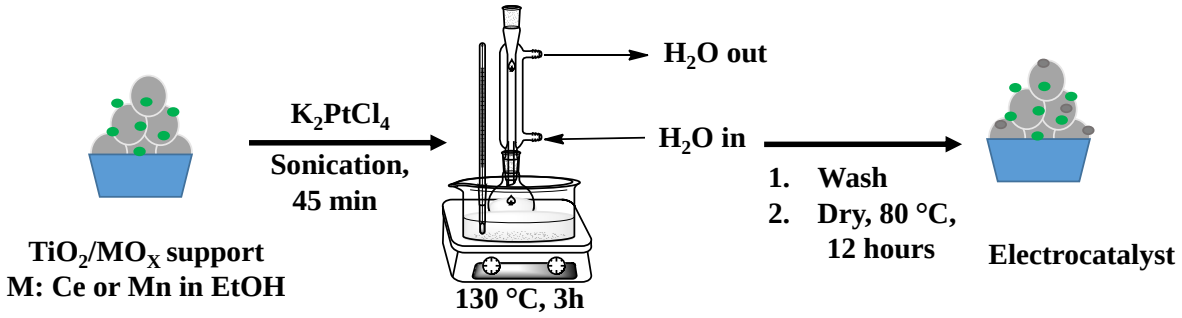


Scheme 3.1: Synthesis of the support materials.

3.2.2 Synthesis of Electrocatalyst Materials

The electrocatalysts were prepared by a modified alcohol reduction method previously reported [81]. The pre-determined mass of the TiO_2 based supports was dispersed in EtOH followed by sonication for 45 minutes. Then, (0.075 mmol; 31.4 mg) of the K_2PtCl_4 previously dissolved in ultrapure water was added into the TiO_2/EtOH suspension in a dropwise manner. The resultant mixture was refluxed at 130 °C for 3 hours, allowed to cool to ambient temperature and centrifugally washed with ultra-pure water for 5 cycles at 4500 rpm. Finally, the obtained

solid was dried in an oven at 80 °C for 12 hours. The syntheses procedure is summarized in Scheme 3.2.



Scheme 3.2: Synthesis of the electrocatalysts.

3.3 Physical Characterization

3.3.1 Powder X-Ray Diffraction (PXRD)

Powder X-Ray Diffraction (PXRD) patterns were recorded on Bruker D2 Phaser powder X-ray diffractometer with a copper (Cu) Kα (λ = 0.154060 nm) radiation X-ray source, operating at 30 kV and 10 mA. The samples were ground into a fine powder using an agate mortar and pestle, mounted onto the sample holder and flattened with a glass plate. The patterns were collected between 2θ values of 10 ° and 90 ° with a step size of 0.026 °. Thereafter, the XRD patterns were identified by using the inorganic crystal structure database (ICDD). The average crystallite sizes and lattice parameters of Pt were estimated from FWHM of the (1 1 1) peak.

3.3.2 Raman Spectroscopy

The Raman spectra were acquired from Horiba LabRAM HR Raman spectrometer equipped with an Olympus BX41 microscope. A 514.5 nm line of a Lexel Model 95 SHG argon ion laser was used and data was captured using LabSpec v5 software. The Raman analysis were performed at the University of the Witwatersrand (Physics department).

3.3.3 Ultra-violet Visible Spectroscopy (UV-vis.)

The UV-vis. spectra were recorded with Specord®210 Plus (analytikjena) UV-vis. spectrometer in the wavelength of 200–800 nm. For the sample preparation, 2 mg of the support material was sonicated in 2 ml of H_2SO_4 (98%) for 3 hours. The resulting solution was filled up to 10 mL with ultra-pure water. A 20 vol. % H_2SO_4 was prepared and used as blank solution.

3.3.4 Scanning Electron Microscopy (SEM)

The morphology and elemental composition of the materials studied in this work were characterized using SEM, (LEO 1525 SEM instrument operating at EHT = 10 kV and a working distance of 5.00 mm. For the sample preparation, a double-sided tape was taped onto the aluminium specimen stud and small quantities of the powders were scattered onto the sticky carbon tape. Finally, the samples were coated with two layers of carbon, to mitigate the charging of the sample that would result to poor image quality. The SEM analysis were performed at the National Metrology Institute of South Africa (NMISA).

3.3.5 Energy Dispersive Spectroscopy (EDS)

A LEO 1525 SEM instrument coupled with an OXFORD INCA EDS detector was used to perform EDS for the materials in this work. The EDS detector was used to evaluate the elemental composition of the samples and the analyses were performed at the National Metrology Institute of South Africa (NMISA).

3.3.6 Transmission Electron Microscopy (TEM)

A FEI Spirit 120 kV TEM was used to determine the surface morphology of the materials. The samples were prepared by dispersing a 0.5 mg of the sample in 3 mL of isopropanol followed by ultra-sonication for 30 minutes. Thereafter, a small volume (a drop) of the solution was dropped onto a lacey carbon TEM grid and was left to dry under air for 30 minutes.

3.3.7 X-Ray Photoelectron Spectroscopy (XPS)

The XPS analysis were conducted using Thermo ESCA lab 250Xi spectrometer with monochromatic Al Kα (1486.7 eV). For the sample preparation, the powers were scattered onto a carbon tape. The XPS tests were performed and analysed at NMISA.

3.4 Electrochemical Characterization

3.4.1 Cells, Electrodes and Sample Preparations

Three-electrode electrochemical cell used for $K_3[Fe(CN)_6]$/ $K_4[Fe(CN)_6]$ and EOR experiments

The experiments were conducted using a three-electrode cell shown in Figure 3.1 which was connected to a Bio – Logic VMP300 Potentiostat. All experiments were conducted at room temperature (25 °C). A glassy carbon electrode (GCE) with a diameter of 3.0 mm, Pt rod and Ag|AgCl (3.0 M KCl) were used as the WE, counter electrode (CE) and as reference electrode (RE), respectively. All potentials are referred to as Ag|AgCl (3.0 M KCl).

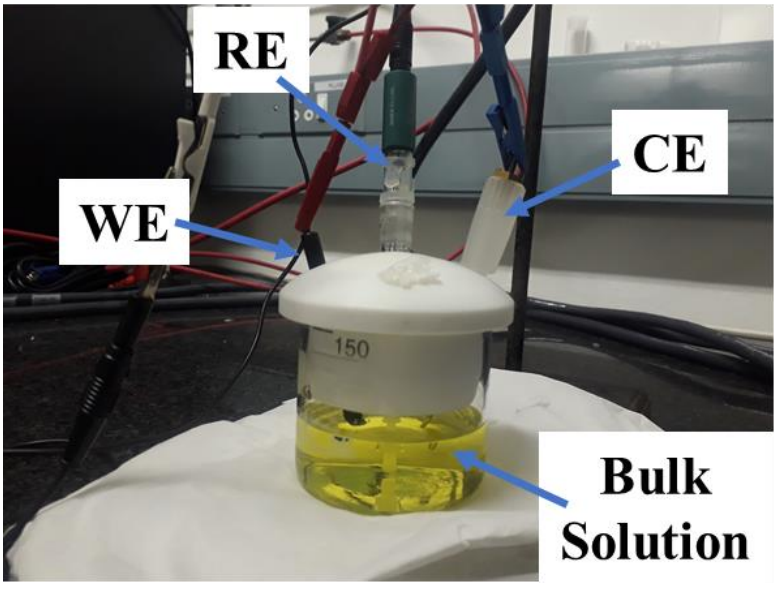


Figure 3.1: A three-electrode cell used for $K_3[Fe(CN)_6]$/ $K_4[Fe(CN)_6]$ and EOR experiments.

Ink and Working Electrode Preparation

Firstly, the WE was polished with alumina slurry followed by rinsing with ultra-pure water. Each electrocatalyst ink was prepared by dispersing 3.5 mg of the electrocatalysts powder in (50:50 vol. %) of ultrapure water (H_2O) and isopropanol (IPA) and 30 µL of (5 wt. %) Nafion® followed by sonication for 1 hour. The electrocatalyst inks were left overnight to ensure that all samples are thoroughly dispersed in the alcohol and water mixture before use. Then, an aliquot of the sonicated ink was pipetted onto the clean and dry GCE to yield 0.063 mg_{Pt} cm^{-2}. The ink was dried at an ambient temperature.

Three-electrode electrochemical cell used for ORR

The RDE experiments were conducted using a three-electrode cell shown in Figure 3.2 which was connected to a Potentiostat. The rotating disk electrode (RDE) with a diameter of 5.0 mm was used as the WE. The Pt rod and Ag|AgCl (3.0 M KCl) were used as the CE and RE. All potentials for the ORR experiments were referred to as reversible hydrogen electrode (RHE) and the experiments were conducted at room temperature (25 °C).

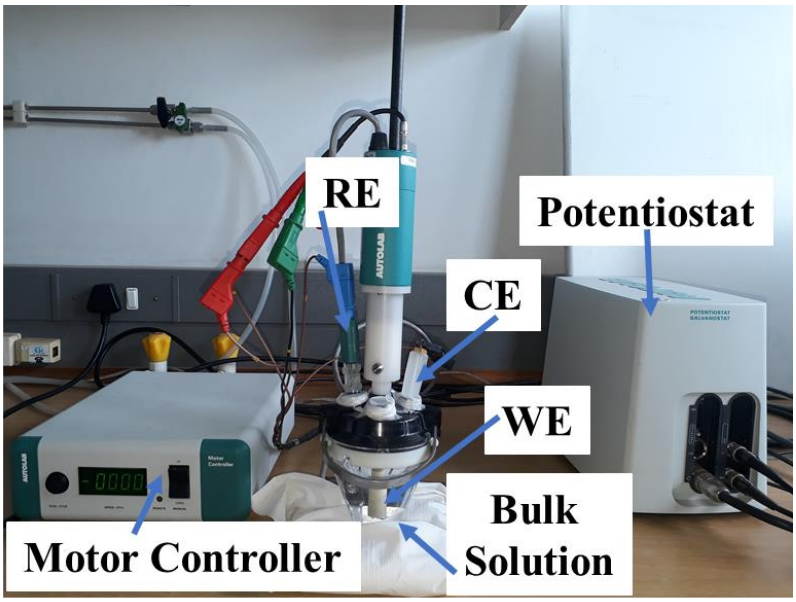


Figure 3.2: A three-electrode cell used for ORR rotating disc electrode experiment.

Ink and Working Electrode Preparation

The same ink preparation method described above was used for the evaluation of ORR. An aliquot amount equivalent to 0.022 mg_{Pt} cm^{-2} was drop-casted onto a clean and dry 5 mm glassy carbon RDE. Thereafter, the ink was dried at an ambient temperature.

3.4.2 Cyclic Voltammetry (CV)

Electrochemical measurements were conducted in nitrogen (N_2) purged electrolyte solutions (0.50 M H_2SO_4 and 0.50 M KOH separately) for the determination of the electrochemical surface area (ECSA) of the electrocatalysts. Firstly, a minimum of five CV cycles were collected between at 50 mVs^{-1} as a background. Then, three CVs at a scan rate of 25 mVs^{-1} was collected and the third scan was used for the determination of the ECSA.

3.4.3 Cyclic Voltammetry (CV) and Ethanol Oxidation Reaction

The electrochemical behaviour towards EOR on the electrocatalysts was examined in 0.50 M H_2SO_4 and 0.50 M KOH containing a volume of EtOH yielding 0.50 M EtOH, separately. Again, five CV cycles were performed at 50 mVs^{-1}, once stable, the last cycle was reported for the electrocatalytic activity towards EOR.

3.4.4 Linear Sweep Voltammetry (LSV)

The LSV experiment was conducted for EOR in 0.50 M H_2SO_4 or 0.50 M KOH containing a volume of EtOH yielding 0.50 M EtOH, separately. Subsequently, the LSVs were collected at 5 mVs^{-1}.

3.4.5 Chronoamperometry (CA)

The CA measurements were conducted at constant potentials for EOR in 0.50 M H_2SO_4 and 0.50 M KOH, respectively and the technique was conducted for 1000 s to evaluate the steady state activity of the electrocatalysts.

3.4.6 Electrochemical Impedance Spectroscopy

The EIS measurements were conducted to study the behaviour of the $Fe(CN)_6^{4-}/Fe(CN)_6^{3-}$ probe and EOR on the surface of the electrocatalysts in N_2 purged 0.10 M KCl containing 3.00 mM $K_3[Fe(CN)_6]/K_4[Fe(CN)_6]$, 0.5 M H_2SO_4 and 0.5 M KOH, separately. The measurements were conducted on a frequency ranging from 0.10 Hz to 100 kHz with an AC signal amplitude of 10 mA at the open circuit potential (OCV).

3.4.7 Rotating Disc Electrode (RDE) and Oxygen Reduction Reaction

The electrochemical behaviour of the electrocatalysts towards the ORR was investigated in O_2 saturated 0.5 M H_2SO_4 and 0.1 M KOH, separately. The electrolyte was purged with O_2 for 30 mins before collecting RDE measurements at the different rotation rates: 400, 625, 900, 1225, 1600, 2025 and 2500 rpm between 0.00 and 1.20 V vs. RHE.

3.4.8 EtOH Gas Sensing

The catalyst and catalyst ink were prepared using the method described in Section 3.4.1. For the catalyst ink, the drop and dry method was used to load 0.063 mg_{Pt} cm^{-2} of the catalyst.

A similar gas sensing set up and method as the one previously reported by Modjtahedi and co-workers [44] was used (shown in Figure 3.3).

The N_2 gas was used to facilitate the transportation of the analyte to the sensor chamber. Aliquots of absolute EtOH were pipetted into the stoppered-round bottom flask (RBF) containing 80 mL of ultra-pure water. Subsequently, the EtOH vapour was carried to the sensing chamber that was connected to the WE and CE. The gas sensing chamber comprised of an inlet and outlet, to allow the flow of the fresh analyte and removal of the used or products, respectively. The CA technique briefly described in Section 3.4.5 was used to conduct the study. A step potential of – 0.40 V ($E_{1/2}$ for the EOR in 0.50 M KOH) for 15 s per concentration.

The preliminary study investigated concentration values: 0.00 – 0.08 g dL^{-1} that are equivalent to 1.09 – 17.36 mM, respectively.

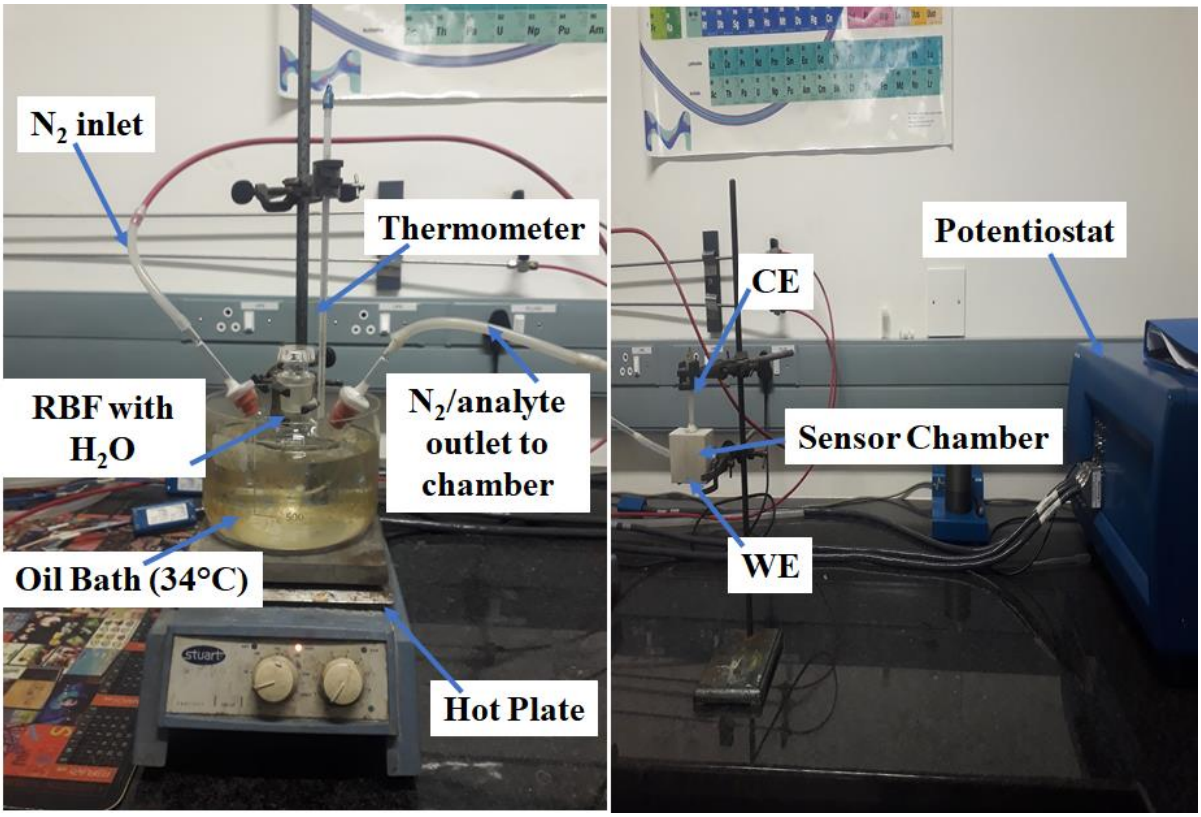


Figure 3.3: A picture of the experimental gas sensing set up.

Chapter 4

Physical and Electrochemical Characterization of the Supports and Electrocatalysts

4.1. Results and Discussion

In this Chapter, the physical characterization results from PXRD, Raman analysis, UV-vis., SEM and TEM of the support and electrocatalyst materials are discussed. Thereafter, the redox electrocatalysts are evaluated for their electron transport and mass transfer process.

4.1.1. Physical Characterization

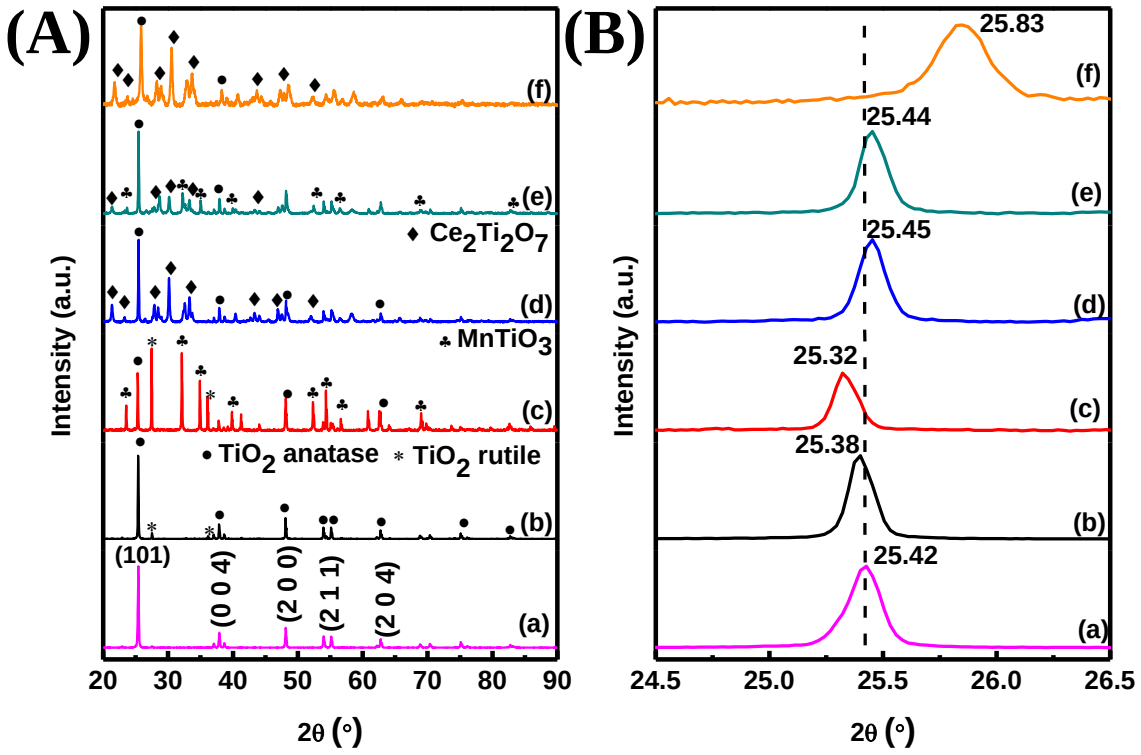


Figure 4.1: (A) PXRD patterns of the supports (a) TiO_2 anatase, (b) TiO_2, (c) TiO_2Mn, (d) TiO_2Ce, (e) $TiO_2Mn_{0.5}Ce_{0.5}$ and (f) TiO_2Ce/C and (B) the enlarged view of the (1 0 1) peak.

Figure 4.1 shows the XRD patterns obtained for TiO_2 anatase and the synthesized supports and electrocatalysts. The intense, narrow peaks indicate the high crystallinity of the TiO_2-based supports. In Figure 4.1A (a), the TiO_2 anatase exhibited peaks that are characteristic of the tetragonal phase in TiO_2 anatase (ICDD: 00-064-0863). The patterns of the TiO_2 and TiO_2Mn exhibit a rutile phase peak (ICDD: 00-021-1276) at $2\theta = 27.5$ °. This observation was expected since thermal treatment of TiO_2 at high temperatures (> 400 °C) results in phase transformation [110]. Also, Figure 4.1B(b) shows, the (1 0 1) peak shift to lower Bragg angle's, due to the transformation and the distortion of the crystal lattice upon the insertion of Mn cations in the TiO_2 lattice. Similar observations were reported by Pérez-Larios and co-workers [99], demonstrating a shift in (1 0 1) peak due to Mn cation insertion into the TiO_2 lattice. The presence of Ce/CeOx prohibited the phase transformation of the TiO_2 from anatase to rutile phase. Similar observations were previously reported [83,111] where the phase transformation hindrance was related to the formation of the Ce-O-Ti interface, in which the tetrahedral Ti atoms, substituted into the CeO_2 lattice interacts with octahedral Ti sites in TiO_2 anatase. This blocks the nucleation of TiO_2 anatase to rutile phase. Indeed, the XRD patterns of the TiO_2Ce and TiO_2Ce/C supports show new peaks that are attributed to cerium titanate ($Ce_2Ti_2O_7$), confirming the presence of the Ce-O-Ti interface. There is a slight broadening of the (1 0 1) peak in TiO_2Ce/C which is due to the overlapping amorphous carbon and (1 0 1) peak from carbon and TiO_2 anatase, respectively. Moreover, from Figure 4.1B, only a slight shift to a higher Bragg angle was observed for TiO_2Ce. This illustrates that the Ce cations do not substitute the Ti^{4+} in the TiO_2 lattice like it was postulated in the TiO_2Mn support. Since the ionic radii of Ce^{3+} (1.01 Å) is larger than Mn^{3+}/ Mn^{4+} (0.54 or 0.53Å), it is most likely that the Mn^{3+}/ Mn^{4+} ions would substitute the Ti^{4+} (0.61 Å), leading to a noticeable shift in (1 0 1) peak. The new peaks on the XRD patterns of the TiO_2Mn, TiO_2Ce and $TiO_2Mn_{0.5}Ce_{0.5}$ composite supports are attributed to pyrophanite ($MnTiO_3$) and $Ce_2Ti_2O_7$ [110,112].

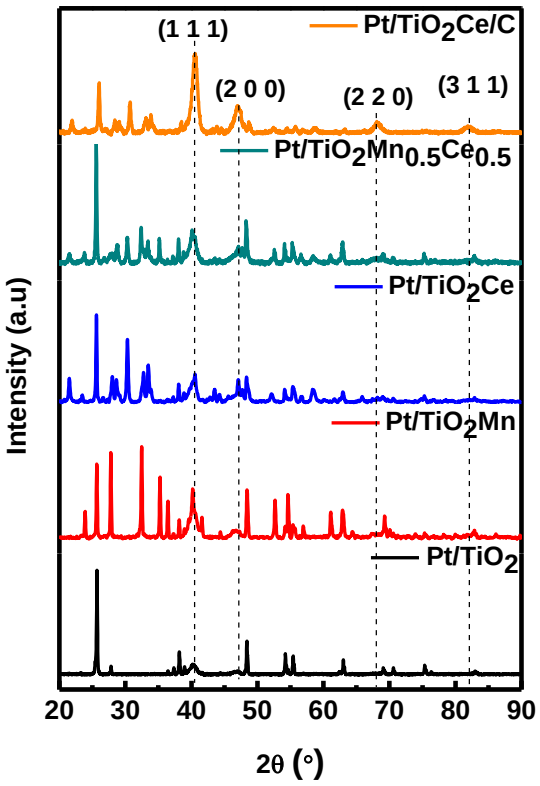


Figure 4.2: PXRD patterns of the electrocatalysts.

Table 4.1: Average crystallite size and lattice parameter by XRD for the electrocatalysts.

Electrocatalysts	***D* (nm)**	**a_0 (Å)**
Pt/TiO_2	7.6	3.88
Pt/TiO_2Mn	8.1	3.88
Pt/TiO_2Ce	8.7	3.87
$Pt/TiO_2Mn_{0.5}Ce_{0.5}$	7.9	3.88
$Pt/TiO_2Ce/C$	9.0	3.85

Figure 4.2 shows the XRD patterns of the electrocatalysts with the characteristics of face-centred cubic (fcc) structure of Pt. The reflections labelled (1 1 1), (2 0 0), (2 2 0) and (3 1 1) are attributed to the fcc Pt. The crystallite sizes of the Pt nanoparticles were calculated with the most structural sensitive miller index, Pt (1 1 1) using the Scherrer-Debye equation (Equation 3.1). The average crystallite sizes and lattice parameters are recorded in Table 4.1. The lattice

parameter of pure Pt is reported to be 3.92 [15], however, Table 4.1 shows lower values for all the investigated electrocatalysts. This result indicate the presence of a lattice compressive strain upon the Pt nanoparticles by the support.

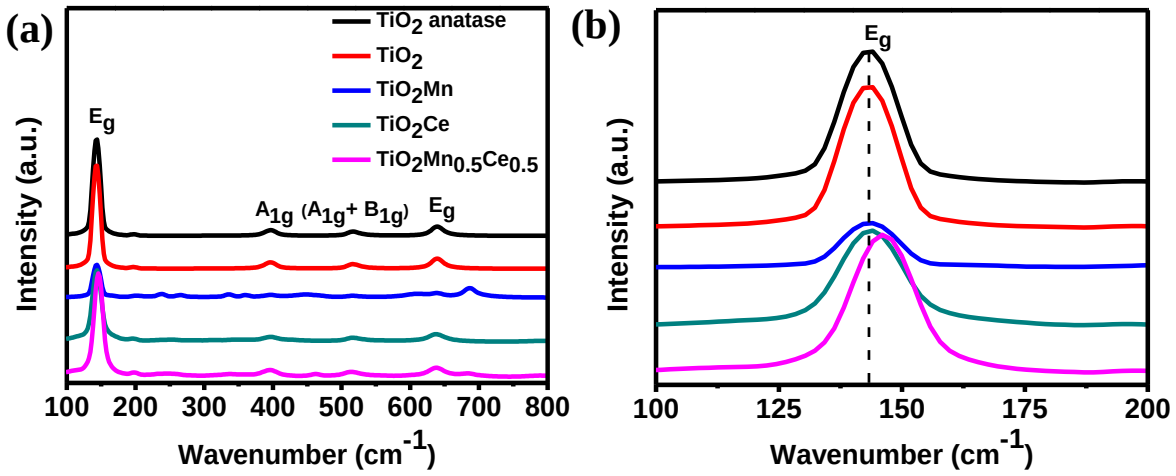


Figure 4.3: The Raman spectra of (a) the prepared supports and (b) an enlarged view of the Eg peak of the supports.

The phase structures of the hydrogenated, thermally treated support materials were further investigated by Raman spectroscopy shown in Figure 4.3. The Raman spectra of the support materials show peaks at 144 (E_g), 397 (A_{1g}), 516 (A_{1g}+B_{1g}) and 638 cm^{-1} (E_g) that correspond to the characteristic bond vibrations of the anatase phase TiO_2 [110]. The peak at 147cm^{-1} (E_g) was not identified due to the possible suppression by the high intense peak of E_g at 144 cm^{-1}. A similar observation was reported by Mehta and co-workers [43]. In Figure 4.3b, the E_g peak of $TiO_2Mn_{0.5}Ce_{0.5}$ displays a positive shift of the E_g peak towards higher wave numbers, whilst the other patterns displayed broader E_g peaks with reduced intensity. Pérez-Larios and co-workers [99] reported this kind of shifts being due to the changes that occur in the local structure around the metal ions (Ti^{4+}) as a result of Raman active modes being sensitive to any disruption that occurs on the oxygen (O) to metal (Ti) coordination. This observation suggests that Mn^{2+}, Mn^{3+} and Mn^{4+} ions substitute Ti^{4+}, disrupting the TiO_2 lattice [99,112,113].

Furthermore, the TiO_2Mn spectrum shows a strong Raman active mode at 685.7 cm^{-1} that is ascribed to the vibrational mode of MnO_6 octahedra [112]. Raman active modes at 199.5, 240.5, 264.4, 336.2, 360.1, 445.5, 610.5 and 685.7 cm^{-1} were also observed. Similar active modes were reported by Guowei et al. [112] and Maurya et al. [114], separately. The authors associated the peaks to the presence or formation of pyrophanite $MnTiO_3$ confirming the Ti-O- Mn bond formation.

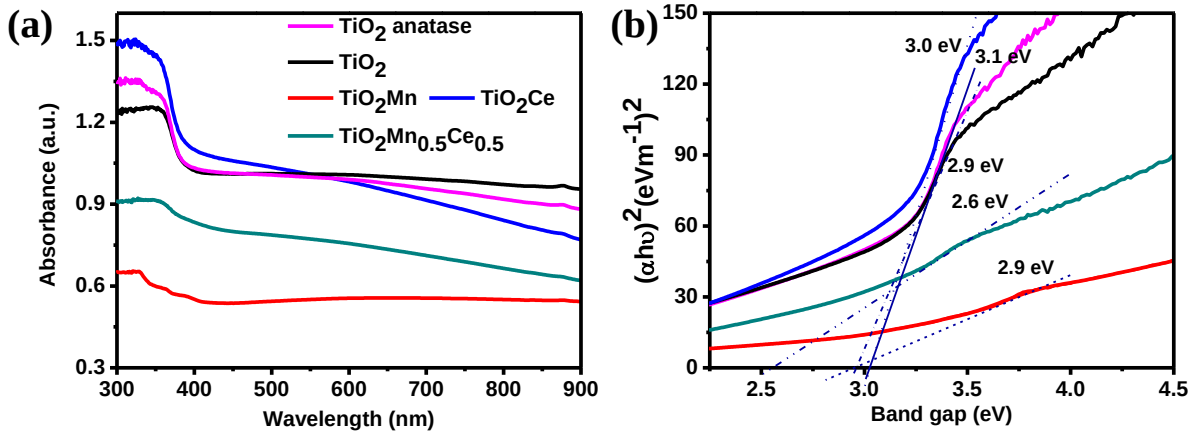


Figure 4.4: (a) UV-visible spectra and (b) Tauc plot for TiO_2 anatase, TiO_2, TiO_2Mn, TiO_2Ce and TiO_2 $Mn_{0.5}Ce_{0.5}$.

The optical properties of the support materials were examined with the use of UV-Visible spectroscopy and their absorption spectra are shown in Figure 4.4a. TiO_2 anatase shows an absorption at wavelengths shorter than 400 nm, which is attributed to the excitation of electrons from the valence band into the conduction band of TiO_2 anatase [114,115]. There was no significant shift observed for the annealed TiO_2. However, the TiO_2Ce and $TiO_2Mn_{0.5}Ce_{0.5}$ show slight shifts of absorption towards higher wavelengths (red shift) in the range of 400 – 530 and 350 – 530 nm, respectively. The red shifts in the absorption spectra when compared to the TiO_2 anatase indicates the reduction in the band gap of the TiO_2 anatase upon the introduction of Mn and Ce cations into the TiO_2 crystal lattice and the heat treatment [109,115,116]. Furthermore, the UV spectra of the TiO_2Mn shows a wide absorption band in

the wavelength range of 340 – 750 nm. The absorption bands range are 340 – 450, 450 – 750 nm and are attributed to Mn^{2+} to Ti^{4+} charge transfer and $^6A_{1g}$ to $^4A_{1g}$ to $^6A_{1g}$ to $^4T_{2g}$ crystal field transition of octahedral Mn^{2+}site in the $MnTiO_3$ [111,117]. Tauc plots are represented in Figure 4.4b, where the band gap energies were estimated by extrapolating the linear region to $y = (\alpha h\nu)^2 = 0$. The estimated band gaps for the TiO_2 anatase and the prepared supports are presented in Table 4.2. As seen from the results, TiO_2 anatase exhibited a slightly lower band gap than the literature value (3.2 eV) [89]. On the other hand, the prepared supports exhibited reduced band gaps after subjection of the powdered samples to high temperature (850 ºC) under H_2/N_2 flow, in the presence of Mn and Ce cations. A significant shift on the band gap was noticeable for $TiO_2Mn_{0.5}Ce_{0.5}$ (0.5 eV). Similar observations in bandgap shifts have been reported by other authors due to doping of TiO_2 [116,118,119] and exposure to reducing environment [43], indicating changes in the optical properties of materials. The reduced band gaps associated to enhanced conductivity of the materials [81]. The $TiO_2Mn_{0.5}Ce_{0.5}$ may exhibit improved conductivity due to the narrow bandgap compared to the other electrocatalyst supports that revealed only slight shifts.

Table 4.2: Band gap and shifts.

Supports	**Bandgap (eV)**	**Bandgap Shift (eV)**
TiO_2 anatase	3.1	-
TiO_2	2.9	0.2
TiO_2Mn	2.9	0.2
TiO_2Ce	3.0	0.1
$TiO_2Mn_{0.5}Ce_{0.5}$	2.6	0.5

XPS was conducted to probe the surface composition, valence states and chemical bonding of the electrocatalysts. The binding energies and atomic percentages (at. %) are reported in Table 4.3. Figure 4.5 – 4.7 shows the high resolution XPS spectra of Ti 2p, O 1s, Mn 2p, Ce 3d and Pt 4f for TiO_2 anatase and the respective electrocatalysts.

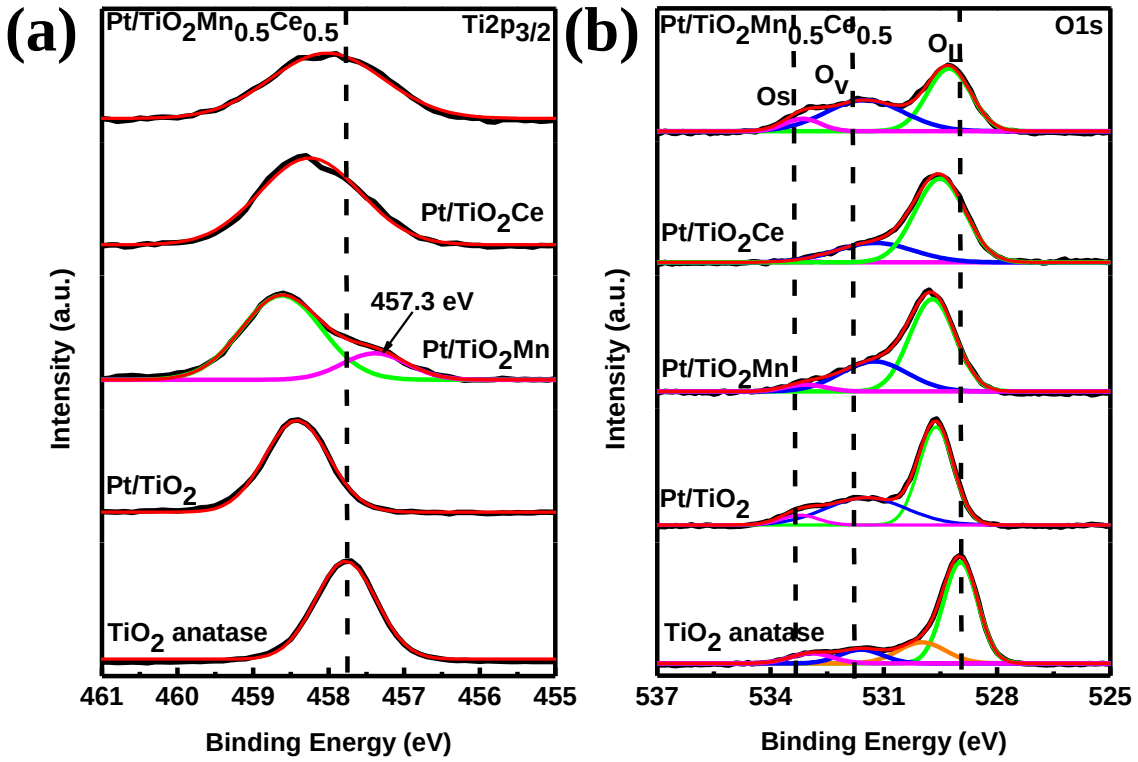


Figure 4.5: XPS spectra of (a) Ti2p and (b) O1s for TiO_2 anatase and the electrocatalysts.

In Figure 4.5a, the $Ti2p_{3/2}$ core level spectra, associated to Ti^{4+} in TiO_2 anatase and the electrocatalysts are shown. It is observed that the binding energy of the electrocatalysts show a positive shift compared to TiO_2 anatase, indicative of a change in the local environment of Ti^{4+} in the TiO_2 lattice upon hydrogen treatment at 850 °C and the presence of Mn and Ce cations [80]. Also, Lu and co-workers [120] attributed this kind of positive shift to the electron transfer from TiO_2 to Pt and the same interaction is possible for the materials reported in this work. The deconvolution of $Ti2p_{3/2}$ peak of the Pt/TiO_2Mn shows a new peak at binding energy 457.4 eV that is due to the Ti^{4+} state in the $MnTiO_3$ which supports the XRD and Raman

analysis, demonstrating the presence of $MnTiO_3$ [117]. Figure 4.5b shows the O1s spectra which after deconvolution, three peaks are presented at *ca*. 529.6, 531.4 and 532.8 eV assigned to the lattice oxygen (O_L), oxygen vacancies (O_V) and surface adsorbed hydroxyl groups (O_S), respectively [121]. The O_L peaks show a positive shift relative to the TiO_2 anatase, indicative of a change in the TiO_2 lattice oxygen. The at. % ratio of O_V and the total oxygen content are 0.11, 0.20, 0.19, 0.15 and 0.26 for TiO_2 anatase, Pt/TiO_2, Pt/TiO_2Mn, Pt/TiO_2Ce and $Pt/TiO_2Mn_{0.5}Ce_{0.5}$, respectively. This result indicates a higher content of O_V in the $Pt/TiO_2Mn_{0.5}Ce_{0.5}$, Pt/TiO_2 and Pt/TiO_2Mn unlike Pt/TiO_2Ce. In a study conducted by Guo and co-workers [98], the authors found that O_V rich support material (CeO_2 nanorods) improved the dispersion of small sized PdCu nanoparticles, unlike CeO_2 nanorods with low O_V content. A similar observation was noticed in this work, where O_V rich electrocatalyts (Pt/TiO_2, Pt/TiO_2Mn and $Pt/TiO_2Mn_{0.5}Ce_{0.5}$) revealed small average particle (Pt) sizes relative to Pt/TiO_2Ce. Several studies have demonstrated enhanced catalytic behaviour in electrochemical reactions such as, alcohol oxidation and oxygen reduction reactions by O_V rich electrocatalysts [89,98,121]. Thus, from the XPS results, the $Pt/TiO_2Mn_{0.5}Ce_{0.5}$ may exhibit improved electrocatalytic behaviour, due to the abundant O_V present in the sample.

Table 4.3: The binding energies and elemental at. % of the TiO_2 anatase and electrocatalysts from XPS analysis.

Species	TiO_2 Anatase	Pt/TiO_2	Pt/TiO_2Mn	Pt/TiO_2Ce	$Pt/TiO_2Mn_{0.5}Ce_{0.5}$
Ti $2p_{3/2}$	457.7	458.4	458.6	458.2	458.1
	28.5 %	22.6 %	19.8 %	20.4 %	15.7 %
O1s: O_L	528.9	529.6	529.8	529.6	529.3
	57.2 %	47.6 %	47.2 %	51.6 %	41.0 %
O1s: O_V	531.5	531.6	531.4	531.4	531.6
	8.1 %	14.2 %	12.5 %	9.5 %	17.3 %
O1s: O_S	533.0	533.2	533.1	533.0	533.0
	6.3 %	9.9 %	5.0 %	3.2 %	12.0%
Pt $4f_{7/2}$		70.1	70.5	70.3	70.3
		5.7 %	9.3 %	8.5 %	7.3 %
Mn $2p_{3/2}$	-	-	640.8	-	640.8
			6.3 %	-	1.5%
Ce $3d_{5/2}$: Ce^{4+}	-	-	-	881.0	881.9
	-	-	-	2.9 %	1.7 %
Ce $3d_{5/2}$: Ce^{3+}	-	-	-	885.0	885.2
	-	-	-	3.9 %	1.8 %

The $Mn2p_{3/2}$ spectra at *ca*. 640.8 eV for the Pt/TiO_2Mn and $Pt/TiO_2Mn_{0.5}Ce_{0.5}$ are shown in Figure 4.6a. After deconvolution three peaks were presented at 639.8, 640.9 and 642.3 eV attributed to Mn^{2+}, Mn^{3+} and Mn^{4+}, respectively, demonstrating the presence of the different states of manganese. The additional peak at 641.1 eV was assigned to Mn^{2+} satellite band

[99,112,116]. Figure 4.6b, displays the Ce3d spectra of the Pt/TiO_2Ce and Pt/$TiO_2Mn_{0.5}Ce_{0.5}$. Two regions of the Ce3d, attributed to Ce $3d_{5/2}$ and Ce $3d_{3/2}$ are shown. After deconvolution of Ce $3d_{5/2}$ region, two peaks presented at binding energies of *ca*. 881.5 and 885.1 eV are shown and ascribed to Ce^{4+} and Ce^{3+}, respectively. The Ce^{3+}, is associated to O_V in the CeO_X lattice [98]. The determined at. % ratio of Ce^{3+} in the Ce content for Pt/TiO_2Ce and Pt/$TiO_2Mn_{0.5}Ce_{0.5}$ was 0.57 and 0.50, respectively. This result indicates a higher Ce^{3+} (O_V) content in Pt/TiO_2Ce compared to Pt/$TiO_2Mn_{0.5}Ce_{0.5}$.

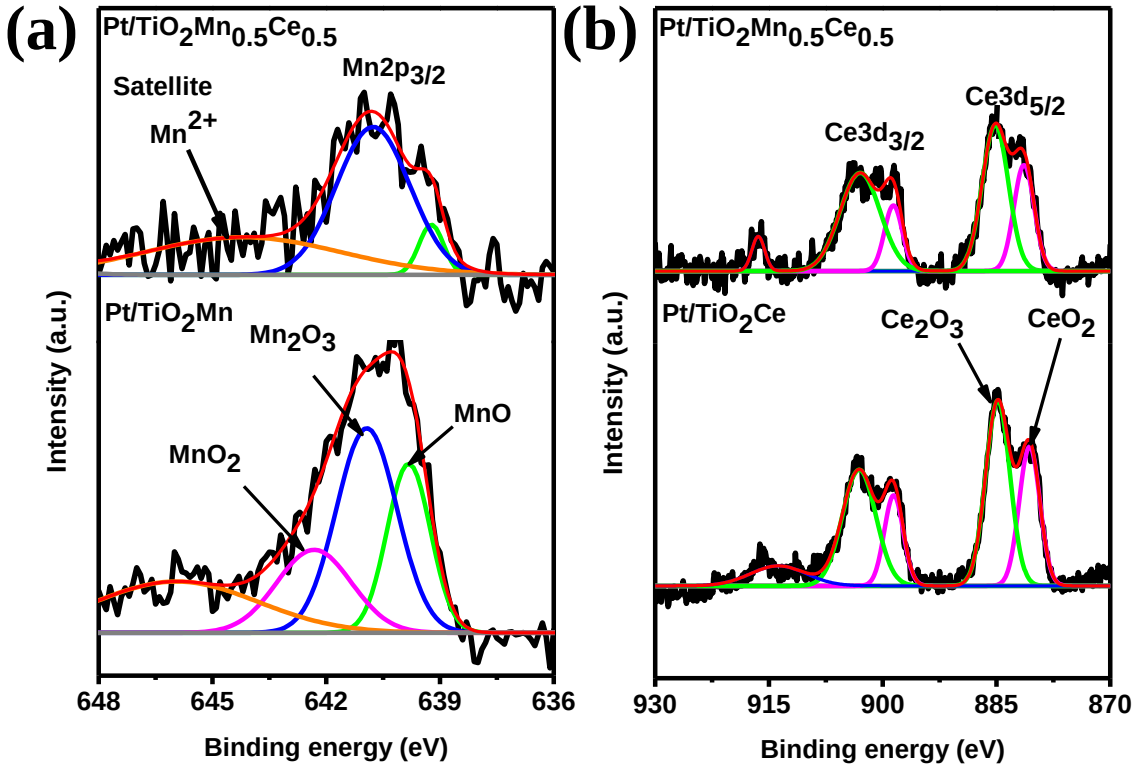


Figure 4.6: XPS spectra of (a) Mn2p and (b) Ce3d of the electrocatalysts.

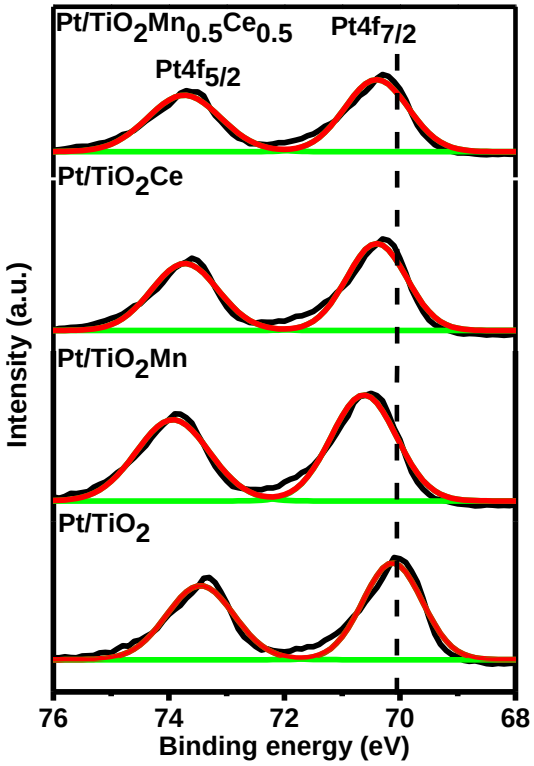


Figure 4.7: XPS spectra of Pt4f for the electrocatalysts.

Figure 4.7 displays the Pt 4f XPS spectra, with a doublet that is attributed to the $Pt4f_{7/2}$ and $Pt4f_{5/2}$. The $Pt4f_{7/2}$ binding energies for the Pt/TiO_2, Pt/TiO_2Mn, Pt/TiO_2Ce and $Pt/TiO_2Mn_{0.5}Ce_{0.5}$ show a negative shift by 0.9, 0.5, 0.7 and 0.7 eV, respectively, relative to Pt/C that has a binding energy of 71.0 eV [81,67]. This is associated to the loss of electron from the TiO_2 based supports to Pt, indicating a strong metal to support interaction when compared to Pt/C [67]. The strong interaction is known to enhance catalytic activity, by the electronic effect. Thus, it is expected that Pt/TiO_2 and Pt/TiO_2Ce and $Pt/TiO_2Mn_{0.5}Ce_{0.5}$ will reveal less poisoning in this work, as a result to the weak adsorption of reaction intermediates species on the Pt surface (better tolerance to CO_{ads}-like species). Furthermore, the SMSI is expected improve the stability of the electrocatalysts, preventing dissolution and agglomeration of the Pt nanoparticles [51]. The at. % of Pt on the electrocatalysts are given in Table 4.3 and the Pt:Ti ratios are 0.25, 0.47, 0.42 and 0.41 for Pt/TiO_2, Pt/TiO_2Mn, Pt/TiO_2Ce and

$Pt/TiO_2Mn_{0.5}Ce_{0.5}$, respectively. As seen from the results, Pt/TiO_2 exhibited the lowest Pt content, which suggests that the loading was improved in composite supports TiO_2/MO_X.

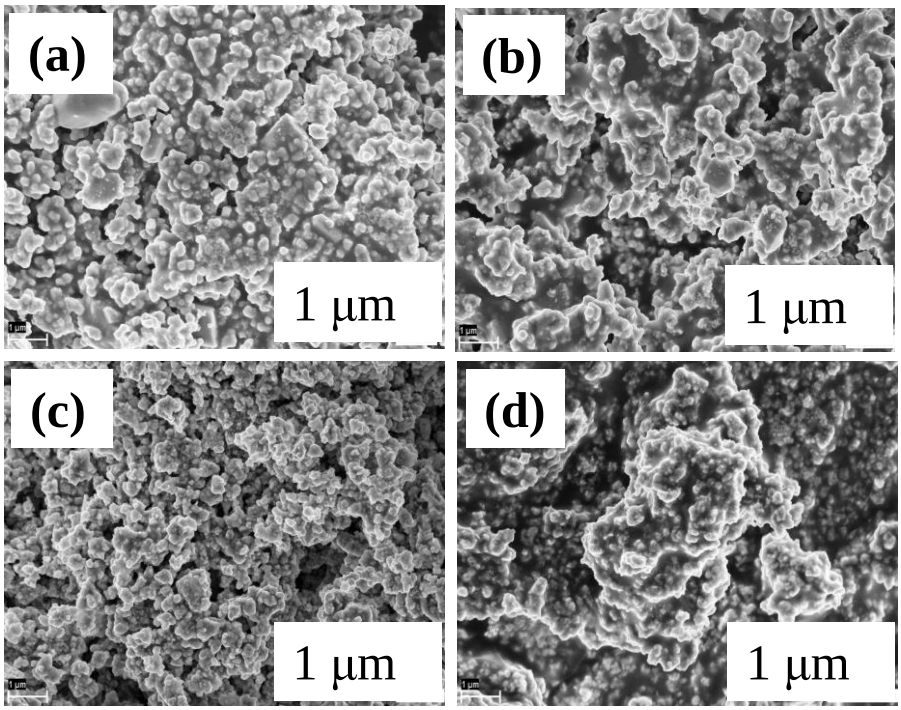


Figure 4.8: (a–d) SEM images Pt/TiO_2, Pt/TiO_2Mn, Pt/TiO_2Ce and $Pt/TiO_2\ Mn_{0.5}Ce_{0.5}$, respectively.

The surface morphology and elemental analysis of the electrocatalysts were examined by SEM and EDX, respectively. Figure 4.8 a-d displays the SEM images of the electrocatalysts. The prepared materials show agglomerated grains as well as, small particles that are spherical-like on the support. The large agglomerates are the metal oxides composites (TiO_2/MO_X) and the small spherical-like particles are the supported metal particles. The corresponding EDS spectra of the electrocatalysts are presented in Figure 4.9 a-d. The spectra show the peaks that are associated with Pt, Ti, O, Mn and Ce in the electrocatalysts. This observation confirms the presence of the elements in the respective materials.

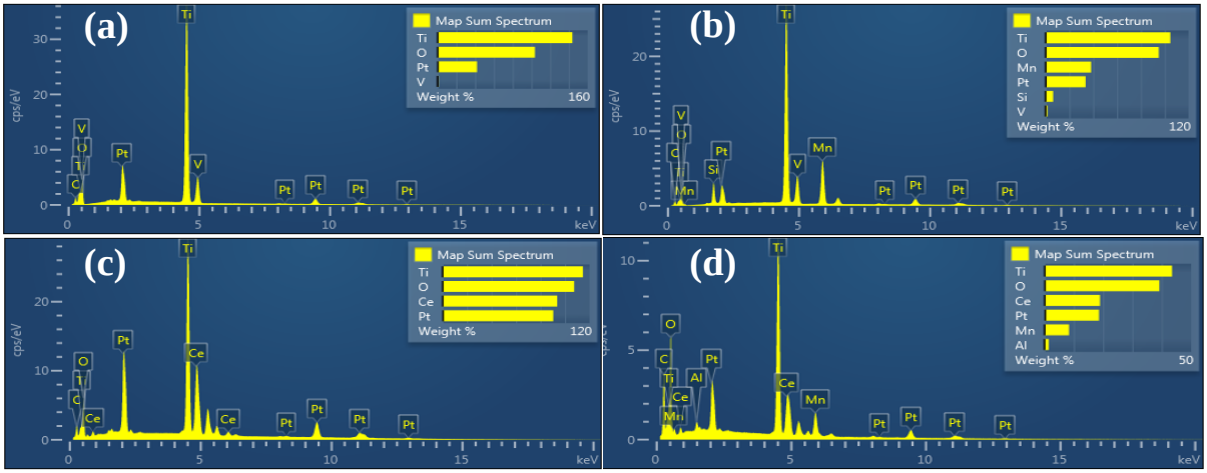


Figure 4.9: EDX spectra (a-d) of Pt/TiO_2, Pt/TiO_2Mn, Pt/TiO_2Ce and $Pt/TiO_2\ Mn_{0.5}Ce_{0.5}$, respectively.

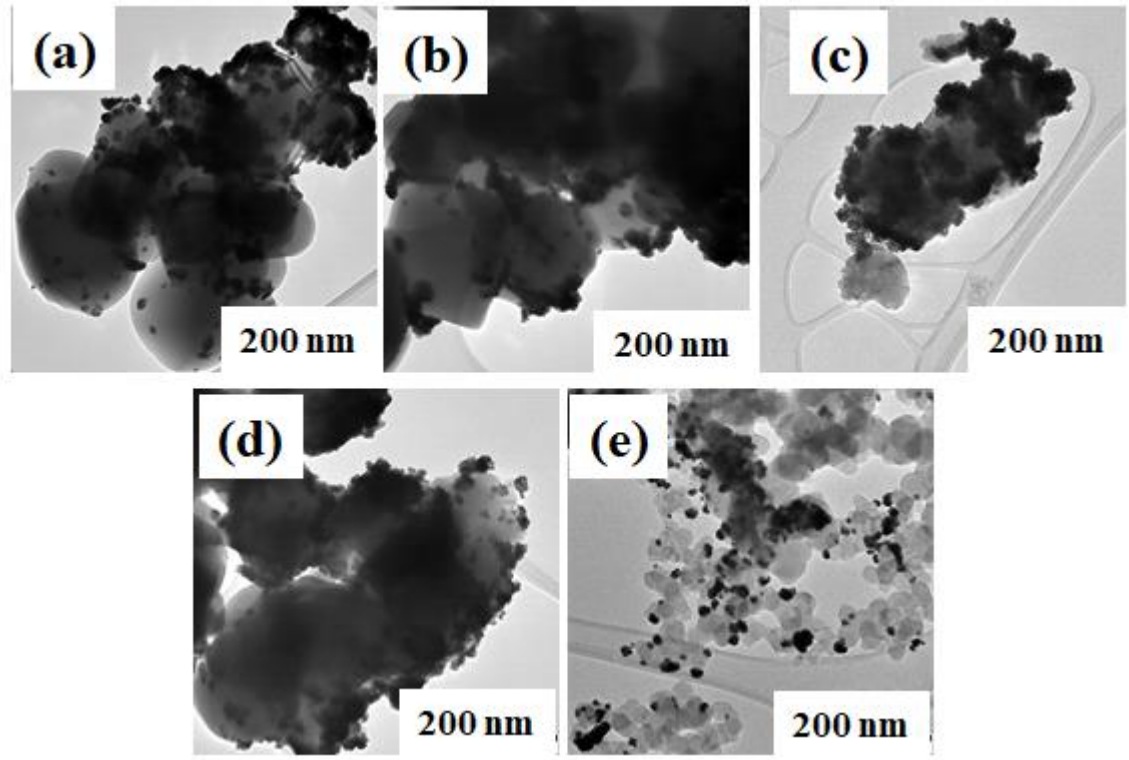


Figure 4.10: The TEM images of the electrocatalysts (a) Pt/TiO_2, (b) Pt/TiO_2Mn, (c) Pt/TiO_2Ce and (d) $Pt/TiO_2Mn_{0.5}Ce_{0.5}$, (e) $Pt/TiO_2Ce/C$.

The morphologies of the electrocatalysts were also investigated by TEM. Figure 4.10 shows the TEM images of the electrocatalysts. The metal particles are distributed on the TiO_2-based and TiO_2/Ce/C supports. The supported particles display semi-spherical morphologies that

appear agglomerated, demonstrating a non-uniform distribution on the supports. In Figure 4.10e, the carbon in the $Pt/TiO_2/Ce/C$ is observed. It is noticed that the carbon/MO_X composite was not a homogenous mixture since some parts of the carbon were not occupied by the MO_X.

4.1.2 Electrochemical characterization

Electrochemical behaviour of the electrocatalysts in 0.1 M KCl containing 3.0 mM $K_4[Fe(CN)_6]/K_3[Fe(CN)_6]$.

In this subsection, the electron transport and mass transfer process on the electrocatalysts were investigated. The experiments were conducted in a 0.1 M KCl containing 3.0 mM potassium ferro-/ferri-cyanide ($K_4[Fe(CN)_6]/K_3[Fe(CN)_6]$) redox probe.

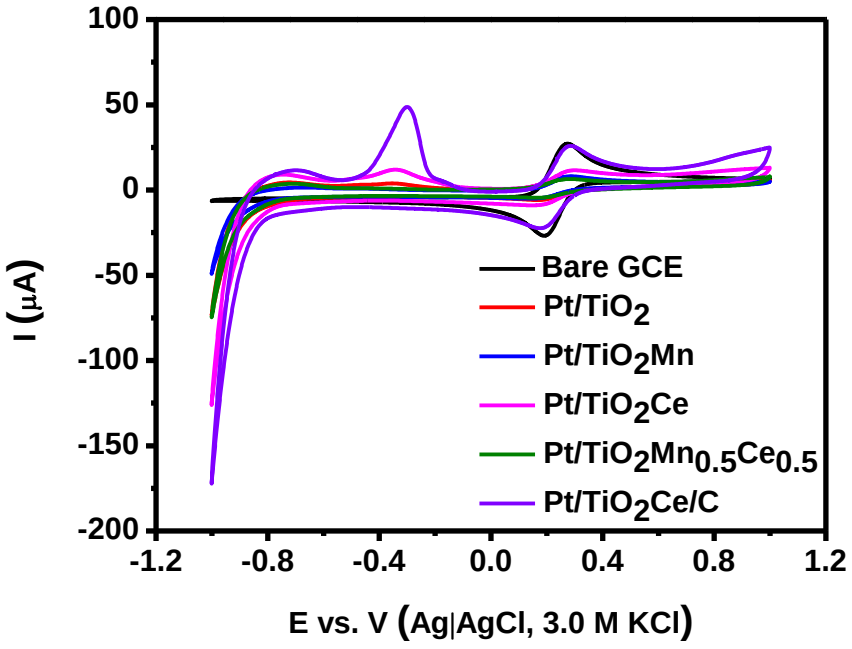


Figure 4.11: Cyclic Voltammograms of the bare GCE and modified GCE in 0.1 M KCl containing 3.0 mM $K_3[Fe(CN)_6]/K_4[Fe(CN)_6]$ at 10 mVs^{-1}.

The CVs of the GCE and modified GCE with Pt/TiO_2, Pt/TiO_2Mn, Pt/TiO_2Ce, Pt/$TiO_2Mn_{0.5}Ce_{0.5}$ and Pt/TiO_2C/C are shown in Figure 4.11. From the CV profiles, the $K_3[Fe(CN)_6]$/ $K_4[Fe(CN)_6]$ redox couple and H_{ads}/H_{des} peaks appear at 0.0 to 0.5 and - 1.0 to - 0.10 V, respectively. The H_{ads}/H_{des} peaks represent a monolayer coverage of hydrogen on the Pt surfaces which was discussed in Section 2.4.1 [9]. In addition, the electrocatalysts Pt/TiO_2, Pt/TiO_2Mn, Pt/TiO_2Ce and Pt/$TiO_2Mn_{0.5}Ce_{0.5}$ show a suppressed current response compared to the bare GCE and Pt/TiO_2Ce/C. This indicates the greater resistance to e^- transfer on the materials when compared to the Pt/TiO_2Ce/C. As expected, carbon enhanced the e^- transfer of the material Pt/TiO_2Ce due to the improved conductivity that is induced by carbon. To support this, the Δ*E*p values were calculated using Equation 4.1 and are reported in Table 4.4.

$$\Delta Ep = E_{Anode} - E_{Cathode} = \frac{56.5\ mV}{n} \qquad 4.1$$

Where, E_{Anode} is the anodic scan peak potential, $E_{Cathode}$ is the cathodic scan peak potential and *n* is the number of electrons in the electrochemical equation. The ferri-ferrocyanide electrochemical process involves $1e^-$ process. As seen from Table 4.4, the Δ*E*p increase in the order: bare GCE, Pt/TiO_2Ce/C, Pt/TiO_2, Pt$TiO_2Mn_{0.5}Ce_{0.5}$, Pt/TiO_2Mn and Pt/TiO_2Ce, respectively. The Δ*E*p indicates faster e^- transfer kinetics on the Pt/TiO_2Ce/C relative to the other electrocatalysts. The enhanced e^- transfer on Pt/TiO_2Ce/C is attributed to the increased conductivity upon coupling Pt/TiO_2Ce with carbon. The high Δ*E*p values for Pt/TiO_2, Pt$TiO_2Mn_{0.5}Ce_{0.5}$, Pt/TiO_2Mn and Pt/TiO_2Ce indicates the resistive nature of the hybrid supports TiO_2/MOx [122,123].

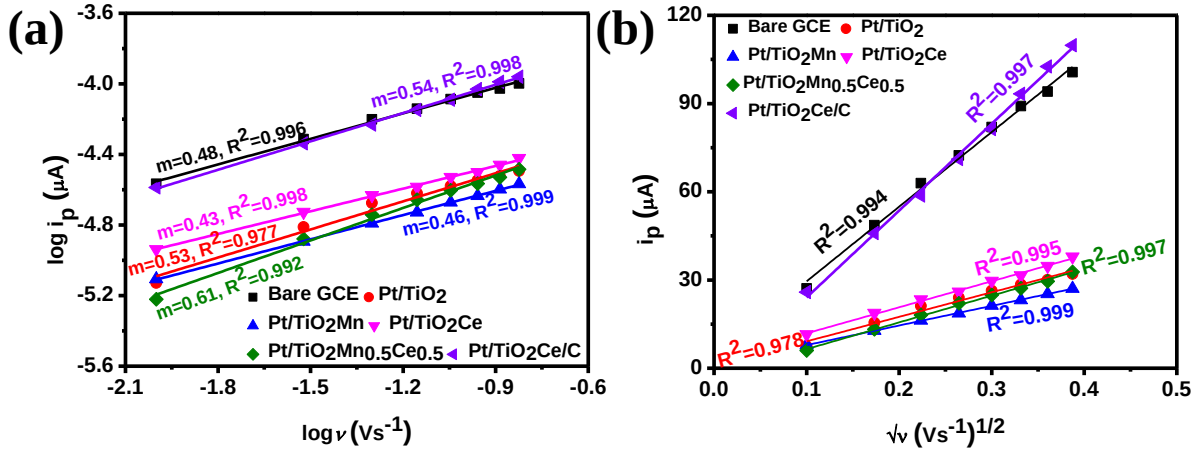


Figure 4.12: The (a) log i_p vs. log ν and (b) i_p vs. √ν plots for bare GCE and Pt/TiO_2, Pt/TiO_2Mn, Pt/TiO_2Ce, Pt/TiO_2Mn$_{0.5}$Ce$_{0.5}$ and Pt/TiO_2Ce/C.

The effect on anodic peak current (i_p) with increasing scan rate (v) (0.01–0.15 V/s) was investigated on all electrocatalysts to determine whether the obtained current response was attributed to diffusion or capacitive behaviour on the electrocatalyst. Previously, this behaviour has been studied by the use of the Equation 4.2 [124,125]:

$$i = av^b \tag{4.2}$$

Where a and b are adjustable parameters, of which b is obtainable from the logarithmic plot of i_p vs. ν. The b value is a representative of the faradaic and non-faradaic current that is attributed to the diffusional (0.5) and capacitive (1.0) behaviour of the electrocatalysts, respectively. Therefore, when b = 0.5, i is directly proportional to √ν. When b = 1, the relationship between i and ν is defined by Equation 4.3 shown below [124]:

$$i = C_{dl}Av \tag{4.3}$$

Where C_{dl} is the double layer capacitance, A is the active area of the electrode and i and v were previously defined above. As seen in Figure 4.11a, the slope from the logarithmic plot of i vs. v range from 0.43 to 0.61, with Pt/TiO_2, Pt/TiO_2Mn, Pt/TiO_2Ce and Pt/TiO_2Ce/C showing b ~

0.5, indicative of a diffusion controlled process. The Pt/$TiO_2Mn_{0.5}Ce_{0.5}$ presents b = 0.61, indicative of a mixed diffusion-adsorptive behaviour of the electrocatalyst [123,126]. Figure 4.11b shows the i_p vs. √ν and all electrocatalysts showed a linear relationship. However, Pt/$TiO_2Mn_{0.5}Ce_{0.5}$ and Pt/TiO_2Ce/C demonstrated negative (-ve) y-intercepts, indicative of a slight deviation from a purely diffusion-controlled behaviour. The active electrode surface area of the electrocatalysts were determined from the Randles-Ševčik equation shown in Equation 4.4 [127] and reported in Table 4.4.

$$i_p = (2.69 \times 10^5) A C D^{0.5} v^{0.5} n^{1.5} \quad 4.4$$

Where A is the active electrode surface area (cm^2), C is the bulk concentration of the species (mol cm^{-3}), D is the diffusion coefficient of the species (cm^2 s^{-1}) and the other variables were previously defined. The A values support the observed i_p values whereby Pt/$TiO_2Mn_{0.5}Ce_{0.5}$ and Pt/TiO_2Ce/C, exhibited a high active area relative to the other electrocatalysts. This suggests that the high current response observed on Pt/$TiO_2Mn_{0.5}Ce_{0.5}$ and Pt/TiO_2Ce/C is attributed to both the high exposure of active sites and the mixed adsorptive-diffusion controlled process behaviour of the electrocatalysts. Furthermore, the surface coverage (Γ) values were calculated using the Brown-Anson theory, Equation 4.5 [124] and reported in Table 4.4.

$$i_p = \frac{n^2 F^2}{4RT} v A \Gamma \quad 4.5$$

Where F is the Faraday's constant (96485.33 C mol^{-1}), R is the gas constant (8.314 J $mol^{-1}K^{-1}$), T is the temperature (298.15 K) where other variables were previously defined above. Again, Pt/$TiO_2Mn_{0.5}Ce_{0.5}$ and Pt/TiO_2Ce/C displayed high Γ, indicating high surface coverage on the electrode and the diffusion-adsorptive behaviour of the electrocatalyst.

Table 4.4: Summary of data obtained from CV of the bare GCE and electrocatalysts in 0.1 M KCl containing 3.0 mM $K_3[Fe(CN)_6]/K_4[Fe(CN)_6]$.

Electrocatalysts	**ΔE (V)**	**$A \times 10^{-3}$ (cm^{-2})**	**Γ (nmol cm^{-2})**
Bare GCE	0.0831	11.4	7.44
Pt/TiO_2	0.108	3.75	2.42
Pt/TiO_2Mn	0.147	3.00	1.98
Pt/TiO_2Ce	0.152	3.98	2.63
$Pt/TiO_2Mn_{0.5}Ce_{0.5}$	0.130	4.10	2.68
Pt/TiO_2Ce-C	0.0927	13.3	8.83

To further examine the electrochemical behaviour of the electrocatalysts, EIS was conducted at OCV of 0.30 V in the frequency range of (0.1 Hz – 100 kHz). Figure 4.13a presents the Nyquist plots of the GCE and modified GCE. The plots were fitted with the EEC shown in Figure 4.13b and c, and the fitted data was reported in Table 4.5 with their relative deviations from the real fit. The models consist of the R_s, R_{ct}, C_{dl}, *CPE* and *W* [128]. As seen from the Nyquist plot, the bare GCE exhibits a lower R_{ct}, illustrated by the small diameter of the semicircle [128,129]. After modifying the GCE with the electrocatalysts, the diameters increased, indicative of the increased R_{ct} on the electrode surface. This result supports the calculated ΔE_p from the CVs. In particular, the Pt/TiO_2Ce exhibited the highest charge transfer resistance whereas the addition of carbon lowered the R_{ct}. It is possible that the Pt/TiO_2Ce consists of a passive layer which resulted in a higher R_{ct} indicating a slower charge transfer rate as seen from the ΔE_p. Also, it is noticeable that CeO_X increases the pseudocapacitive behaviour of the electrocatalysts, exhibiting high *CPE* values relative to the other electrocatalysts. Moreover, the addition of carbon, increases the porosity of the material that results in surface roughness and induces the pseudocapacitive behaviour, yielding high *CPE* values [130].

The *CPE* impedance (W_{CPE}) is defined in Equation 4.6 [126]:

$$W_{\mathrm{CPE}} = [Q(j\omega)^{a}]^{-1} \qquad 4.6$$

Where Q is the frequency-independent constant, ω is the radial frequency, a is obtainable from the slope of the log Z vs. log frequency. When a = -1, 0, 0.5 and 1 the CPE behaves as an inductor, a pure resistor, Warburg impedance and a pure capacitor respectively. As seen from Table 4.5, a ranges from 0.74 – 0.81, demonstrating a mixture of Warburg impedance and capacitor behaviour on all the electrocatalysts.

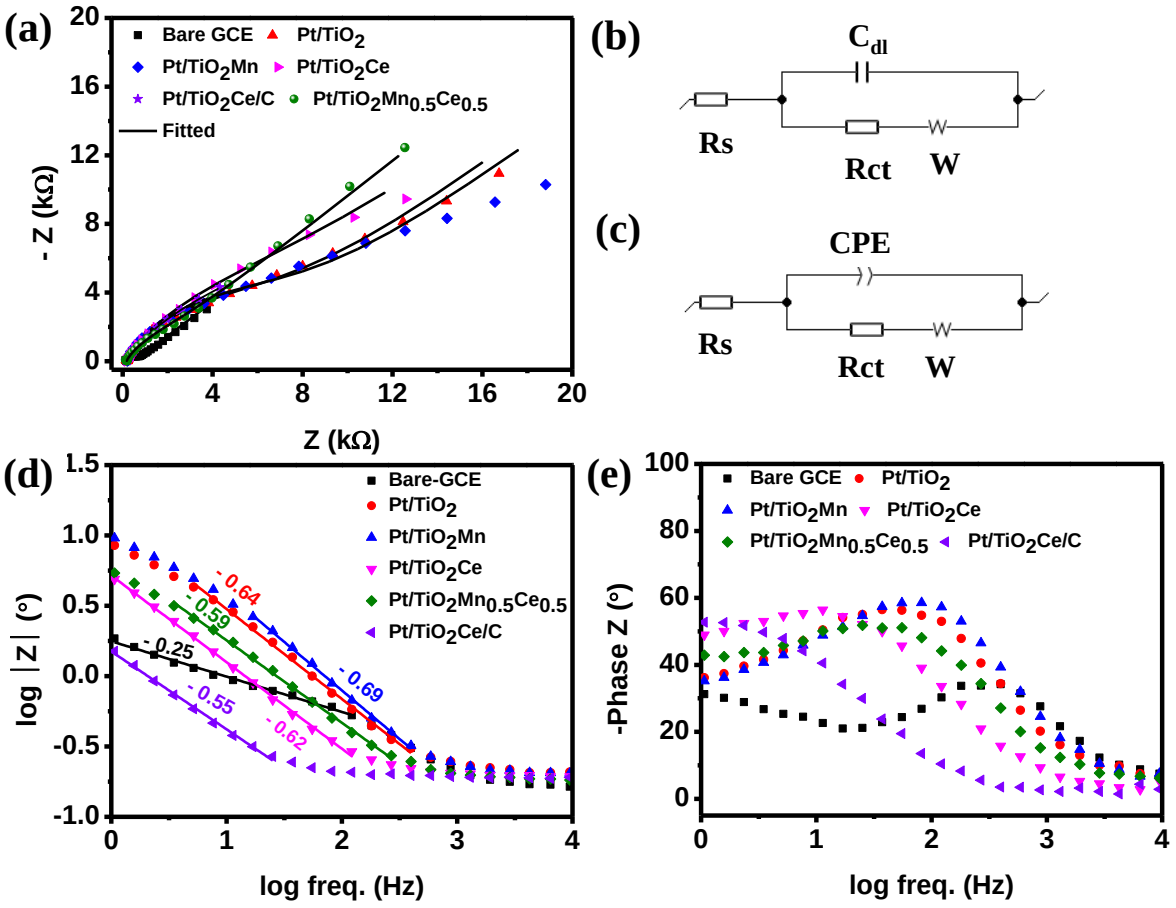


Figure 4.13: The (a) Nyquist plots, (b,c) EEC and Bode plots, (d) log Z vs. log frequency and (e) phase Z vs. log frequency for the GCE and modified GCE in 0.10 M KCl containing 3.0 mM $K_3[Fe(CN)_6]/K_4[Fe(CN)_6]$.

Figure 4.13d and e displays the Bode impedance plots of the electrocatalysts. The log Z vs. log frequency slope values are shown in Figure 4.13d and phase angles (θ) are reported in Table

4.5. When θ is -90 and -45 ° the electrocatalysts demonstrate an adsorption-limited and diffusion-limited process, respectively [126]. All the modified GCE exhibit a mixed adsorption and diffusive behaviour with θ values > - 45 ° (more of the diffusive limited process). Also, the electrocatalysts show a pseudocapacitive behaviour, illustrated by the slope values that are > - 0.50 [127,131].

Table 4.5: EIS data and Bode impedance data for the bare GCE and modified GCE. The values in the parenthesis are the deviations from the real fit.

Electrocatalysts	R_s **(Ω)**	R_{ct} **(Ω)**	C_{dl} **(μF)**	*CPE* **(μF)**	***a***	θ **(°)**
Bare GCE	146.4 (0.291)	388.7 (0.464)	2.77 (0.154)	-	-	-34.3
Pt/TiO_2	187.3 (0.289)	7620 (5615)	-	10.55 (0.0198)	0.79 (0.501)	-56.8
Pt/TiO_2Mn	186.5 (0.287)	8087 (4.49)	-	7.87 (0.0131)	0.81 (0.501)	-59.4
Pt/TiO_2Ce	182.4 (0.271)	10455 (27.55)	-	36.1 (0.0415)	0.76 (0.501)	-57.1
$Pt/TiO_2Mn_{0.5}Ce_{0.5}$	166.6 (0.303)	3570 (25.71)	-	18.4 (0.135)	0.77 (0.502)	-51.8
$Pt/TiO_2Ce/C$	180.6 (0.260)	9888 (202.2)	-	161.8 (0.637)	0.74 (0.500)	-52.8

4.2. Conclusion

TiO_2 based supports (TiO_2, TiO_2Mn, TiO_2Ce and $TiO_2Mn_{0.5}Ce_{0.5}$) were synthesized under reducing atmosphere at 850 °C. From the physicochemical characterizations, it is deduced that titanium sub-oxides (Ti_XO_{2x-1}) did not form in the presence of Mn and Ce at the reported experimental conditions and slight band gap narrowing was observed for the prepared material, where $Pt/TiO_2Mn_{0.5}Ce_{0.5}$ showed significant reduction. The average Pt particle sizes < 10 nm, were successfully dispersed on different TiO_2 based supports TiO_2Mn, TiO_2Ce, $TiO_2Mn_{0.5}Ce_{0.5}$

and TiO_2Ce/C by alcohol reduction method. The TEM images displayed agglomeration of the nanoparticles on the support. The Pt loading on the electrocatalysts were similar, except for Pt/TiO_2, that exhibited lower Pt:Ti ratio. Furthermore, Pt/TiO_2Mn exhibited weaker SMSI effect compared to the other electrocatalysts, whilst Pt/TiO_2Ce demonstrated lower O_V content. The $Pt/TiO_2Mn_{0.5}Ce_{0.5}$ exhibited enhanced electrocatalytic behaviour in $K_3[Fe(CN)_6]/K_4[Fe(CN)_6]$, exhibiting low R_{ct}, high A and Γ relative to the non-carbon material, indicating the enhanced catalytic behaviour. The results indicate enhanced behaviour due to the lowered band gap and high O_V content, as it was suggested from the Tauc plot and XPS results. It was interesting to note that, Pt/TiO_2Ce, with large ΔE_p and high R_{ct} exhibited high current response. This illustrates the enhanced catalytic property that is induced by CeO_X. Moreover, carbon was added to TiO_2Ce and the corresponding electrocatalyst $Pt/TiO_2Ce/C$ showed enhanced catalytic behaviour, revealing smaller ΔE_p, lowered R_{ct}, high A and Γ due to the improved conductivity. Based on the EIS, all electrocatalysts demonstrated a pseudocapacitive behaviour and a mixed diffusion-adsorption process.

Chapter 5
Electrochemical Behaviour of the Electrocatalysts towards EOR

5.1. Results and Discussion

In this Chapter, the electrochemical behaviour of the electrocatalysts towards EOR were investigated in acid and alkaline electrolyte, respectively. The experiments were conducted using a three-electrode setup and techniques described in Section 3.4.

5.1.1. Electro-oxidation of ethanol in acidic and alkaline electrolyte

The electrochemical behaviour of the electrocatalysts for EOR were investigated in acid and alkaline media. Figure 5.1 presents the CVs of the Pt/TiO_2, Pt/TiO_2Mn, Pt/TiO_2Ce, $Pt/TiO_2Mn_{0.5}Ce_{0.5}$ electrocatalysts in (a) 0.5 M H_2SO_4 and (b) 0.5 M KOH electrolytes. All recorded CVs displayed the characteristic signal of the Pt in the electrolytes: (i) H_{ads}/H_{des} at lower potentials, (ii) double layer region, and (iii) Pt-O oxidation and reduction peaks at the higher potentials. The H_{ads}/H_{des} peaks were observed at a low potential range of – 0.20 to 0.16 and – 1.0 to – 0.5 V in the 0.5 M H_2SO_4 and 0.5 M KOH, respectively. The ECSA of the electrocatalysts were calculated according to the area of H_{des} peak using Equation 3.4 [37].

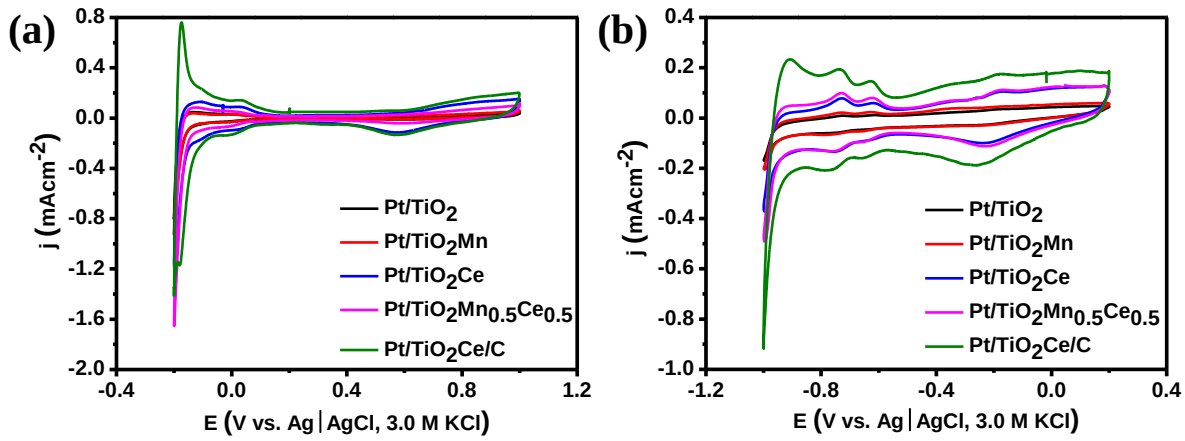


Figure 5.1: Cyclic voltammograms of the electrocatalysts in N_2 purged (a) 0.5 M H_2SO_4 and (b) 0.5 M KOH collected at a scan rate of 25 mVs^{-1}.

The ECSA for the electrocatalysts, Pt/TiO_2, Pt/TiO_2Mn, Pt/TiO_2Ce, $Pt/TiO_2Mn_{0.5}Ce_{0.5}$ were calculated and reported in Table 5.1. As seen, the electrocatalysts modified with Ce showed two times higher ECSA relative to the ones without CeO_X, (Pt/TiO_2 and Pt/TiO_2Mn) electrocatalysts in both media (0.5 M H_2SO_4 and 0.5 M KOH). This observation suggests that the ECSA of the electrocatalysts were enhanced upon the addition of CeO_X to the TiO_2 supports. The electrocatalytic activities of the electrocatalysts towards the EOR were investigated by CV in acid and alkaline electrolytes separately, as displayed in Figure 5.2 Summary of the EOR activities for the electrocatalysts in the two electrolytes (H_2SO_4 and KOH) are reported in Table 5.1. The forward peak current (i_{fp}) of the electrocatalysts were normalized by the geometric surface area of the working electrode (0.0707 cm^2) to give current density (j_{fp}). By comparing the j_{fp} and E_{onset} from the respective CVs, the catalytic behaviours of the electrocatalysts were established.

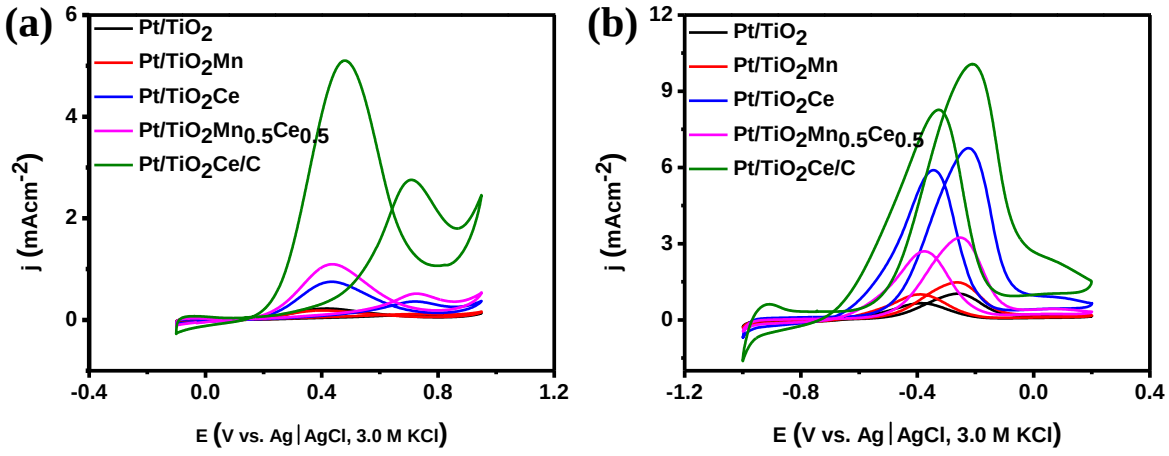


Figure 5.2: Cyclic voltammograms of the electrocatalysts in N_2 purged (a) 0.5 M H_2SO_4 + 0.5 M EtOH and (b) 0.5 M KOH + 0.5 M EtOH collected at a scan rate of 50 mVs^{-1}.

The EOR activity increased in the following order: Pt/TiO_2 < Pt/TiO_2Mn < $PtTiO_2Ce$ ≤ $Pt/TiO_2Mn_{0.5}Ce_{0.5}$ < $PtTiO_2Ce/C$. These results agree with the calculated ECSA and ΔE_p values (Table 5.1), since $PtTiO_2Ce$, $Pt/TiO_2Mn_{0.5}Ce_{0.5}$ and $PtTiO_2Ce/C$ display higher ECSA and faster e^- transfer. The high catalytic activity of the CeO_X containing electrocatalysts in both acid and alkaline media, respectively implies that the EOR activity was enhanced by the presence of Ce or CeO_X in the electrocatalysts which promotes the bifunctional mechanism [4]. This result is attributed to the ability of the ceria to adsorb and release oxygen containing species (OH_{ads}). During the EOR, the dissociation of ethanol molecules into CO_{ads}-like species occurs, thus the presence of oxygen groups (OH_{ads}) from CeO_X on the surface of the electrocatalyst facilitates the oxidation of adsorbed species to acetaldehyde and/or acetic acid at lower potentials unlike Pt surfaces alone [132–134]. In addition, all the electrocatalysts improved catalytic behaviour in alkaline electrolyte showing low $E_{onset,}$ E_p and high j. The enhanced electrochemical activities in alkaline electrolyte are attributed to the abundant hydroxyl (OH^-) species in the 0.5 M KOH that facilitate removal of CO_{ads}-like species revealing more catalyst active sites for the EOR to take place and the absence of sulphate anions (SO_4^{2-}

), which acts as catalyst poisons in acidic media. Hence, more active sites are available for the EOR to occur continuously [2,9]. As expected, the addition of carbon enhanced the activity towards the EOR. This result was attributed to the widely distributed active sites on the high surface area TiO_2Ce/C hybrid support (increased ECSA), as well as the electronic conductivity of carbon unlike TiO_2Ce alone.

The anodic to cathodic peak current ratio j_{fp}/j_{rp} was determined for all the electrocatalysts to establish the tolerance to poisoning species on the surface of the electrodes. A high ratio demonstrates the tolerance of the electrocatalysts towards poisonous species and a low ratio demonstrates an acceptable or poor tolerance [10]. Table 5.1 presents the results and the ratios. The ratios show an unexpected trend. The Pt/TiO_2 and Pt/TiO_2Mn exhibited high j_{fp}/j_{rp} ratio compared to the Pt/TiO_2Ce and $Pt/TiO_2Mn_{0.5}Ce_{0.5}$. This suggests that Pt/TiO_2 and Pt/TiO_2Mn are more tolerant to the produced poisonous species during EOR. It seems like the CeO_X activates the bifunctional mechanism earlier than on TiO_2 and TiO_2Mn, which explains the observed low onset potential. However, as the reaction reaches the anodic peak potential, the CeO_X may be less active in facilitating the removal of adsorbed reaction intermediate species. As a result lower j_{fp}/j_{rp} ratios on CeO_X containing materials were observed. However, it is important to note that, a thorough study like carbon monoxide stripping experiment is essential to support the suggestion above. Thus, the obtained results indicate that the enhanced current response at low potentials on Pt/TiO_2Ce and $Pt/TiO_2Mn_{0.5}Ce_{0.5}$ were attributed to the fast electron transport, large ECSA and a high probability of early oxidation of CO-like species on the electrocatalysts facilitated by CeO_X.

Table 5.1: Electrochemical properties of the catalysts studied in both acidic and alkaline media.

Electrocatalysts	**ECSA** ($cm^2\ mg^{-1}_{Pt}$)	E_{onset} **(mV)**	E_{fp} **(mV)**	ΔE_p **(mV)**	j_{fp} **(mA** cm^{-2}**)**	j_{fp}/j_{rp}
0.5 M H_2SO_4						
Pt/TiO_2	22.9	255.8	736.5	311	0.109	0.49
Pt/TiO_2Mn	20.2	211.4	735.1	330	0.117	0.62
Pt/TiO_2Ce	49.5	201.4	722.6	284	0.363	0.48
$Pt/TiO_2Mn_{0.5}Ce_{0.5}$	41.8	168.7	725.9	288	0.517	0.47
$Pt/TiO_2Ce/C$	158.0	175.9	711.2	232	2.75	0.54
0.5 M KOH						
Pt/TiO_2	21.8	-505.0	-217.5	127	1.04	1.6
Pt/TiO_2Mn	21.9	-537.6	-258.9	129	1.48	1.5
Pt/TiO_2Ce	41.8	-626.5	-223.0	121	6.76	1.2
$Pt/TiO_2Mn_{0.5}Ce_{0.5}$	41.3	-559.9	-254.3	125	3.26	1.2
$Pt/TiO_2Ce/C$	142.0	-650.1	-210.8	116	10.1	1.2

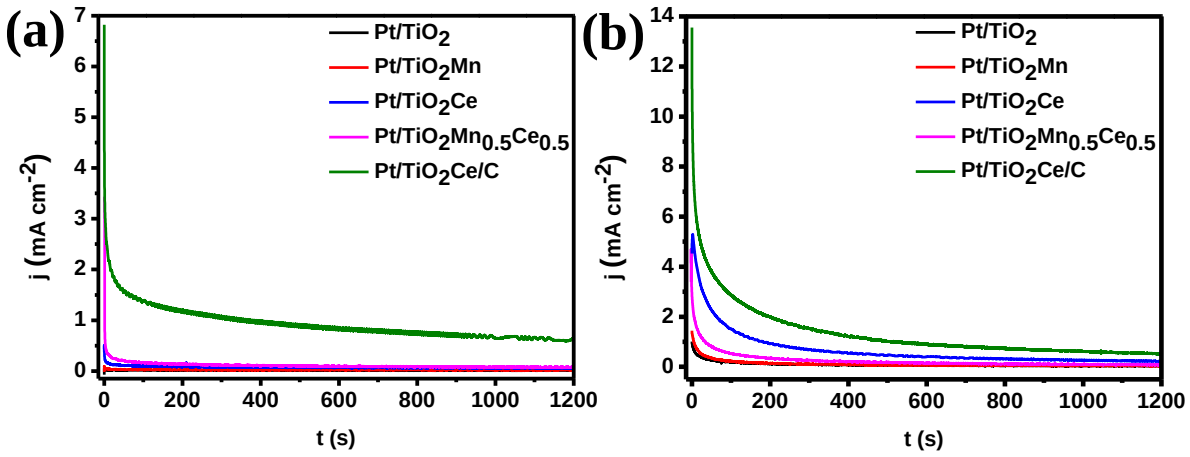


Figure 5.3: Current-time curves recorded at 0.70 and – 0.30 V in (a) 0.5 M H_2SO_4 and (b) 0.5 M KOH.

The chronoamperometric measurements were conducted at a fixed potential where the maximum EOR in 0.5 M H_2SO_4 and 0.5 M KOH occurs, for 1200 s and the resultant curves are shown in Figure 5.3. A rapid decay in current density was observed for the first few seconds owing to the adsorption of the intermediates (CO_{ads}-like) on the active sites [2,9,91]. This is followed by steady current densities over a time. The rate at which the current stabilizes is an indication of the rate at which poisoning of the electrocatalysts occurs. Therefore, from Figure 5.3, the Pt/TiO_2Ce/C exhibits the slowest rate in current decrease in acidic and alkaline media, respectively, showing high initial *j* as well as steady state current densities. On other hand, the electrocatalysts, Pt/TiO_2 and Pt/TiO_2Mn demonstrated a faster rate in current decrease, unlike Pt/TiO_2Ce, Pt/$TiO_2Mn_{0.5}Ce_{0.5}$ at low *t* less than 50s and 200s in acid and alkaline electrolytes, respectively. The electrocatalysts showed further decrease in *j* as time elapses, however, slower decrease rates were observed for Pt/TiO_2Ce and Pt/$TiO_2Mn_{0.5}Ce_{0.5}$, demonstrating the improved stability of the electrocatalysts especially in the alkaline electrolyte.

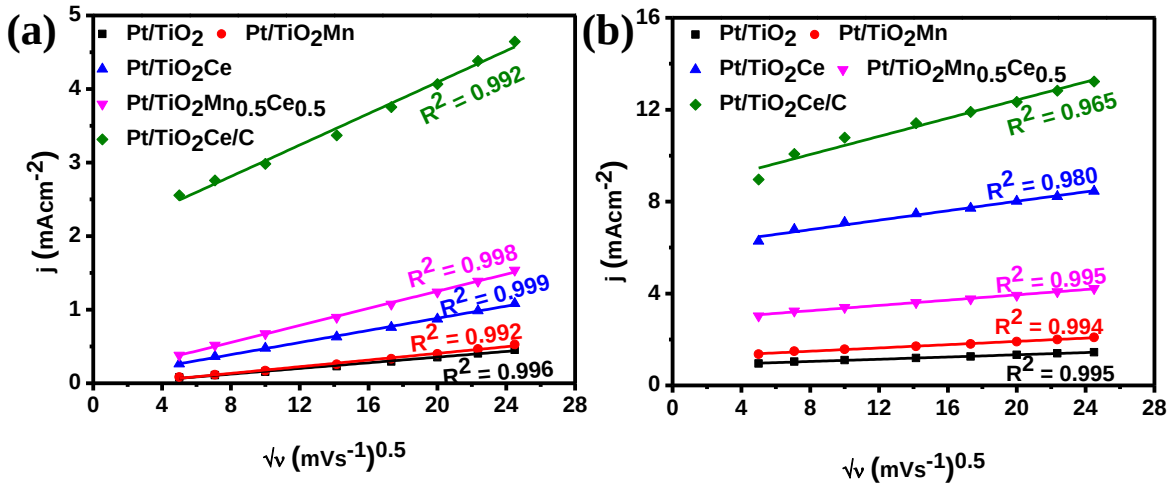


Figure 5.4: The i_p vs. $\sqrt{v}$ plots for the electrocatalysts in (a) 0.5 M H_2SO_4 and (b) 0.5 M KOH.

The effect on peak current with an increase in current on the electrocatalysts towards EOR was conducted in both media for scan rates ranging from 25 – 600 mVs^{-1} to investigate the mass transport (diffusion or adsorption) properties that occurs on the surface of the electrodes. The i_p vs. $\sqrt{v}$ plots for the electrocatalysts are shown in Figure 5.4. The electrocatalysts demonstrate an acceptable linear relationship in both the acid and alkaline electrolyte, indicative of a mixed adsorption-diffusion controlled process on the electrocatalysts.

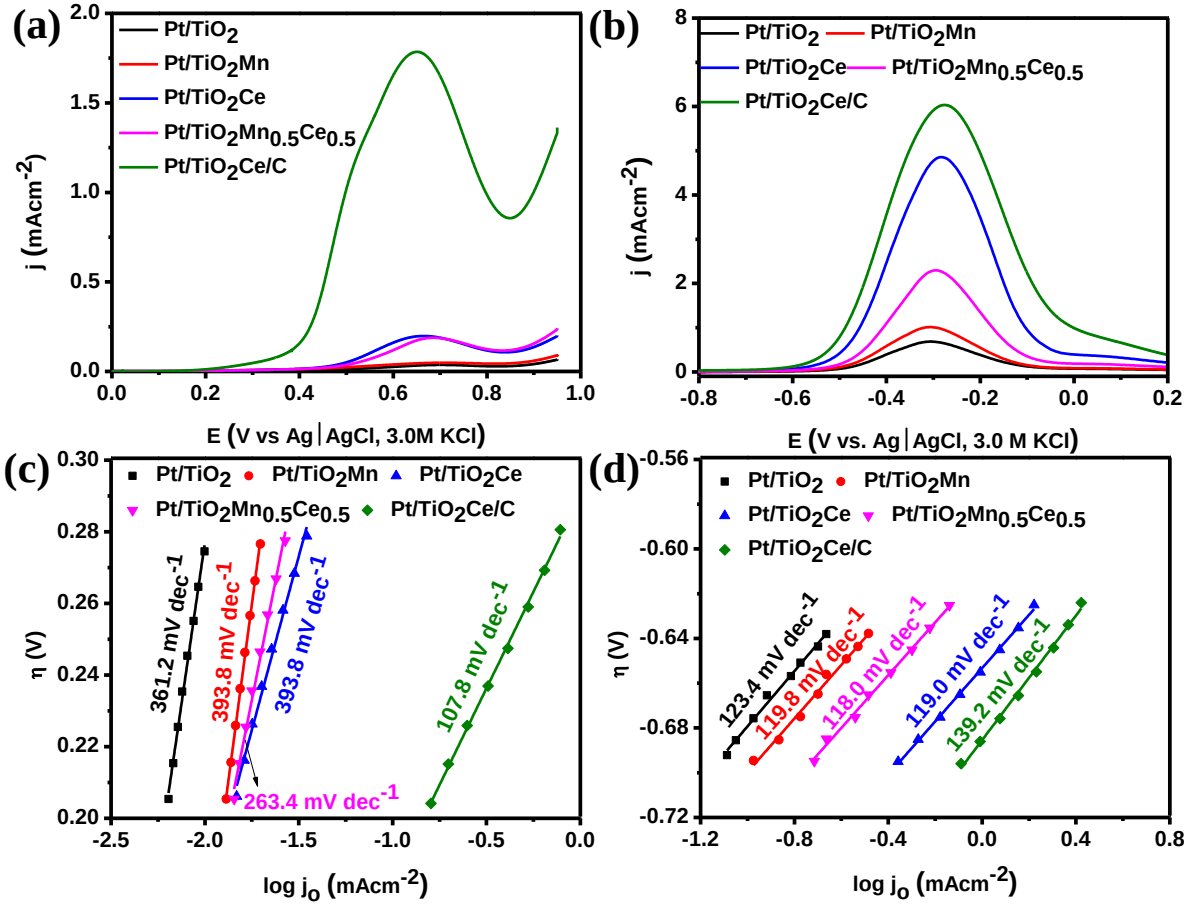


Figure 5.5: The (a,b) linear sweep voltammograms and (c,d) Tafel plots of the electrocatalysts in 0.5 M H_2SO_4 and 0.5 M KOH.

Figure 5.5a and b displays the LSV of the electrocatalysts collected at 5 mVs^{-1} in acid and alkaline media containing 0.5 M EtOH, respectively. The curves show an anodic peak which is due to the oxidation of EtOH. The Tafel plots (η vs log (j)) acquired from LSV in both media containing 0.5 M EtOH are shown in Figure 5.5c and d with the corresponding Tafel slopes. In acid media, high Tafel slope values were observed, relative to the Tafel slope for Pt/C (120.0 mV dec^{-1}). This result is accounted for by the presence of surface metal oxides on the electrocatalyst and the sluggish kinetics on the surface of the electrocatalysts, due to the surface blockage by SO_4^{2-} species [15,135]. The reduced Tafel slope for $Pt/TiO_2Ce/C$, suggests that there is difference in the nature of the electrocatalyst across the material compared to the non-carbon electrocatalysts and indicates an improved catalytic activity. Furthermore, the obtained

Tafel slopes in alkaline electrolyte were *ca.* 120.0 mV dec^{-1} which suggests that the EOR occurs *via* a dual-path way mechanism as proposed by Tripkovic [135]. Firstly, EtOH is oxidized to reaction intermediates (carbonaceous species; CO and CH_x) at lower potentials which adsorb onto the surface; and secondly, the formation of acetyl species that can further undergo oxidation removal by the adsorbed OH_{ads}. Also, the similar slopes imply that the rate determining steps were the same on all the electrocatalysts [92]. The exchange current densities of the electrocatalysts are reported in Table 5.2 where $Pt/TiO_2Ce/C$ exhibited high j_o, illustrating an increased rate of reaction relative to the other electrocatalysts [105]. Also, higher j_o were observed by the electrocatalysts in alkaline electrolyte, indicative of the enhanced behaviour.

Table 5.2: Exchange current densities of the electrocatalysts in both acidic and alkaline media.

Electrocatalysts	Pt/TiO_2	Pt/TiO_2Mn	Pt/TiO_2Ce	$Pt/TiO_2Mn_{0.5}Ce_{0.5}$	$Pt/TiO_2Ce/C$
0.5 M H_2SO_4					
$\boldsymbol{j_o \times 10^{-2}}$ **(mA cm^{-2})**	0.61	1.23	1.30	1.31	14.3
0.5 M KOH					
$\boldsymbol{j_o \times 10^{-2}}$ **(mA cm^{-2})**	6.11	9.2	15.6	36.9	72.8

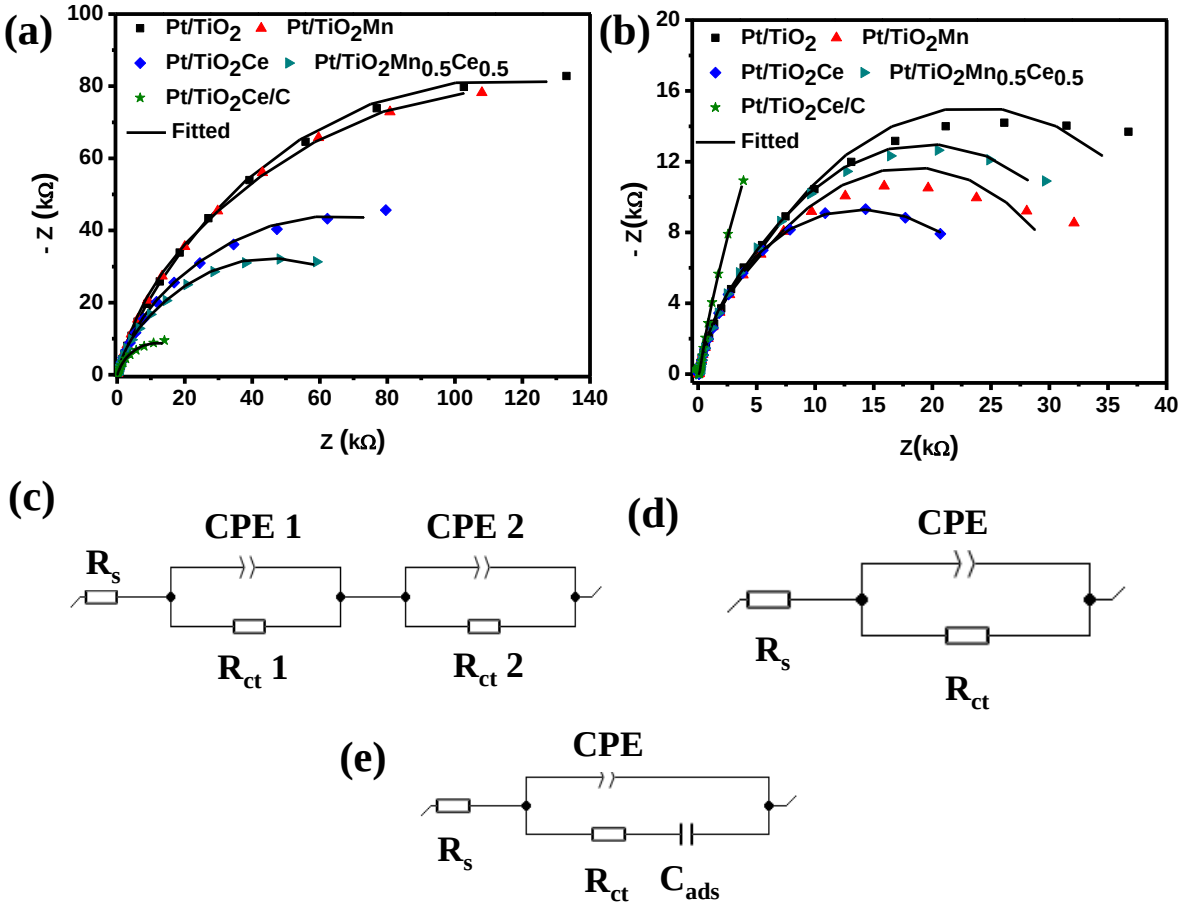


Figure 5.6: (a,b) The fitted Nyquist plots of the electrocatalysts in both electrolytes, Equivalent electrochemical circuits of (c) Pt/TiO_2, Pt/TiO_2Mn and $Pt/TiO_2Mn_{0.5}Ce_{0.5}$, (d) Pt/TiO_2Ce and (e) $Pt/TiO_2Ce/C$ in acidic and alkaline electrolyte.

The electrochemical performances of the electrocatalysts towards the EOR, were further investigated by EIS measurements at a fixed OCV and frequency range of 0.1 Hz – 100 kHz. Figure 5.6 displays the Nyquist plots and the EEC that was used to fit the experimental data. The circuit models consists of the R_s, R_{ct} and *CPE*, an additional element *CPE* 2 or C_{ads} was due to the adsorptive behaviour of the electrocatalysts [9,136,137]. The $Pt/TiO_2Ce/C$ exhibits a low R_{ct} compared to the other electrocatalysts in acid and alkaline electrolytes, as highlighted in Table 5.3. This result is attributed to an enhanced electrical conductivity on the materials upon the addition of carbon. The presence of *CPE* in all electrocatalysts (reported in Table 5.4)

is on account of the roughness of the electrode surface and the adsorption or capacitive behaviour of the electrodes [126,130]. It is worth noting, the absence of *CPE 2* or C_{ads} and R_{ct} 2or R_{ads} on the EEC obtained for Pt/TiO_2Ce, indicative of the less adsorptive nature of the electrocatalysts towards the reaction intermediates. This further explains the enhanced catalytic behaviour displayed by the electrocatalyst towards EOR compared to non-CeO_X containing electrocatalyts.

Table 5.3: Resistance parameters of the electrocatalysts for EOR studied in both acidic and alkaline media.

Electrocatalysts	R_s **(Ω)**	R_{ct1} **(kΩ)**	R_{ct2} **(kΩ)**	R_{tot} **(kΩ)**
0.5 M H2SO4				
Pt/TiO_2	41.46 (1.0)	224.0 (0.001)	3.09 (0.0001)	227.1 (0.001)
Pt/TiO_2Mn	40.9 (0.29)	208.5 (0.39)	35.3 (0.12)	243.8 (0.51)
Pt/TiO_2Ce	44.5 (0.23)	115.8 (0.0072)	-	115.8 (0.007)
Pt/$TiO_2Mn_{0.5}Ce_{0.5}$	44.84 (0.27)	84.0 (0.16)	4.63 (0.015)	88.6 (0.18)
Pt/TiO_2Ce/C	78.86 (1.0)	23.6 (0.001)	-	23.6 (0.001)
0.5 M KOH				
Pt/TiO_2	60.2 (0.29)	28.9 (0.12)	12.8 (0.11)	41.7 (0.23)
Pt/TiO_2Mn	61.5 (0.29)	12.7 (0.082)	19.2 (0.094)	31.9 (0.18)
Pt/TiO_2Ce	64.4 (0.23)	26.0 (0.0049)	-	26.0 (0.0049)
Pt/$TiO_2Mn_{0.5}Ce_{0.5}$	59.6 (0.28)	13.1 (0.19)	20.9 (0.19)	34.0 (0.38)
Pt/TiO_2Ce/C	75.9 (0.31)	0.68 (0.052)	-	0.68 (0.052)

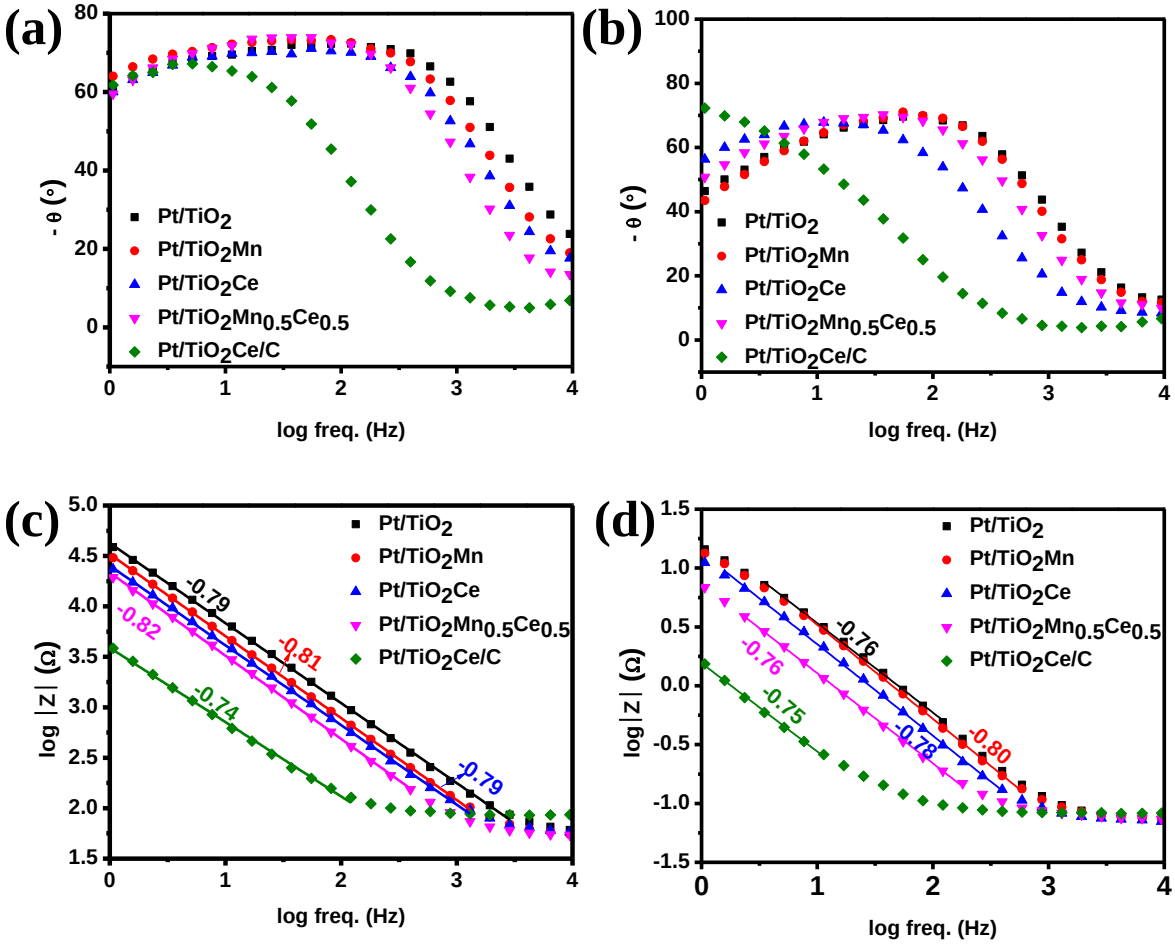


Figure 5.7: The Bode impedance plots (a, b) phase angle vs. log frequency and (c, d) log Z vs. log frequency.

Figure 5.7 a-d shows the Bode impedance plots of the electrocatalysts in both electrolytes. The phase angles for all the electrocatalysts are presented in Table 5.4. All values are > - 45°, indicative of a mixed adsorption and diffusion-limited process on the electrocatalysts [131]. The slope values from the log Z vs. log frequency are presented in Figure 5.7 (c and d). All slopes are > - 0.5, illustrative of pseudocapacitive behaviour of the electrocatalysts, further confirmed by the values of *a*, presented in Table 5.4.

Table 5.4: Pseudocapacitance parameters of the electrocatalysts for EOR studied in both acidic and alkaline media.

Electrocatalysts	***CPE*$_1$ (µF)**	***a*$_1$**	***CPE*$_2$/ C_{ads} (µF)**	***a*$_2$**	**-θ (°)**
0.5 M H2SO4					
Pt/TiO_2	5.62 (1.00)	0.80 (0.88)	27.0 (0.001)	1.00 (0.50)	71.8
Pt/TiO_2Mn	11.1 (0.021)	0.78 (0.50)	13.2 (0.040)	0.94 (0.50)	73.1
Pt/TiO_2Ce	8.49 (0.0006)	0.81 (0.50)	-	-	71.5
$Pt/TiO_2Mn_{0.5}Ce_{0.5}$	12.2 (0.007)	0.82 (0.50)	26.0 (0.00)	1.00 (1.00)	74.7
$Pt/TiO_2Ce/C$	51.7 (1.0)	0.82 (0.88)	41.17 (0.0)	-	67.7
0.5 M KOH					
Pt/TiO_2	25.8 (0.0002)	0.94 (0.51)	12.1 (0.020)	0.81 (0.50)	69.7
Pt/TiO_2Mn	11.3 (0.023)	0.82 (0.50)	30.1 (0.0002)	0.98 (0.53)	71.6
Pt/TiO_2Ce	27.8 (0.0060)	0.81 (0.50)	-	-	68.5
$Pt/TiO_2Mn_{0.5}Ce_{0.5}$	17.6 (0.081)	0.81 (0.50)	38.9 (0.0006)	0.98 (0.53)	70.5
$Pt/TiO_2Ce/C$	119.0 (1.10)	0.80 (0.50)	15.0 (1.06)	-	72.5

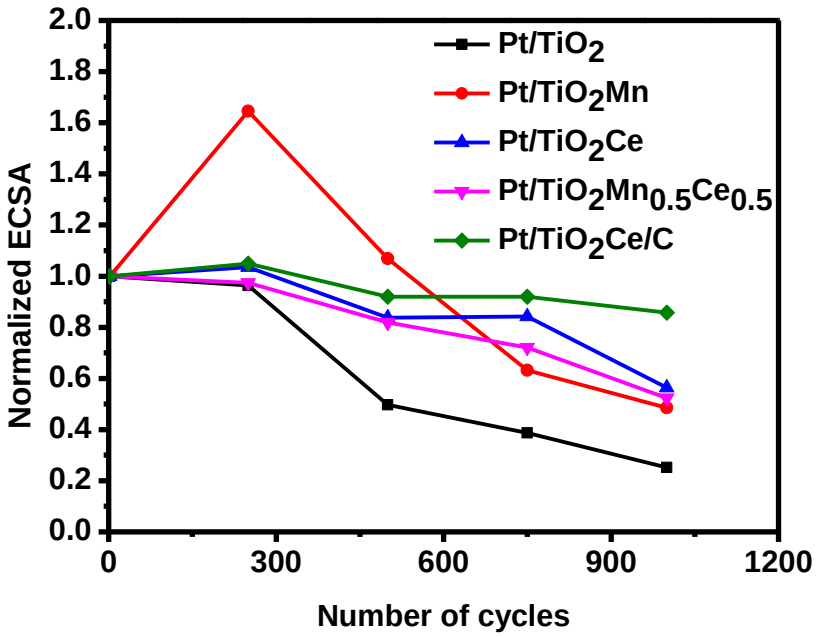


Figure 5.8: Variations of the ECSA of the electrocatalysts with the cycle number during the ADT.

The durability of the electrocatalysts was evaluated by potential cycling from – 0.20 to 1.00 V for 1000 cycles in 0.5 M H_2SO_4 electrolyte. The change in ECSA with the number of potential cycles is shown in Figure 5.8. Initially, the ECSA increased, attributed to the removal of the surface oxides on the active sites. Thereafter, the ECSA reduced with increasing number of cycles. The percentage loss at the end of 1000 cycles is 75.3, 51.6, 43.0, 47 and 14 % for the Pt/TiO_2, Pt/TiO_2Mn, Pt/TiO_2Ce, $Pt/TiO_2Mn_{0.5}Ce_{0.5}$ and $Pt/TiO_2Ce/C$, respectively. This indicates the higher stability of the Pt/TiO_2Ce and $Pt/TiO_2Mn_{0.5}Ce_{0.5}$ relative to the other electrocatalysts. The degradation of ECSA with an increase in potential cycle is attributed to dissolution and/or agglomeration of the Pt nanoparticles [38,85,138]. Therefore, this illustrates the ability of CeO_X to minimize the Pt nanoparticle agglomeration unlike TiO_2 alone. Moreover, the high coverage of Pt active sites by MnO_X was indicated by the significant increase in ECSA after 200 cycles, this explains the low ECSA observed for the Pt/TiO_2Mn in Table 5.1.

5.2. Conclusion

The Pt-based electrocatalysts supported over TiO_2, TiO_2Mn, TiO_2Ce and $TiO_2Mn_{0.5}Ce_{0.5}$ were prepared by an alcohol reduction method. The behaviour of the electrocatalysts towards EOR was investigated in acid and alkaline electrolyte, respectively. The $Pt/TiO_2Mn_{0.5}Ce_{0.5}$ and Pt/TiO_2Ce exhibited enhanced electrocatalytic behaviour in acid and alkaline electrolyte, respectively, compared to Pt/TiO_2 and Pt/TiO_2Mn. This was attributed to the high ECSA, small ΔE_p and low R_{ct} demonstrated by the electrocatalysts. The results indicate the enhanced electron transport and catalyst distribution in the presence of CeO_X in the TiO_2 based supports towards the EOR. As expected, faster electron transport and high j_o was observed in alkaline medium, attributed to the abundant OH_{ads} species unlike the strong adsorbates SO_4^{2-} present in acidic electrolyte. The EIS study demonstrated mixed adsorption-diffusion processes on the surface of the electrocatalysts. The poor performance displayed by Pt/TiO_2 and Pt/TiO_2Mn are attributed to the low ECSA, slow charge transfer and high R_{ct}. Hence, the addition of CeO_X in the TiO_2-based electrocatalysts is promising compared to the addition of MnO_X and TiO_2 alone.

Chapter 6

Electrochemical Behaviour of the Electrocatalysts towards ORR

6.1. Results and Discussion

In this chapter, the electrochemical behaviour of the electrocatalysts: Pt/TiO_2, Pt/TiO_2Mn, Pt/TiO_2Ce, $Pt/TiO_2Mn_{0.5}Ce_{0.5}$ and $Pt/TiO_2Ce/C$ towards ORR was investigated in 0.5 M H_2SO_4 and 0.1 M KOH electrolyte. The experiments were conducted using a three-electrode setup and techniques described in Section 3.4.

6.1.1. Oxygen reduction reaction in acidic and alkaline electrolyte

Figure 6.1 shows the CVs recorded for the Pt/TiO_2, Pt/TiO_2Mn, Pt/TiO_2Ce and $Pt/TiO_2Mn_{0.5}Ce_{0.5}$ and $Pt/TiO_2Ce/C$ in acid and alkaline electrolyte solutions. The CVs show characteristic peaks of the Pt-based electrocatalysts in the two electrolytes respectively. The low potential region (0.0 to 0.2 V) shows the Pt-$H_{ads/des}$ peaks. The area under the H_{des} peak was calculated and used to estimate the ECSA using Equation 3.2 [14].

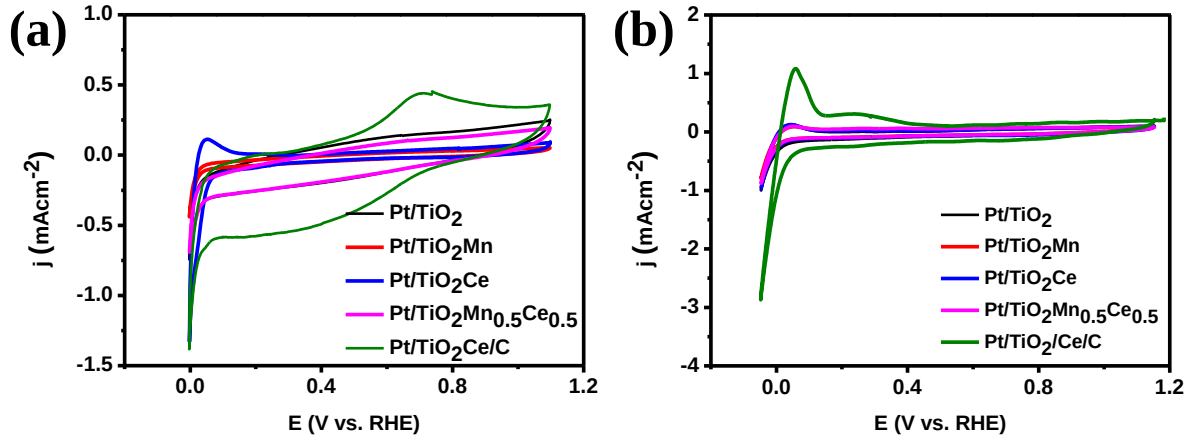


Figure 6.1: CVs of the electrocatalysts in (a) 0.5 M H_2SO_4 and (b) 0.1 M KOH collected at 25 mVs^{-1}.

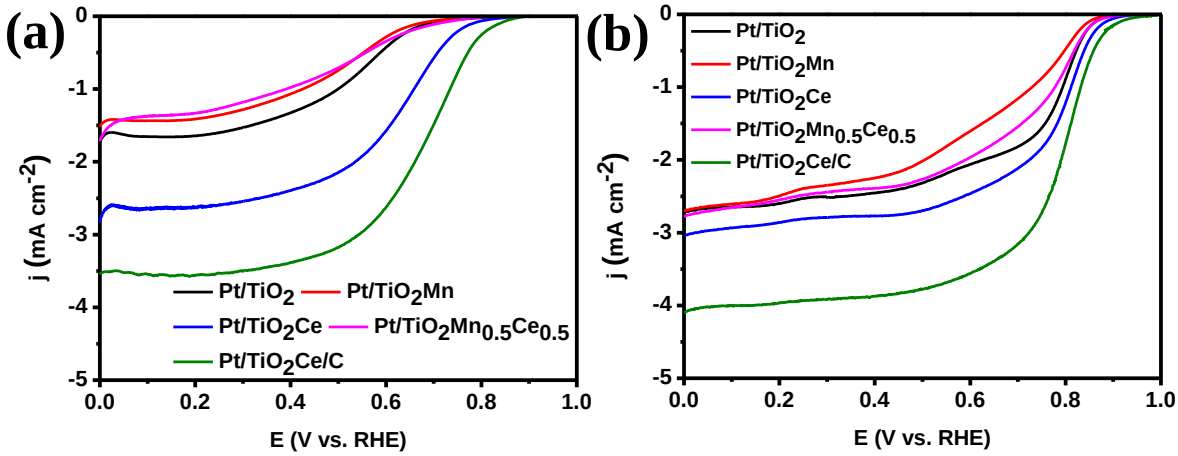


Figure 6.2: LSVs of the electrocatalysts in O_2 saturated (a) 0.5 M H_2SO_4 and (b) 0.1 M KOH collected at 1600 rpm, 10 mVs^{-1}.

The electrochemical activities of the electrocatalysts towards the ORR were investigated by RDE measurements at a rotation speed of 1600 rpm and a scan rate of 10 mVs^{-1} in 0.5 M H_2SO_4 and 0.1 M KOH saturated with O_2 separately. Figure 6.2a and b displays the LSV plots of the electrocatalysts in acid and alkaline electrolyte, respectively. The ORR activities of the electrocatalysts were determined by comparing the E_{onset}, $E_{1/2}$ and diffusion-limited current density (j_d) reported in Table 6.1. From Figure 6.2 a and b, the Pt/TiO_2Ce exhibits a more positive E_{onset}, $E_{1/2}$ and higher j_d in both electrolytes relative to the other electrocatalysts. The order of the best ORR activity shown by the electrocatalyts is $Pt/TiO_2Ce/C$ > Pt/TiO_2Ce > $Pt/TiO_2Mn_{0.5}Ce_{0.5}$ > Pt/TiO_2 > Pt/TiO_2Mn in both electrolytes. It is observed that the presence of CeO_X in the supports enhances the ORR activity in the TiO_2-based electrocatalysts, which suggests that there exists a favourable synergy between Pt nanoparticles and CeO_2 in the electrocatalysts through the continuous supply of O_2 to the adjacent Pt nanoparticles by the CeO_X and the enhanced distribution of the Pt nanoparticles. A similar observation was reported by Lee and co-workers [139] where PtCo-CeO_X exhibited an enhanced catalytic activity towards ORR unlike PtCo alone. The authors suggested this enhanced behaviour to be ascribed

to the improved adsorption and desorption of O_2 on the PtCo, due to the electronic effect on the active sites. On the other hand, the Pt/TiO_2Mn exhibited the poor activity in both electrolytes, which could be attributed to the blocked actives sites by the MnO_X, as indicated from the accelerated durability tests in Chapter 5. It is worth noting that Pt/TiO_2 showed better catalytic activity compared to Pt/TiO_2Mn, almost similar to $Pt/TiO_2Mn_{0.5}Ce_{0.5}$. This enhanced behaviour of the electrocatalyst may be attributed to the exposed active sites unlike Pt/TiO_2Mn. Furthermore, the lowered binding energy observed from the XPS $Pt4f_{7/2}$ spectra may improve the catalytic activity of the electrocatalyst by weak adsorption of the oxygenated species, enhancing the adsorption and desorption of the analyte and products, respectively. Carbon enhance the ECSA and conductivity of the Pt/TiO_2, further improving the electrocatalysts behaviour showing positive shifts in E_{onset}, $E_{1/2}$ and high j_d.

Table 6.1: Electrocatalytic activities of the electrocatalysts for the ORR using RDE. Collected at 1600 rpm, 10mVs^{-1} in O_2 saturated 0.5 M H_2SO_4 and 0.1 M KOH electrolyte.

Electrocatalysts	**ECSA** ($m^2 g^{-1}_{Pt}$)	E_{onset} **(V)**	$E_{1/2}$ **(V)**	j_d **(mAcm^{-2})**
0.5 M H_2SO_4				
Pt/TiO_2	4.98	0.714	0.559	-1.595
Pt/TiO_2Mn	2.82	0.692	0.554	-1.426
Pt/TiO_2Ce	7.67	0.801	0.709	-2.628
$Pt/TiO_2Mn_{0.5}Ce_{0.5}$	3.11	0.731	0.559	-1.651
$Pt/TiO_2Ce/C$	16.7	0.850	0.771	-3.5105
0.1 M KOH				
Pt/TiO_2	6.62	0.867	0.820	-2.726
Pt/TiO_2Mn	7.35	0.856	0.798	-2.689
Pt/TiO_2Ce	8.34	0.890	0.838	-3.008
$Pt/TiO_2Mn_{0.5}Ce_{0.5}$	9.82	0.870	0.818	-2.778
$Pt/TiO_2Ce/C$	22.3	0.927	0.855	-4.022

Moreover, RDE measurements were performed at rotation speeds ranging from 400 to 2500 rpm in both electrolytes (not shown here). The diffusion-limited current density increased with an increase in rotation speed. The number of electrons transferred during the ORR was determined using the Koutecky-Levich (K-L) equation shown in Equation 3. The C_{O2} (1.1 and 1.2×10^{-6} mol cm^{-3}) [140], D (1.40 and 1.95×10^{-5} cm^{-2}s^{-1}) [140] and γ (10 and 8.89×10^{-3} cm^{2}s^{-1}) [77,140] constant values were used in the K-L plots for the acid and alkaline electrolyte, respectively. The corresponding K-L plots for the electrocatalysts together with the theoretical K-L plots for the 2 and 4 electron processes for the ORR are shown in Figure 6.3a-

e and Figure 6.4a-e in 0.5 M H_2SO_4 and 0.1 M KOH, respectively. The calculated *n* values for each electrocatalyst in both acid and alkaline electrolytes are presented in Table 6.2.

Table 6.2: The estimated number of electrons transferred (*n*) for the electrocatalysts.

Electrocatalysts	**0.5 M H_2SO_4**	**0.1 M KOH**
Pt/TiO_2	4.3	3.0
Pt/TiO_2Mn	4.4	4.1
Pt/TiO_2Ce	2.4	2.4
$Pt/TiO_2Mn_{0.5}Ce_{0.5}$	2.8	2.8
$Pt/TiO_2Ce/C$	4.3	4.4

As seen from the results, the *n* values are close to $4e^-$ pathway for the Pt/TiO_2, Pt/TiO_2Mn, $PtTiO_2Ce/C$, $Pt/TiO_2Mn_{0.5}Ce_{0.5}$ and $2e^-$ pathway for only the Pt/TiO_2Ce. The results indicate that the highest ORR active electrocatalyst, Pt/TiO_2Ce, favoured the $2e^-$ pathway which was unexpected. Although the ECSA and kinetics of the electrocatalysts towards ORR was enhanced by the presence of CeO_X in the electrocatalyst, the complete reduction of O_2 was hindered. This indicates a compensation of the direct reduction of O_2 in CeO_X materials studied in this work; i.e. although the E_{onset}, $E_{1/2}$ and j_d were improved by the addition of CeO_X, the reduction of O_2 occurred via the $2e^-$ process. In the case of $Pt/TiO_2Ce/C$, the addition of carbon exhibited an enhanced reduction of O_2, which may be attributed to the increased ECSA, availing more active sites for ORR to take place. On the other hand, the Pt/TiO_2Mn that displayed poor ORR activity (low j_d, negative E_{onset} and $E_{1/2}$), exhibited the $4e^-$ process. Several reports have demonstrated the enhanced electrocatalytic activity of MnO_X-based electrocatalysts towards the complete reduction of O_2. The behaviour was attributed to the ability of MnO_X to further decompose the $2e^-$ pathway reaction intermediate species, hydrogen

peroxide (H_2O_2) and (HO_2^-) formed in acid and alkaline electrolytes, respectively [95,106]. As suggested by other researchers, it is possible that the surface MnO_X present on the electrocatalysts presented in this work behave in a similar manner. The poor catalytic activity displayed by Pt/TiO_2Mn may be attributed to the stronger adsorption of the reaction intermediate species on the Pt surface. This is supported by the XPS spectra results, which exhibited a lower shift in binding energy compared to the other electrocatalyst. Thus, the oxygenated species bind weakly to Pt/TiO_2, Pt/TiO_2Ce and $Pt/TiO_2Mn_{0.5}Ce_{0.5}$ compared to Pt/TiO_2Mn.

The kinetic rate constants were estimated from the K-L plots and are presented in Table 6.3. As seen from the results, the $Pt/TiO_2Ce/C$ exhibits the highest *k* compared to the other electrocatalysts in each electrolyte solution. The results corroborate the observed ORR activity since the CeO_X containing electrocatalysts shows an increase in *k* by *ca*. 2 folds. Although the efficiency in complete reduction of O_2 was hindered, the *k* indicates the improved kinetics towards the ORR on CeO_X containing materials.

Table 6.3: The kinetic rate constants (*k*) estimated for the electrocatalysts.

Electrocatalysts	Pt/TiO_2	Pt/TiO_2Mn	Pt/TiO_2Ce	$Pt/TiO_2Mn_{0.5}Ce_{0.5}$	$Pt/TiO_2Ce/C$
0.5 M H_2SO_4					
$\boldsymbol{k \times 10^{-3}}$ **(cm s^{-1})**	0.28	0.28	0.41	0.50	2.8
0.1 M KOH					
$\boldsymbol{k \times 10^{-3}}$ **(cm s^{-1})**	0.73	0.45	1.4	0.89	0.92

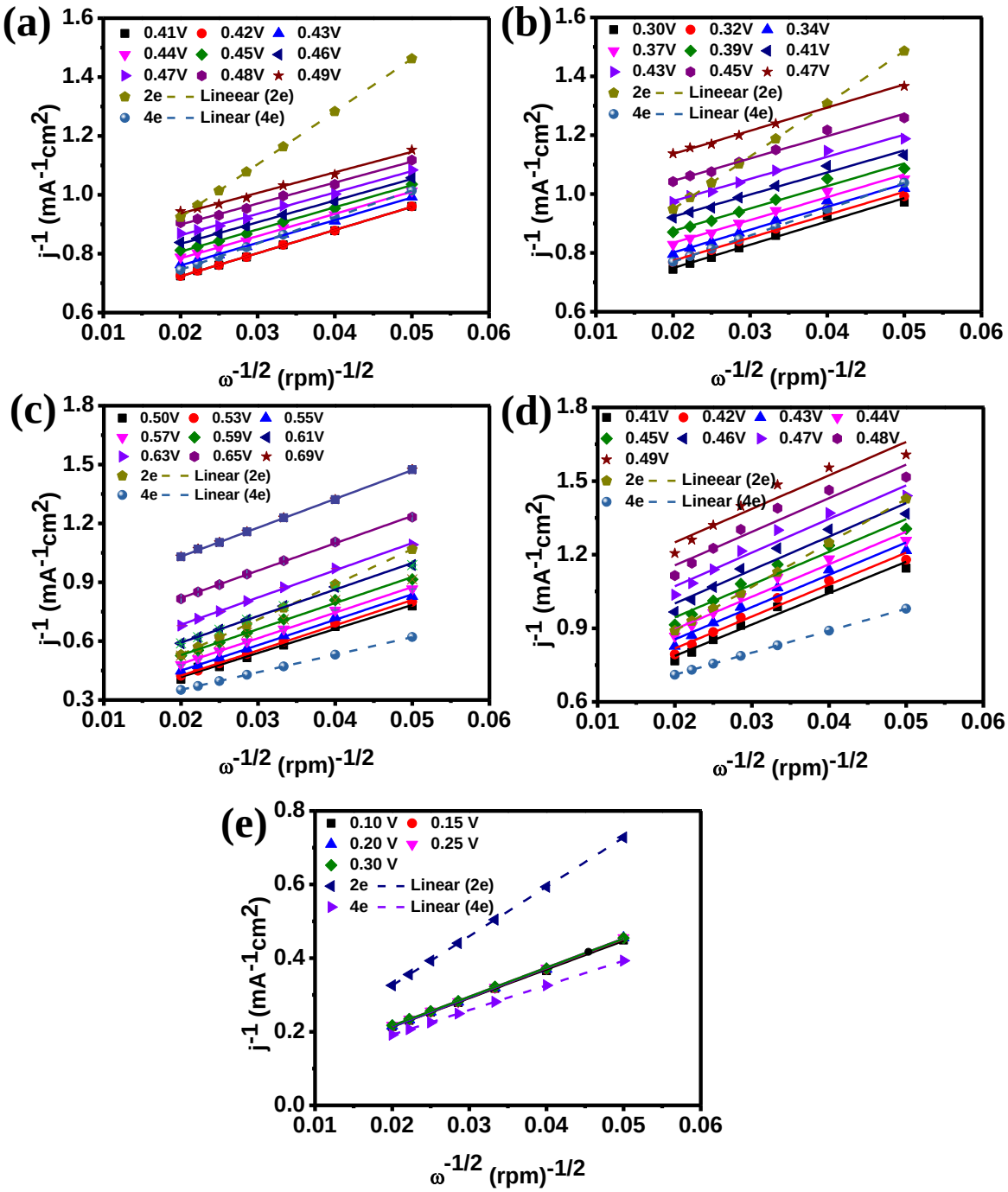


Figure 6.3: K-L plots of the electrocatalysts in 0.5 M H_2SO_4 for (a) Pt/TiO_2, (b) Pt/TiO_2Mn, (c) Pt/TiO_2Ce, (d) $Pt/TiO_2Mn_{0.5}Ce_{0.5}$ and $Pt/TiO_2Ce/C$.

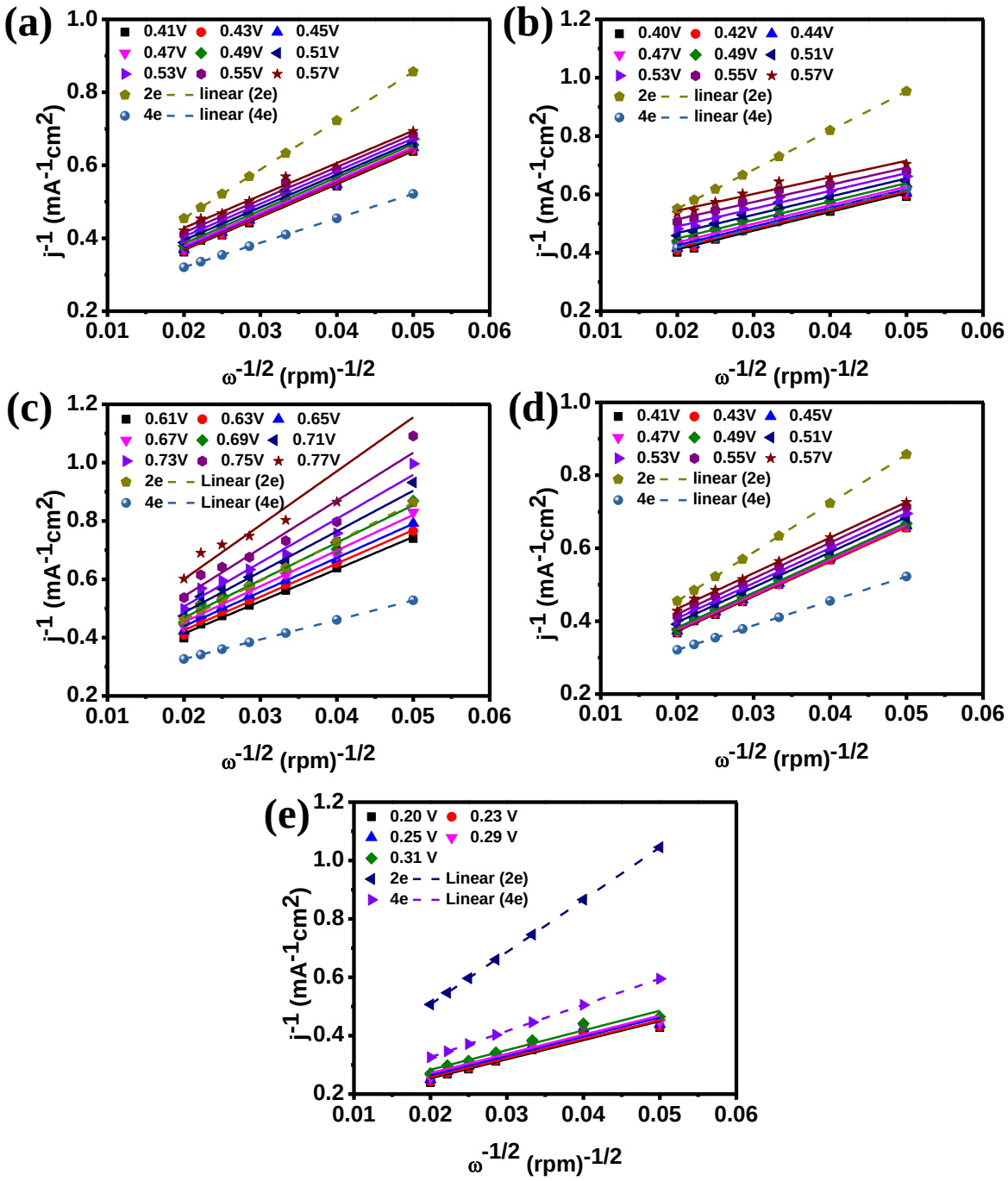


Figure 6.4: K-L plots of the electrocatalysts in 0.1 M KOH for (a) Pt/TiO_2, (b) Pt/TiO_2Mn, (c) Pt/TiO_2Ce, (d) $Pt/TiO_2Mn_{0.5}Ce_{0.5}$ and $Pt/TiO_2Ce/C$.

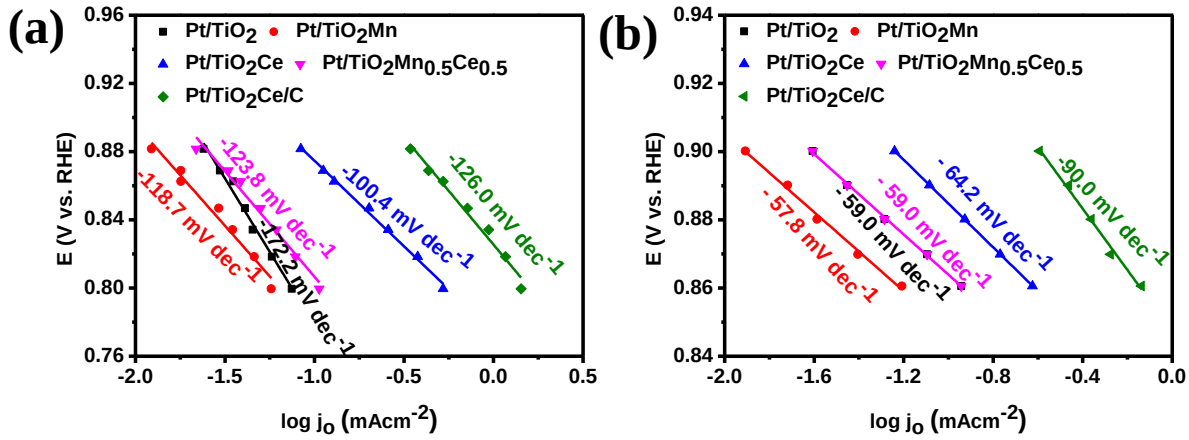


Figure 6.5: Tafel slopes of the electrocatalysts in (a) 0.5 M H_2SO_4 and (b) 0.1 M KOH.

The Tafel plots for the electrocatalysts determined from their respective LSV curves collected at 1600 rpm and scan rate of 10 mVs^{-1} are presented in Figure 6.5a and b**.** The electrocatalyst present similar Tafel slope values in acid and alkaline electrolyte, respectively which illustrate similar rate determining step. In the acidic electrolyte, the Tafel slopes presented were higher compared to the typical slope value of 60 mV dec^{-1} for Pt/C at low current density region [141]. This result is ascribed to the presence of the surface metal oxides. Previously, He and co-workers [142] deduced that in the high potential region, the formation of Pt-OH_{ads} that is associated with the dissociation of H_2O or reaction with O_2, led to low Tafel slope values. In their study, the authors demonstrated increased Tafel slope values and associated them to the presence of MO_X that inhibited or delayed the formation of Pt-O or Pt-OH, availing more active sites for O_2 adsorption. Since the electrocatalysts presented in this work presents high Tafel slopes, it suggests that the oxidation of Pt active sites (Pt-O or Pt-OH) was minimized by the presence of MO_X electrocatalyst. Furthermore, a poor catalytic activity was observed in acid electrolyte relative to the alkaline media [143]. The enhanced activity in alkaline media is promoted by the weaker adsorption of OH species on the Pt surface unlike the strong SO_4^{2-} adsorbate, which strongly bind to the active sites, blocking the adsorption of fresh O_2 molecules. Also, the electrocatalysts exhibited slope values of *ca.* 60 mV dec^{-1} alkaline

electrolyte, demonstrating the enhanced activities with lower Tafel slope values. This is in agreement with other reports on ORR in acid and alkaline electrolyte solutions [89,138].

6.2 Conclusion

The electrochemical behaviour of Pt/TiO_2, Pt/TiO_2Mn, Pt/TiO_2Ce, $Pt/TiO_2Mn_{0.5}Ce_{0.5}$ were evaluated as electrocatalysts towards the ORR. Pt/TiO_2Ce displayed high catalytic activity towards the ORR with more positive E_{onset}, $E_{1/2}$ and high j_d in acid and alkaline electrolyte solutions. The K-L plots exhibited a $2e^-$ process for ORR on Pt/TiO_2Ce. On the other hand, a $4e^-$ process was exhibited by Pt/TiO_2, Pt/TiO_2Mn, $Pt/TiO_2Mn_{0.5}Ce_{0.5}$ and $Pt/TiO_2Ce/C$, respectively. Thus the presence of CeO_X compensates the complete reduction of O_2 during the ORR. However, the coupling of TiO_2/CeO_X with carbon improved the efficiency of the electrocatalyst. This is attributed to the improved $Pt/TiO_2/CeO_X$ interaction, ECSA and conductivity of the material. Thus, the incorporation of CeO_XC in the TiO_2 based electrocatalysts is beneficial towards the ORR.

Chapter 7
Sensing Performance of $Pt/TiO_2Ce/C$

7.1 Introduction

The analysis of volatile organic compounds (VOCs) is an appealing method that is used to assess chemical compounds in liquids and solids. This is due to the general assumption by Henry's Law that; *"at a constant temperature, the concentration of gas dissolved in a liquid is directly proportional to its concentration in the air directly above the liquid"* [46,144].

The method is applicable in clinical, environmental analysis as well as food and beverage industries. For instance, VOCs in human sweat and breath contains several chemical compounds that can be used as biomarkers to diagnose human illnesses or the state of a persons' sobriety. This method, especially through breath sampling has received growing interest since it offers an easy to use, portable, non – invasive analysis that is low-cost and rapid for analysis. The detection of EtOH is also applicable in automobile industries as interlock ignition devices, commercial industries for monitoring the use of alcohol by employees whilst on duty and law enforcement agencies for the monitoring of impaired motorists. The breath alcohol detection is mostly employed by traffic officers, to enforce drinking and driving laws. Furthermore, to prevent and control the number of road accidents that occur as a result of impaired motorists [45,145–148].

BAC is defined as alcohol (EtOH) content in grams (g) per decilitre (dL) blood volume (Equation 7.1). The legal alcohol limit in South Africa (SA) is less than 50 mg per 100 mL of blood and less than 0.024 g per 10 dL of breath [46].

$$\%\,BAC = \frac{EtOH\ content\ (g)}{blood\ volume\ (dL)} \times 100 \qquad 7.1$$

FCBrAS are widely adopted as screening devices due to their accuracy, rapid responses and good linearity. The mode of detection of the BAC from a human subject is directly proportional to the BrAC since there exists a well-established ratio between the BAC and the BrAC in the alveolar (air deep inside the lungs) of around 2100:1. The blood/ breath factor renders the reliability of the method of detection. Furthermore, the factor is accepted for legal purposes since it is normally used for calibration of breath alcohol testing devices [146,147].

The operation of FCBrAS is similar to that of DEFC. Briefly, a certain volume of breath is fed into the device through a mouth piece and delivered into the anode compartment where EtOH is oxidized whilst O_2 reduction takes place on the cathode compartment. The current produced as a result of the electrochemical reactions is recorded and the relationship between the generated current and BAC is linear. This holds true since current signal of the sensors are calibrated against BAC [146].

There are limited reports on FCBrAS, especially those that employ the recently developed electrocatalysts for DEFCs.

A BrAS with MEA that consists of a solid polymer electrolyte (Nafion 115) with low Pt/C loading was fabricated by Modjtahedi and co-workers [149]. The anode and cathode electrode comprised of 0.3 and 0.03 mg cm $^{-2}$ of Pt loading, respectively. In the study, the BrAS presented a wide range detection of % BAC (0.05 – 0.2) with high linearity, using 130 times lower Pt loading compared to commercial sensors. In a study by Ghavidel and co-workers [44], Pt based alloy electrocatalysts namely; Pt-Mn/C and Pt-Cu/C were fabricated and tested for FCBrAS. The fabricated electrocatalysts' sensitivity and stability were compared to commercial electrocatalysts Pt/C and Pt_3Sn/C. The electrochemical results showed high mass sensitivities for the Pt – Cu/C, with less Pt content than the commercial catalyst [44].

It is notable from the literature review that no study has employed MO_X supported Pt

nanoparticles for FCBrAS. Therefore, in this chapter, we investigate the Pt/TiO_2Ce/C electrochemical sensing of EtOH.

7.2. Results and Discussion

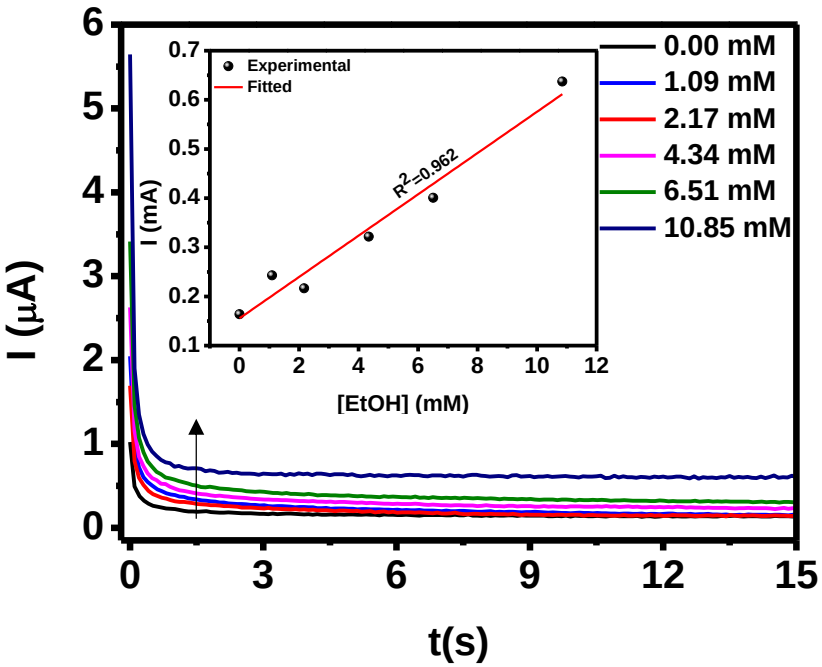


Figure 7.1: The current-time curve polarized at -0.40 V for 15 seconds and (insert) concentration against current plots.

The chronoamperometry technique was used to investigate the current response of Pt/TiO_2Ce/C for EtOH concentrations (0.00 – 10.85 mM). Figure 7.1 shows the current-time curves for Pt/TiO_2Ce/C that was obtained by adding different analyte concentrations. The curves displayed an increase in current response as a function of analyte concentration. Also, the relationship between EtOH concentration and current response is shown in Figure 7.1 (insert) and a sensitivity value of $0.042 \pm 1.31 \times 10^{-3}$ mA mM^{-1} was obtained. The limit of detection (LoD) was determined using Equation 7.2.

$$LoD = \frac{3.3\delta}{m} \qquad 7.2$$

Where, δ is the relative standard deviation of the y-intercept and m is the slope from the fitted line. The obtained LoD of the electrocatalyst is 4.56 mM.

7.3. Conclusion

A gas sensing experiment was conducted to probe the performance of the $Pt/TiO_2Ce/C$ in the alkaline environment. The preliminary results display a direct relationship between the current response and change in EtOH concentration ($R^2 = 0.962$) in the BAC range (0.00 – 10.85 mM ≡ 0.005 – 0.05 %). The preliminary results show acceptable linearity in the low concentration range.

Chapter 8
Summary and Recommendations

Non-carbon supported Pt-based electrocatalysts were synthesized using an alcohol reduction method and their electrochemical behaviour towards EOR and ORR in acid and alkaline electrolyte was evaluated and reported. Thereafter, the sensor performance of the electrocatalyst presenting an efficient activity towards EOR was probed for the development of electrocatalysts used in FCBrAS.

The annealing of the composite mixtures under hydrogen treatment was explored to improve the conductivity of the materials since it is well known that metal oxides display low conductivity. From the physical characterizations, it was observed that the TiO_2 suboxide was not produced. However, the UV-vis. spectra in particular, showed changes in band gaps of the support material, especially $Pt/TiO_2Mn_{0.5}Ce_{0.5}$ and Pt/TiO_2Mn which displayed significant shifts in bandgap, exhibiting a successful reduction in bandgaps. This was attributed to the successful doping of Mn cations into the TiO_2 lattice. This was supported by the XRD, Raman analysis and XPS results. From the XPS spectra, the electrocatalysts displayed strong metal to support interactions compared to Pt/C. Among the prepared electrocatalyts, a weaker metal to support interaction was displayed by the Pt/TiO_2Mn compared to Pt/TiO_2, Pt/TiO_2Ce and $Pt/TiO_2Mn_{0.5}Ce_{0.5}$. Also, Pt/TiO_2Ce displayed the lowest amount of O_V. This observation may be attributed to the distorted Ti^{4+} environment to small degree unlike in Pt/TiO_2, Pt/TiO_2Mn and $Pt/TiO_2Mn_{0.5}Ce_{0.5}$, that displayed significant changes. The XPS, EDS and SEM analyses confirmed the presence of each element in the respective electrocatalysts. The Pt/TiO_2 demonstrated the lowest at. % Pt loading, showing an improved loading for the composite metal oxide support materials. The TEM analysis displayed agglomeration of the Pt

nanoparticles showing an un-even distribution over the supports, possibly due to the longer refluxing conditions used to prepare the electrocatalysts. Thus, it would be recommended to optimize the refluxing conditions (temperature and time) to obtain the optimum Pt loading and size distribution.

The electron transfer behaviour on the electrocatalysts was investigated by the use of ferri-ferrocyanide electrolyte solution. The analysis indicated faster charge transfer on the $Pt/TiO_2Mn_{0.5}Ce_{0.5}$ among the electrocatalysts without carbon, demonstrating an enhanced conductivity on the material, thus showing improved charge transfer. Although, Pt/TiO_2/Ce displayed slow electron transfer from the high ΔE_p and R_{ct}, the electrocatalyst showed acceptable current response, due to the high exposure of active sites and high electrode coverage by the material compared to Pt/TiO_2 and Pt/TiO_2Mn. An addition of carbon to Pt/TiO_2/Ce resulted to improved activity attributed to the improved conductivity shown by the EIS study. All electrocatalysts exhibited a mixed adsorption-diffusion controlled process as presented by the EIS study.

The electrochemical behaviour of the electrocatalysts towards the EOR were conducted in acid and alkaline electrolyte, separately. The $Pt/TiO_2Mn_{0.5}Ce_{0.5}$ and Pt/TiO_2Ce exhibited high ECSA and electrocatalytic activity in acid and alkaline electrolyte, respectively. The lowest activity was displayed by Pt/TiO_2, attributed to the low ECSA and high R_{ct} of the electrocatalyst. This indicates the poor Pt to support interaction across the material that result in the poor conductivity of the material. It illustrates the synergistic effect induced by the addition of Mn and Ce. As a result, an enhanced performance of the Pt/TiO_2Mn, Pt/TiO_2Ce and $Pt/TiO_2Mn_{0.5}Ce_{0.5}$ was observed relative to Pt/TiO_2. This was attributed to the improved ECSA and bifunctional mechanism. Also, the addition of carbon is important, to reduce the resistance of the TiO_2-based materials, improving the conductivity and availing more active sites for the reaction to take place. The Pt/TiO_2Ce/C displayed smaller percentage loss of ECSA

in acidic electrolyte, demonstrating the enhanced stability of the composite material (TiO_2Ce/C). Hence, the addition of carbon is recommended in the use of metal oxides to reduce the R_{ct} and improved the mass transfer of the analyte and product towards and away from the electrode surface.

Moreover, the electrocatalysts were evaluated for the ORR in acid and alkaline media. Again, Pt/TiO_2Ce displayed higher limiting diffusion current density, more positive E_{onset} and $E_{1/2}$ relative to the other electrocatalysts. The Koutecky Levich plots analysis demonstrated a 2 electron transfer process on this electrocatalyst, indicating a compensation of the complete reduction of O_2 in this material. On the other hand, the Pt/TiO_2, Pt/TiO_2Mn, $Pt/TiO_2Ce/C$ and $Pt/TiO_2Mn_{0.5}Ce_{0.5}$ showed a 4 electron process. The enhanced current response and E_{onset} and $E_{1/2}$ may be attributed to the ECSA however, an explanation of the observed hindrance towards to O-O splitting requires more investigation. Although, Pt/TiO_2Mn revealed more negative shift in E_{onset} and $E_{1/2}$, the 4 electron process on the electrocatalysts exhibits its efficiency in complete reduction of oxygen. The efficiency may be due to the presence of the MnO_X that are known to facilitate the decomposition of the reaction intermediate species. The same explanation is applicable to $Pt/TiO_2Mn_{0.5}Ce_{0.5}$. In the case of, Pt/TiO_2, the enhanced behaviour is due the strong interaction between Pt and TiO_2 revealed by the XPS, resulting in weak adsorptions of the oxygenated species, revealing the modification of the Pt structure. Overall, $Pt/TiO_2Ce/C$ exhibited improved ORR activities, showing high kinetic constant rates.

Lastly, the sensing performance of $Pt/TiO_2Ce/C$ towards ethanol gas was evaluated in Chapter 7. The preliminary result shows a relatively good linearity, indicative of its' potential use as an electrocatalyst material for FCBrAS

In conclusion, the investigation of the effect of Ce and Mn on TiO_2 as co-catalysts to Pt nanoparticles revealed that there exists synergy between the MnO_X and CeO_X and the Pt

nanoparticles towards EOR and ORR, illustrated by the improved activities on the composite materials. The findings in this study are in agreement with other works where the reduction of Pt loading was illustrated by the addition of co-catalysts in the electrocatalyst material. It is recommended that metal oxides should consist of carbonaceous material, to improve their low conductivity and low surface area. As seen from the study, there was a significant improvement in the electrochemical behaviour of the material upon coupling with carbon. Also, it is recommended to optimize the amount of the metal dopants in the metal oxides, in order to identify the optimum amount required to reduce the resistance of the TiO_2-based materials. Further studies would be recommended to study the effect of the use of different reducing agents to deposit the metal nanoparticles on the supports and heat treatment of the electrocatalysts, since previous reports have demonstrated enhanced electrochemical behaviour upon annealing treatment, attributed to alloy formation.

References

[1] S. Paul and A. K. Molla, Development and Electrochemical Characterization of Al_2O_3-ZnO Composite Electro Catalytic Material for Energy Synthesis from Electro Oxidation of Ethanol, *Res. Rev. Electrochem.*, 2018, **9**, 1–12.

[2] R. Rizo, D. Sebastián, M. J. Lázaro and E. Pastor, On the Design of Pt-Sn Efficient Catalyst for Carbon Monoxide and Ethanol Oxidation in Acid and Alkaline Media, *Appl. Catal. B-Environ.*, 2017, **200**, 246–254.

[3] Y. Wang, K. S. Chen, J. Mishler, S. Chan and X. Cordobes, From Bimetallic Metal-Organic Framework to Porous Carbon: High Surface Area and Multicomponent Active Dopants for Excellent Electrocatalysis, *Appl. Energy*, 2011, **88**, 981–1007.

[4] C. Xu, R. Zeng, P. Kang and Z. Wei, Synergistic Effect of CeO_2 Modified Pt/C Catalysts on the Alcohols Oxidation, *Appl. Energy*, 2005, **51**, 1031–1035.

[5] R. Huang, G. Shao, Y. Zhang and Y. Wen, Thermal Stability of Platinum−Cobalt Bimetallic Nanoparticles: Chemically Disordered Alloys, Ordered Intermetallics, and Core− Shell Structures, *ACS Appl. Mater. Interfaces*, 2017, **9**, 12486–12493.

[6] S. Siwal, S. Thakur, Q. B. Zhang and V. K. Thakur, Electrocatalysts for Electrooxidation of Direct Alcohol Fuel Cell: Chemistry and Applications, *Mater. Today Chem.,* 2019, **14**, 100182.

[7] A. Dicks, J. Larminie, *Fuel Cells Systems Explained*, John Wiley & Sons Ltd., 2nd ed., 2003.

[8] M. Shao, Electrocatalysis in Fuel Cells, *Catalysts*, 2015, **5**, 2115 – 2121.

[9] H. Hua, C. Hu, Z. Zhao, H. Liu, X. Xie and Y. Xi, Pt Nanoparticles Supported on Submicrometer-sized TiO_2 Spheres for Effective Methanol and Ethanol Oxidation, *Electrochim. Acta*, 2013, **105**, 130–136.

[10] A. K. Ipadeola, R. Barik, S. C. Ray and K. I. Ozoemena, Bimetallic Pd/SnO_2 Nanoparticles on Metal Organic Framework (MOF)-Derived Carbon as Electrocatalysts for Ethanol Oxidation, *Electrocatalaysis*, 2019, **10**, 366–380.

[11] K. I. Ozoemena, Nanostructured Platinum-free Electrocatalysts in Alkaline Direct Alcohol Fuel Cells: Catalyst Design, Principles and Applications, *RSC Adv*., 2016, **6**, 89523–89550.

[12] C. Bianchini and P. K. Shen, Energy Efficiency Enhancement of Ethanol Electrooxidation on Pd–CeO_2/C in Passive and Active Polymer Electrolyte-Membrane Fuel Cells, *Chem. Rev*., 2009, **109**, 4183–4206.

[13] Y. Wang, Y. Yang, L. Zou, Q. Huang, Q. Li and Q. Xu, Carbon-Supported W@Pt Nanoparticles with a Pt-Enriched Surface as a Robust Electrocatalyst for Oxygen Reduction Reactions, *ChemistrySelect*, 2018, **3**, 1056–1061.

[14] D. Lim, W. Lee, D. Choi and H. Lee, Effect of Ceria Nanoparticles into the Pt/C catalyst as Cathode Material on the Electrocatalytic Activity and Durability for Low-temperature Fuel Cell, *Appl. Catal. B-Envron.*, 2010, **94**, 85–96.

[15] M. Roca-Ayats, O. Guillén-Villafuerte, G. García, M. Soler-Vicedo, E. Pastor, M.V. Martínez-Huertab, PtSn Nanoparticles Supported on Titanium Carbonitride for the Ethanol Oxidation Reaction, *Appl. Catal. B-Envron*., 2018, **237**, 382–391.

[16] F. Hasché M. Oezaslan, and P. Strasser, Activity, Structure and Degradation of Dealloyed $PtNi_3$ Nanoparticle Electrocatalyst for the Oxygen Reduction Reaction in PEMFC, *J. Electrochem. Soc*., 2012, **159**, 24–33.

[17] R. Chattot, T. Asset, J. Drnec, P. Bordet, J. Nelayah, L. Dubau and F. Maillard, Atomic-Scale Snapshots of the Formation and Growth of Hollow PtNi/C Nanocatalysts, *Nano Lett*., 2017, **17**, 2447–2453.

[18] T. Wilberforce, A. Alaswad, A. Palumbo, M. Dassisti, A.G. Olabi, Advances in Stationary and Portable Fuel Cell Applications, *Int. J. Hydrog. Energy*, 2016, **41**, 16509–16522.

[19] K. Maheshwari, S. Sharma, A. Sharma and S. Verma, A Review: Fuel Cell a Sustainable Future, *Int. J.Chem. Stud*., 2018, **6**, 2588–2591.

[20] O. Z. Sharaf, M. F. Orhan, An Overview of Fuel Cell Technology: Fundamentals and Applications, *Renew. Sustain. Energy Rev*., 2014, **32**, 810–853.

[21] A. Alaswad, A. Baroutaji, H. Achour, J. Carton, A. Makky, A.G. Olabi, Developments in fuel cell technologies in the transport sector, *Int. J. Hydrog. Energy*,2016, **164**, 16499–16508.

[22] N. Matulić, G. Radica, F. Barbir, S. Nižetić, Commercial Vehicle Auxiliary Loads Powered by PEM Fuel Cell*, Int. J. Hydrog. Energy*, 2019, **44**, 10082–10090.

[23] A. Baroutaji, T. Wilberforce, M. Ramadan, A. G. Olabi, Comprehensive Investigation on Hydrogen and Fuel Cell Technology in the Aviation and Aerospace Sectors, *Renew. Sustain. Energy Rev*., 2019, **106**, 34–40.

[24] N. Abdullah, S.K. Kamarudin, Titanium dioxide in Fuel Cell Technology: An Overview, *J. Power Sources*, 2015, **278**, 109–118.

[25] Q. Jia, Z. Zhao, L. Cao, J. Li, S. Ghoshal, V. Davies, E. Stavitski, K. Attenkofer, Z. Liu, M. Li, X. Duan, S. Mukerjee, T. Mueller and Y. Huang, Roles of Mo Surface Dopants in Enhancing the ORR Performance of Octahedral PtNi Nanoparticles, *Nano Lett*. 2018, **18**, 798−804.

[26] A. Hassana, V. A. Paganina, A. Carreras and E. A. Ticianelli, Molybdenum Carbide-based Electrocatalysts for CO Tolerance in Proton Exchange Membrane Fuel Cell Anodes, *Electrochim. Acta*, 2014, **142**, 307–316.

[27] A. Hassan, V. A. Paganin and E. A. Ticianelli, Effect of Addition of Ru and/or Fe in the Stability of PtMo/C Electrocatalysts in Proton Exchange Membrane Fuel Cells, *Electrocatalysis*, 2015, **6**, 512 – 520.

[28] M. Nagarajan, G. P. Kalaignan, G.A. Pathanjali, Novel Anodes for Fuel Cell using Nanostructured Tungsten and Titanium based Electrocatalysts, *Int. J. Hydrog. Energy*, 2011, **36**, 14829 – 14837.

[29] Y. Daia, Y. Liu and S. Chena, Pt–W Bimetallic Alloys as CO-tolerant PEMFC Anode Catalysts, *Electrochim. Acta* , 2013, **89**, 744– 748.

[30] R. Huang, G. F. Shao, Y. Zhang and Y. H. Wen, Thermal Stability of Platinum−Cobalt Bimetallic Nanoparticles: Chemically Disordered Alloys, Ordered Intermetallics, and Core−Shell Structures, *ACS Appl. Mater. Interfaces*, 2017, **9**, 12486–12493.

[31] V. V. Pryadchenko, S. V. Belenov, D. B. Shemet, V. V. Srabionyan, L. A. Avakyan, V. A. Volochaev, A. S. Mikheykin, K. E. Bdoyan, I. Zizak, V. E. Guterman and L. A. Bugaev, Effect of Thermal Treatment on the Atomic Structure and Electrochemical Characteristics of Bimetallic PtCu Core−Shell Nanoparticles in PtCu/C Electrocatalysts, *J. Phys. Chem. C*, 2018, **122**, 17199–17210.

[32] T. S. Almeida, A. R. Van Wassen, R. B. VanDover, A. R. De Andrade and H. D. Abruña, Combinatorial PtSnM (M = Fe, Ni, Ru and Pd) Nanoparticle Catalyst Library toward Ethanol Electrooxidation, *J. Power Sources*, 2015, **284**, 623–630.

[33] E. Lee, S. Kim, J. Jang, H. Park, A. Matin, Y. Kim and Y. Kwon, Effects of Particle Proximity and Composition of Pt-M (M = Mn, Fe,Co) Nanoparticles on Electrocatalysts in Methanol Oxidation Reaction, *J. Power Sources*, 2015, **294**, 75–81.

[34] Y. Munaiah, S. Boopathi, S. S. Kumar and P. Ragupathy, Unveiling the Enhanced Performance of Non-platinum based Hybrid Nanocomposites for Selective Electrocatalytic Oxygen Reduction, *Mater. Lett*., 2019, **239**, 184–191.

[35] Y. Ito, T. Takeuchi, T. Tsujiguchi, M. A. Abdelkareem and N. Nakagawa, Ultrahigh Methanol Electro-oxidation Activity of PtRu Nanoparticles prepared on TiO_2-embedded Carbon Nanofiber Support, *J. Power Sources*, 2013, **242**, 280–288.

[36] L. Dong, R. R. S. Gari, Z. Li, M. M. Craig and S. Hou, Graphene-supported Platinum and Platinum – ruthenium Nanoparticles with High Electrocatalytic Activity for Methanol and Ethanol Oxidation, *Carbon N. Y.*, 2009, **48**, 781–787.

[37] S. Meenakshi, P. Sridhar and S. Pitchumani, Carbon Supported Pt–Sn/SnO_2 Anode Catalyst for Direct Ethanol Fuel Cells, *RSC Adv*., 2014, **4**, 44386–44393.

[38] F. Xu, D. Wang, B. Sa, Y. Yu and S. Mu, One-pot Synthesis of Pt/CeO_2/C Catalyst for Improving the ORR Activity and Durability of PEMFC, *Int. J. Hydrogen Energy*, 2017, **42**, 13011–13019.

[39] C. Odetola, E. B. Easton and L. Trevani, Investigation of TiO_2/Carbon Electrocatalyst Supports prepared using Glucose as a Modifier, *Int. J. Hydrogen Energy*, 2015, **41**, 8199–8208.

[40] L. Du, Y. Shao, J. Sun, G. Yin, J. Liu and Y. Wang, Advanced Catalyst Supports for PEM Fuel Cell Cathodes, *Nano Energy*, 2016, **29**, 314–322.

[41] D. S. Van Vuuren, *Keynote address: Titanium-an opportunity and challenge for South Africa*, 2019, CSIR.

[42] M. Harris, The Production of Electrolytic Manganese in South Africa, *J. South. Afr. Inst. Min. Metall*., 1977, **7**, 137–142.

[43] M. Mehta, N. Kodan, S. Kumar, A. Kaushal, L. Mayrhofer, M. Walter, M. Moseler, A. Dey, S. Krishnamurthy, S. Basu and A. P. Singh, Hydrogen Treated Anatase TiO_2: A New Experimental Approach and Further Insights from Theory, *J. Mater. Chem. A*, 2016, **4**, 2670–2681.

[44] M. Z. Ghavidel, M. R. Rahman and E. B. Easton, Fuel Cell-based Breath Alcohol Sensors utilizing Pt-alloy Electrocatalysts, *Sensors Actuators B Chem*., 2018, **273**, 574–584.

[45] K. C. Kim, S. M. Cho and H. G. Choi, Detection of Ethanol Gas Concentration by Fuel Cell Sensors fabricated using a Solid Polymer Electrolyte, *Sensors Actuators B Chem*., 2000, **67**, 194–198.

[46] K. I. Ozoemena, S. Musa, R. Modise, A. K. Ipadeola, L. Gaolatlhe, S. Peteni and G. Kabongo, Fuel Cell-based Breath-alcohol Sensors : Innovation-hungry Old Electrochemistry, *Curr. Opin. Electrochem*., 2018, **10**, 82–87.

[47] C. Lamy, E.M. Belgsir and J-M. Leger, Electrocatalytic Oxidation of Aliphatic Alcohols: Application to the Direct Alcohol Fuel Cell (DAFC), *J. Appl. Electrochem*., 2001, **31**, 733 – 809.

[48] O. O. Fashedemi, H. A. Miller, A. Marchionni, F. Vizza and K. I. Ozoemena, Electro-oxidation of Ethylene Glycol and Glycerol at Palladium-decorated FeCo@Fe core–shell Nanocatalysts for Alkaline Direct Alcohol Fuel Cells: Functionalized MWCNT Supports and Impact on Product Selectivity, *J. Mater. Chem. A*, 2015, 3, 7145–7156.

[49] J. Zhou, J. Hu, X. Zhang, J. Li, K. Jiang, Y. Liu, G. Zhao, X. Wang, H. Chu, Facet Effect of Pt Nanocrystals on Catalytical Properties toward Glycerol Oxidation Reaction, *J. Catal*., 2020, **381**, 434–442.

[50] J. J. Duan, X. X. Zheng, H. J. Niu, J. J. Feng, Q. L. Zhang, H. Huang, A. J. Wang, Porous Dendritic PtRuPd Nanospheres with Enhanced Catalytic Activity and Durability for Ethylene Glycol Oxidation Oxygen Reduction Reactions, *J. Colloid Interface Sci*., 2020, **560**, 467–474.

[51] B. Cermenek, J. Ranninger, B. Feketeföldi, I. Letofsky-papst, N. Kienzel, B. Bitschnau and V. Hacker, Novel Highly Active Carbon Supported Ternary PdNiBi Nanoparticles as Anode Catalyst for the Alkaline Direct Ethanol Fuel Cell, *Nano Res*., 2020, **12**, 683–693.

[52] P. Nekooi, M. Akbari and M. K. Amini, CoSe Nanoparticles prepared by the Microwave-Assisted Polyol Method as an Alcohol and Formic Acid Tolerant Oxygen Reduction Catalyst, *Int. J. Hydrogen Energy*, 2010, **35**, 6392–6398.

[53] E. Antolini and E. R. Gonzalez, Ceramic Materials as Supports for Low-temperature Fuel Cell Catalysts, *Solid State Ionics*, 2009, **180**, 746 – 763.

[54] V. T. T. Ho, C. Pan, J. Rick, W. Su and B. Hwang, Nanostructured $Ti_{0.7}Mo_{0.3}O_2$ Support Enhances Electron Transfer to Pt: High-Performance Catalyst for Oxygen Reduction Reaction, *J. Am. Chem. Soc*., 2011, **133**, 11716–11724.

[55] Y. Dai, Y. Liu, and S. Chen, Pt-W Bimetallic Alloys as CO-tolerant PEMFC Anode Catalysts, *Electrochim Acta*, 2013, **89**, 744–748.

[56] R. M. A. Hameed, R. S. Amin, K. M. El-khatib and A. E. Fetohi, Preparation and Characterization of Pt-CeO_2/C and Pt-TiO_2/C Electrocatalysts with Improved Electrocatalytic Activity for Methanol Oxidation, *Appl. Surf. Sci*., 2016, **367**, 382–390.

[57] J. M. Jacob, P. G. Corradini, E. Antolini, N. A. Santos, J. Perez, Environmental Electro-oxidation of Ethanol on ternary Pt-Sn-Ce/C Catalysts, *Appl. Catal. B-Environ*., 2015, **165**, 176–184.

[58] S. Beyhan, J. Léger and F. Kadirgan, Pronounced Synergetic Effect of the Nano-sized PtSnNi/C Catalyst for Ethanol Oxidation in Direct Ethanol Fuel Cell, *Appl. Catal. B-Environ*., 2013, **131**, 305–313.

[59] M. Z. Ghavidel and E. B. Easton, Improving the Ethanol Oxidation Activity of Pt-Mn Alloys through the Use of Additives during Deposition, *Catalysts*, 2015, **5**, 1016–1033.

[60] N. Du, C. Wang, R. Long and Y. Xiong, N-doped Carbon-stabilized PtCo Nanoparticles derived from Pt@ZIF-67: Highly Active and Durable Catalysts for Oxygen Reduction Reaction, *Nano Res*., 2017, **10**, 3228–3237.

[61] A. Hassan, V. A. Paganin and E. A. Ticianelli, Investigation of Carbon supported PtW Catalysts as CO Tolerant Anodes at High Temperature in Proton Exchange Membrane Fuel Cell, *J. Power Sources*, 2016, **325**, 375–382.

[62] Y. Nie, L. Li and Z. Wei, Recent Advancements in Pt and Pt-free Catalysts for Oxygen Reduction Reaction, *Chem. Soc. Rev*., 2015, **44**, 2168–2201.

[63] S. Mukerjee, S. J. Lee, E. A. Ticianelli, J. McBreen, B. N. Grgur, N. M. Markovic, P. N. Ross, J. R. Giallombardo, E. S. De Castro, Investigation of Enhanced CO Tolerance in Proton Exchange Membrane Fuel Cells by Carbon Supported PtMo Alloy Catalyst, *Electrocem. Solid State Lett*., 1999, **2**, 12–15.

[64] S. Jongsomjit, P. Prapainainar and K. Sombatmankhong, Synthesis and Characterisation of Pd-Ni-Sn Electrocatalyst for use in Direct Ethanol Fuel Cells, *Solid State Ionics*, 2016, **288**, 147–153.

[65] D. K. Hassen, M. M. Selim, S. A. El- safty, K. A. Khalil, G. A. el-Maged and M. Dewidar, Graphene-Supported $Co(OH)_2$ Mesostructures for Ethanol Oxidation Reaction Electrocatalysis, *Nano-Structures & Nano-Objects*, 2017, **9**, 31–39.

[66] H. A. Miller, A. Lavacchi, F. Vizza, M. Marelli, F. D. Benedette, F. D. Acapito, Y. Paska, M. Page and D. R. Dekel, A Pd/C-CeO_2 Anode Catalyst for High-Performance Platinum-Free Anion Exchange Membrane Fuel Cells, *Angewante*, 2016, **3200003**, 6108–6111.

[67] X. Xie, S. Chen, W. Ding, Y. Nie and Z. Wei, An Extraordinarily Stable Catalyst: Pt NPs Supported on Two-Dimensional $Ti_3C_2X_2$ (X=OH, F) Nanosheets for Oxygen Reduction Reaction, *Chem. Commun*., 2013, **49**, 1–11.

[68] J. Guo, Y. Li, Y. Cheng, L. Dai, Z. Xiang, Highly Efficient Oxygen Reduction Reaction Electrocatalysts Synthesized Under Nanospace Confinement of Metal-Organic Framework, *ACS Nano*, 2017, **11**, 8379–8386.

[69] Y. Huang, C. Feng, H. Wu, S. Wang, F. Wang and H. Liu, Hybrids of Fe_3O_4/$CoSe_2$ as Efficient Electrocatalysts for Oxygen Reduction Reaction, *J. Mater. Sci*., 2018, **53**, 1123–1134.

[70] X. Wang, H. Zhang, H. Lin, S. Gupta, C. Wang, Z. Tao, H. Fu, T. Wang, J. Zheng, G. Wu and X. Li, Directly Converting Fe-Doped Metal-Organic Frameworks into Highly Active and Stable Fe-N-C Catalysts for Oxygen Reduction in Acid, *Nano Energy*, 2016, **25**, 110–119.

[71] G. Dong, M. Huang and L. Guan, Iron Phthalocyanine Coated on Single-Walled Carbon Nanotubes Composite for the Oxygen Reduction Reaction in Alkaline Media, *Phys. Chem. Chem. Phys*., 2012, **14**, 2557–2559.

[72] E. Antolini, Pt-Ni and Pt-M-Ni (M = Ru, Sn) Anode Catalysts for Low-Temperature Acidic Direct Alcohol Fuel Cells: A Review, *Energies*, 2017, **10**, 1–20.

[73] A. A. Gewirth, J. A. Varnell and A. M. Diascro, Nonprecious Metal Catalysts for Oxygen Reduction in Heterogeneous Aqueous Systems, *Chem. Rev*., 2018, **118**, 2313–2339.

[74] Z. Zhang, L. Xin, K. Sun and W. Li, Pd-Ni Electrocatalysts for Efficient Ethanol Oxidation Reaction in Alkaline Electrolyte, *Int. J. Hydrog. Energy*, 2011, **36**, 12686–12697.

[75] J. He, X. He, L. Liu, B. Hu, F. Bai and P. Zhang, Tailoring Carbon Materials Substrate to Modify the Electronic Structure of Platinum for Boosting Its Electrocatalytic Activity, *J. Electrochem. Soc*., 2018, **165**, 247–252.

[76] E. Pomerantseva, F. Bonaccorso, X. Feng, Y. Cui and Y. Gogotsi, Energy storage: The Future Enabled by Nanomaterials, *Science*, 2019, **366**, 1–12.

[77] T. Ioroi, H. Senoh, S. Yamazaki, Z. Siroma, N. Fujiwara and K. Yasuda, Stability of Corrosion-Resistant Magnéli-Phase Ti_4O_7-Supported PEMFC Catalysts at High Potentials, *J. Electrochem. Soc*., 2008, **155**, B231–B326.

[78] Y. Bai, J. Wu, J. Xi, J. Wang, W. Zhu, L. Chen and X. Qiu, Electrochemical Oxidation of Ethanol on Pt-ZrO_2/C Catalyst, *Electrochem. Comm*., 2005, **7**, 1087–1090.

[79] M. Roca-Ayats, G. García, M. Soler-Vicedo, E. Pastor, M. J. lázaro, M. V. Martínez-Huerta, The Role of Sn, Ru and Ir on the Ethanol Electrooxidation on Pt_3M/TiCN Electrocatalysts, *Int. J. Hydrog. Energy*, 2015, **40**, 14519–14528.

[80] R. A. M. Esfahani, I. I. Ebralidze, S. Specchia and E. B. Easton, A Fuel Cell Catalyst Support based on Doped Titanium Suboxides with Enhanced Conductivity, Durability and Fuel Cell Performance, *J. Mater. Chem. A*, 2018, **6**, 14805–14815.

[81] R. Alipour, M. Esfahani, L. Miguel, R. Gavidia, G. García, E. Pastor and S. Specchia, A Fuel Cell Catalyst Support based on Doped Titanium Suboxides with Enhanced Conductivity, Durability and Fuel Cell Performance, *Renew. Energy*, 2018, **120**, 209–219.

[82] S. Shahgaldi and J. Hamelin, The Effect of Low Platinum Loading on the Efficiency of PEMFC's Electrocatalysts Supported on TiO_2-Nb and SnO_2-Nb: An Experimental Comparison between Active and Stable Conditions, *Energy Convers. Manag.*, 2015, **103**, 681–690.

[83] A. E. Alvarez, A. N. Gravina, J. M. Sieben, P. V. Messina and M. M. E. Duarte, Synthesis of PtSn Nanostructured Catalysts Supported Over TiO_2 and Ce-doped TiO_2 Particles for the Electro-oxidation of Ethanol, *Mater. Sci. Eng.*, 2016, **211**, 26–32.

[84] S. Samad, K. Shyuan, K. S. Loh, W. Y. Wong, T. K. Lee, J. Sunarso, S. T. Chong and W. R. W. Daud, Carbon and Non-Carbon Support Materials for Platinum-Based Catalysts in Fuel Cells, *Int. J. Hydrog. Energy*, 2017, **43**, 7823–7854.

[85] P. Wang, Y. Wen, S. Yin and N. Wang, PtRh Alloys on Hybrid TiO_2-Carbon Support as High Efficiency Catalyst for Ethanol Oxidation, *Int. J. Hydrog. Energy*, 2017, **42**, 2489–24696.

[86] L. Wang, X. Zhang, W. Liu, W. Xu, A. Singh and Y. Lin, Electrochemical Properties of Ti_3O_5 Powders Prepared by Carbothermal Reduction, *J. Mater. Sci: Mater. Electron*, 2017, **28**, 6421–6425.

[87] I. A. Rutkowska and P. J. Kulesza, Electroanalysis of Ethanol Oxidation and Reactivity of Platinum-Ruthenium Catalysts Supported onto Nanostructured Titanium Dioxide Matrices, *J. Electrochem. Soc.*, 2016, **163**, 3052–3060.

[88] X. Sui, Z. Wang, M. Yang, L. Huo, D. Gu and G. Yin, Investigation on $CeTiO_2$ Nanotubes Composite as Pt Catalyst Support for Methanol Electrooxidation, *J. Power Sources*, 2014, **255**, 43–51.

[89] R. Alipour, M Esfahani, S. K. Vankova, A. H. A. M Videla and S. Specchia, Innovative Carbon-Free Low Content Pt Catalyst Supported on Mo-Doped Titanium Suboxide (Ti_3O_5-

Mo) for Stable and Durable Oxygen Reduction Reaction, *Appl. Catal, B-Environ*., 2017, **201**, 419–429.

[90] K. Park and K Seol, Nb-TiO_2 Supported Pt Cathode Catalyst for Polymer Electrolyte Membrane Fuel Cells, *Electrochem. Commun*., 2007, **9**, 2256–2260.

[91] L. Yu, and J. Xi, CeO_2 Nanoparticles Improved Pt-Based Catalysts for Direct Alcohol Fuel Cells, *Int. J. Hydrog. Energy*, 2012, **37**, 15938–15947.

[92] K. Kakaei, A. Rahimi, S. Husseindoost, M. Hamidi, H. Javan and A. Balavandi, Fabrication of Pt-CeO_2 Nanoparticles Supported Sulfonated Reduced Graphene Oxide as an Efficient Electrocatalyst for Ethanol Oxidation, *Int. J. Hydrog. Energy*, 2016, **30**, 1–9.

[93] A. Ganesan, M. Narayanasamy and K. Shunmugavel, Self-Humidifying Manganese Oxide-Supported Pt Electrocatalysts for Highly-Durable PEM Fuel Cells, *Electrochim. Acta*, 2018, **285**, 47–59.

[94] G. R. Mirshekari and A. P. Shirvanian, Electrochemical Behaviour of Manganese Oxide Nanoparticles for Oxygen Reduction Reaction Environment in PEM Fuel Cells, *ECS Transactions*, 2017, **80**, 707–716.

[95] L. Lu, H. Xu, J. Shi, S. Zhu, H. Zhao and G. Wang, Pt-Supported C-MnO_2 as a Catalyst for Polymer Electrolyte Membrane Fuel Cells, *J. Appl. Electrochem*., 2018, **48**, 801–810.

[96] D. R. Askeland, W. J. Wright, *Science and Engineering of Materials*, Nelson Education, 2015.

[97] R. Jenkins, R. L. Snyder, *Introduction to X-ray Powder Diffractometry*, Wiley, 1996.

[98] Z. Guo, X. Kang, X. Zheng, J. Huang and A. Chen, PdCu Alloy Nanoparticles Supported on CeO_2 Nanorods: Enhanced Electrocatalytic Activity by Synergy of Compressive Strain, PdO and Oxygen Vacancy, *J. Catal*., 2019, **374**, 101–109.

[99] A. Pérez-Larios, A. Hernández-Gordillo, G. Moraes-Mendoza, L. Lartundo-Roja, Á. Mantilla, R. Gómeza, Enhancing the H_2 Evolution from Water-Methanol Solution using Photocatalysts, *Catalysis Today*, 2016, **266**, 9–16.

[100] Y. Leng, *Materials Characterization: Introduction to Microscopic and Spectroscopic Methods*, John Wiley & Sons, 2009.

[101] A. Petr, L. Dunsch and A. Neudeck, In Situ EPR/UV–VIS Spectroelectrochemistry of Polypyrrole Redox Cycling, *J. Chem. Soc.*,1998, **412,** 3625–3630.

[102] J. I., Goldstein, D. E. Newbury, P. Echlin, D. C. Joy, C. E. Lyman, E, Lifshin and J. R. Michael, *Special topics in electron beam x-ray microanalysis. In Scanning Electron Microscopy and X-ray Microanalysis*, Springer, Boston MA, 2003.

[103] H. Kohl and L. Reimer, *Transmission Electron Microscopy: Physics of Image Formation*. Springer, New York, 2008.

[104] A. J. Bard, L. R. Faulkner, E. Swain and C. Robey, *Fundamentals and Applications*, 2nd ed., 2000.

[105] K. Kakaei, Decoration of Graphene Oxide with Platinum Tin Nanoparticles for Ethanol Oxidation, *Electrochim. Acta*, 2015, **165**, 330–337.

[106] P. Bocchetta, C. R. Sánchez, A. Taurino and B. Bozzini, Accurate Assessment of the Oxygen Reduction Electrocatalytic Activity of Mn/Polypyrrole Nanocomposites Based on Rotating Disk Electrode Measurements, Complemented with Multitechnique Structural Characterizations, *J. Anal. Methods*, 2016, **2016**, 12–14.

[107] O. O. Fashedemi and K. I. Ozoemena, Oxygen Reduction Reaction at MWCNT-Modified Nanoscale Iron (II) tetrasulfophthalocyanine: Remarkable Performance over

Platinum and Tolerance toward Methanol in Alkaline Medium, *RSC Adv*., 2015, **5**, 22869–22878.

[108] B. Ruiz-Camacho, J. H. Martínez-González, R. G. González-Huerta, M. Tufino-Velázquez, Kinetic Study of Oxygen Reduction Reaction and PEM Fuel Cell Performance of Pt/TiO_2-C Electrocatalyst, *Int. J. Hydrog. Energy*, 2014, **39**, 16731–16739.

[109] X. Gao, J. Wang, Z. Ma and J. Ye, Iron tetrasulfophthalocyanine Functionalized Graphene Nanosheets for Oxygen Reduction Reaction in Alkaline Media, *Electrochim. Acta*, 2014, **130**, 543–550.

[110] A. M. T. Silva, C. G. Silva, G. Dražic and J. L. Faria, Ce-doped TiO_2 for Photocatalytic Degradation of Chlorophenol, *Catalysis Today*, 2009, **144**, 13–18.

[111] M. S. P. Francisco and V. R. Mastelaro, Inhibition of the Anatase-Rutile Phase Transformation with Addition of CeO_2 to CuO-TiO_2 System: Raman Spectroscopy, X-ray Diffraction, and Textural Studies, *Chem. Mater*., 2002, **14**, 2514–2518.

[112] Z. Guowei, K. Youngsoo, L. I. Tianduo and X. U. Guiying, Sol-gel Preparation and Spectroscopic Study of the Pyrophanite $MnTiO_3$ Nanoparticles, *Science in China Ser. B Chemistry*, 2005, **48**, 210–215.

[113] M. Vranješ, J. K. Jakovljević, M. Milošević, G. Ć, M. Stoiljković, A. Konstantinović, V. Pavlović, D. Milivojević and Z. Šaponjić, Hydrothermal Synthesis of Mn^{2+} Doped Titanate Nanotubes : Investigation of their Structure and Room Temperature Ferromagnetic Behaviour, *Solid state Sciences*, 2019, **94**, 155–161.

[114] R. K. Maurya and D. Singh, Nano-Mechanical Behaviour of $MnTiO_3$ Ceramics, *Mater. Lett*., 2019, **246,** 49–51.

[115] Z. Liu, B. Guo, L. Hong and H. Jiang, Preparation and Characterization of Cerium Oxide Doped TiO_2 Nanoparticles, *J. Phys. Chem. Solids*, 2005, **66**, 161–167.

[116] Q. R. Deng, X. H. Xia, M. L. Guo, Y. Gao and G. Shao, Mn-Doped TiO_2 Nanopowders with Remarkable Visible Light Photocatalytic Activity, *Mater. Lett*., 2011, **65**, 2051–2054.

[117] S. Prabhu, T. Viswanathan, K. Jothivenkatachalam and K. Jeganathan, Visible Light Photocatalytic Activity of CeO_2-ZnO-TiO_2 Composites for the Degradation of Rhodamine B, *Indian J. Mater. Sci*., 214, **2014**, 1–10.

[118] J. Li, D. H. L. Ng, F. Luen, K. Ka and L. Chiu, Hierarchically Porous Fibers Heterojunction Photocatalysts with Synergistic Adsorption-Photocatalytic Performance under Visible Light, *J. Porous Mater*., 2017, **24**, 1047–1059.

[119] M. Ahamed, M. A. M. Khan, M. J. Akhtar and H. A. Alhadlaq, Ag-Doping Regulates the Cytotoxicity of TiO_2 Nanoparticles via Oxidative Stress in Human Cancer Cells, *Sci. Rep*., 2017, **7**, 1 – 14.

[120] A. Lu, H. Sun, N. Zhang, L. Che, S. Shan, J. Luo, J. Zheng, L. Yang, D. Peng, C. Zhong and B. Chen, Surface Partial-Charge-Tuned Enhancement of Catalytic Activity of Platinum Nanocatalysts for Toluene Oxidation, *ACS Catal*., 2019, **9**, 7431 – 7442.

[121] B. Qui, C. Wang, N. Zhang, L. Cai, Y. Xiong and Y. Chai, CeO_2-Induced Interfacial Co^{2+} Octahedral Sites and Oxygen Vacancies for Water Oxidation, *ACS Catal*., 2019, **9**, 6484–6490.

[122] G. Perenlei, T. W. Tee, N. A. Yusof and G. J. Kheng, Voltammetric Detection of Potassium Ferricyanide Mediated by Multi-walled Carbon Nanotube/Titanium Dioxide Composite Modified Glassy Carbon Electrode, *Int. J. Electrochem. Sci*., 2011, **6**, 520–531.

[123] A. S. Adekunle, J. Pillay and K. I. Ozoemena, Electrocatalysis of 2-Diethylaminoethanethiol at Nickel Nanoparticle-Electrodecorated Single-Walled Carbon Nanotube Platform: An Adsorption-Controlled Electrode Process, *Electroanal*., 2008, **23**, 2587–2591.

[124] L. Gaolatlhe, R. Barik, S. C. Ray and K. I. Ozoemena, Voltammetric Responses of Porous Co_3O_4 Spinels Supported on MOF-Derived Carbons: Effects of Porous Volume on Dopamine Diffusion Processes, *J. Electroanl. Chem*., 2020, 113863.

[125] J. Wang, J. Polleux, J. Lim and B. Dunn, Pseudocapacitive Contributions to Electrochemical Energy Storage in TiO_2 (Anatase) Nanoparticles, *J. Phys. Chem. C*, 2007, **2**, 14925–14931.

[126] N. W. Maxakato, K. I. Ozoemena and J. Arendse, Dynamics of Electrocatalytic Oxidation of Ethylene Glycol, Methanol and Formic Acid at MWCNT Platform Electrochemically Modified with Pt/Ru Nanoparticles, *Electroanalysis*.,2010, **22**, 519–529.

[127] C. Batchelor-McAuley, L. M. Gonçalves, L. Xiong, A. A. Barros and R. G. Compton, Controlling Voltammetric Responses by Electrode Modification; using Adsorbed Acetone to Switch Graphite Surfaces between Adsorptive and Diffusive Modes, *Chem. Commun*., 2010, **48**, 9037–9039.

[128] B. Kaur, B. Satpati and R. Srivastava, Synthesis of $NiCo_2O_4$/Nano-ZSM-5 Nanocomposite Material with Enhanced Electrochemical Properties for the Simultaneous Determination of Ascorbic Acid, Dopamine, Uric Acid and Tryptophan, *New J. Chem*., 2015, **39**, 1115–1124.

[129] D. K. Subbiah, N. Nesakumar, A. J. Kulandaisamy and J. B. B. Rayappan, Ferricyanide/Reduced Graphene Oxide as Electron Mediator for the Electrochemical Detection

of Methanol in Canned Citrus Sinensis and Citrus Limetta, *Sensors Actuators B Chem.*, 2017, **248**, 708–717.

[130] A. S. Adekunle and K. I. Ozoemena, Electron Transport and Electrocatalytic Properties of MWCNT/Nickel Nanocomposites: Hydrazine and Diethylaminoethanethiol as Analytical Probes, *J. Electroanal. Chem.*, 2010, **645**, 41–49.

[131] N. W. Maxakato, C. J. Arendse and K. I. Ozoemena, Insights into the Eelectro-Oxidation of Ethylene Glycol at Pt/Ru Nanocatalysts Supported on MWCNTs: Adsorption-Controlled Electrode Kinetics, *Electrochem. Commun.*, 2009, **11**, 534–537.

[132] G. L. Cordeiro, E. F. De Camargo, M. C. L. Santos, C. V. Pereira, V. Ussui, N. B. de Lima, A. O. Neto, D. R. R. Lazar, Improved Pt/CeO_2 Electrocatalysts for Ethanol Electro-Oxidation, *Int. J. Electrochem. Sci.*, 2018, **13**, 6388–6401.

[133] L. Artiglia, S. Agnoli and S. Chimiche, Cerium Oxide Nanostructures on Titania: Effect of the Structure and Stoichiometry on the Reactivity Toward Ethanol Oxidation, *J. Phys. Chem. C*, 2018, **122**, 20809–20816.

[134] M. Sedighi, A. Ali and E. Alizadeh, Enhanced Electro-Oxidation of Ethanol using Pt-CeO_2 Electrocatalyst Prepared by Electrodeposition Technique, *Int. J. Hydrog. Energy*, 2016, **42**, 4998 – 5005.

[135] L. Jiang, A. Hsu, D. Chu and R. Chen, Ethanol Electro-Oxidation on Pt/C and PtSn/C Catalysts in Alkaline and Acid Solutions, *Int. J. Hydrog. Energy*, 2010, **35**, 365–372.

[136] S. Guo, J. Liu, S. Qiu, W. Liu, Y. Wang, N. Wu, J. Guo and Z. Guo, Porous Ternary $TiO_2/MnTiO_3$@C Hybrid Microspheres as Anode Materials with Enhanced Electrochemical Performances, *J. Mater. Chem. A*, 2015, **3**, 23895 – 23904

[137] Q. Guo, C. Li, X. Zhang, D. Huang and C. Lei, Facile Synthesis of Porous Ternary $MnTiO_3/TiO_2/C$ Composite with Enhanced Electrochemical Performance as Anode Materials for Lithium Ion Batteries, *Energy Technol*., 2019, **7**, 1800761.

[138] K. Tiido, N. Alexeyeva, M. Couillard, C. Bock, B. R. Macdougall and K. Tammeveski, Graphene-TiO_2 Composite Supported Pt Electrocatalyst for Oxygen Reduction Reaction, *Electrochim. Acta*, 2013, **107**, 509–517.

[139] K. H. Lee, K. Kwon, V. Roev, D. Y. Yoo, H. Chang and D. Seung, Synthesis and Characterization of Nanostructured PtCo-CeO_x/C for Oxygen Reduction Reaction, *J. Power Sources*., 2008, **185**, 871 – 875.

[140] C. Song and J. Zhang, *Electrocatalytic Oxygen Reduction Reaction in PEM Fuel Cell Electrocatalysts and Catalysts layers*, Springer, London, 2008.

[141] K. Fugane, T. Mori, D. Rong, A. Suzuki and H. Yoshikawa, Activity of Oxygen Reduction Reaction on Small Amount of Amorphous CeO_x Promoted Pt Cathode for Fuel Cell Application, *Electrochim. Acta*, 2011, **56**, 3874–3883.

[142] Q. He, S. Mukerjee, R. Zeis, S. Parres-Esclapez, M. J. Illán-Gómez and A. Bueno-López, Enhanced Pt Stability in MO_2 (M = Ce, Zr or $Ce_{0.9}Zr_{0.1}$)-Promoted Pt/C Electrocatalysts for Oxygen Reduction Reaction in PAFCs, *Appl. Catal. A*, 2010, **381**, 54–65.

[143] V. S. Murthi, R. C. Urian and S. Mukerjee, Oxygen Reduction Kinetics in Low and Medium Temperature Acid Environment: Correlation of Water Activation and Surface Properties in Supported Pt and Pt Alloy Electrocatalysts, *J. Phys. Chem. B*, 2004, **108**, 11011-11023.

[144] J. T. S. Allan, H. L. Geoffrey, and E. B. Easton, The Effect of Gas Diffusion Layer on the Performance of Fuel Cell Catalyst Layers in Ethanol Sensors, *Sensors Actuators B Chem*., 2018, **254**, 120–132.

[145] J. Allan, The Modification of Fuel Cell-Based Breath Alcohol Sensor Materials to Improve Water Retention of Sensing Performance, Ontario Institute of Technology, 2016.

[146] M. R. Rahman, J. T. S. Allan, M. Z. Ghavidel, L. E. Prest, F. S. Saleh and E. B. Easton, The Application of Power-Generating Fuel Cell Electrode Materials and Monitoring Methods to Breath Alcohol Sensors, *Sensors Actuators B Chem*., 2016, **228**, 448–457.

[147] L. E. Prest, Fundamental Investigation of Fuel Cell-based Breath Alcohol Sensors and the Cause of Sensor Degradation in Low-humidity Conditions, Ontario Institute of Technology, 2011.

[148] A. W. Jones, Measuring Alcohol in Blood and Breath for Forensic Purposes - A Historical Review, *Forensic Science Review*, 1996, **1**, 15–44.

[149]A. Modjtahedi, A. Amirfazli and S. Farhad, Low Catalyst Loaded Ethanol Gas Fuel Cell Sensor, *Sensors Actuators B Chem*., 2016, **234**, 70–79.